

UNIVERSITÄT BREMEN

DISSERTATION

---

Loading of coloured dissolved organic  
matter in the Arctic Mediterranean  
Sea and its effects on the ocean heat  
budget

---

*Author:*

Vasileios PEFANIS

*Supervisor:*

Prof. Dr. Torsten KANZOW

*in fulfillment of the requirements*

*for the degree of Doctor of Natural Sciences (Dr. rer. nat.) in the*

Faculty of Physics and Electrical Engineering

Doctoral Colloquium: May 19, 2021

1. Reviewer: Prof. Dr. Torsten Kanzow

Alfred Wegener Institute, Helmholtz Centre for Polar and Marine Research, Bremerhaven  
University of Bremen

2. Reviewer: Dr. Maren Walter

University of Bremen

This dissertation was written at the Physical Oceanography of Polar Seas section of the Alfred Wegener Institute, Helmholtz Centre for Polar and Marine Research, Bremerhaven.

*Keep Ithaka always in your mind.  
Arriving there is what you're destined for.  
But don't hurry the journey at all.  
Better if it lasts for years,  
so you're old by the time you reach the island,  
wealthy with all you've gained on the way,  
not expecting Ithaka to make you rich.*

*Ithaka gave you the marvelous journey.  
Without her you wouldn't have set out.  
She has nothing left to give you now.*

*And if you find her poor, Ithaka won't have fooled you.  
Wise as you will have become, so full of experience,  
you'll have understood by then what these Ithakas mean.*

Ithaka by C. P. Cavafy





# Abstract

Currently, the most rapid increase in near-surface air temperature takes place in the Arctic, accompanied by a decline in sea ice cover. Consequently, the underwater shortwave radiation, and thus, the type and amount of phytoplankton are changing. In this context, the thawing permafrost, accompanied by increased precipitation and freshwater discharge, is expected to result in higher loads of coloured dissolved organic matter (CDOM) and total suspended matter (TSM) entering the Arctic Ocean. The amount of these optically active water constituents determines how much light is absorbed in the surface waters and how much can reach greater depths, affecting the vertical distribution of heat.

In this thesis, I first examine the potential of CDOM and TSM in enhancing the radiative heating and sea ice melting in the shelf waters of the Laptev Sea, an area heavily influenced by one of the largest river systems in the Arctic region. By using *in situ* observations, I simulate the in-water radiative heating utilizing coupled atmosphere-ocean radiative transfer modelling (RTM). The results indicate that CDOM and TSM highly affect the energy budget of the Laptev Sea shelf waters, absorbing most of the solar energy in the first 2 meters of the water column. The increased absorbed energy leads to higher sea ice melt rates and changes in the heat exchange with the atmosphere. By using satellite remote sensing and RTM, I quantify the spatial distribution of radiative heating in the Laptev Sea for a typical summer day. The spatial patterns of radiative heating closely follow the distribution of the optically active water constituents, with the highest energy absorption occurring over river-influenced waters.

As a next step, I upscale the previous one-dimensional and regional study by means of general circulation modelling for the entire Arctic Mediterranean Sea. By operating an ocean biogeochemical model coupled to a general circulation model with sea ice

(Darwin-MITgcm), the effect of phytoplankton and CDOM is incorporated into the in-water shortwave radiation penetration scheme. Accounting for their radiative effect increases the sea surface temperature (SST) in summer, decreases the sea ice concentration, and induces more heat loss to the atmosphere, primarily through sensible and latent heat flux. In some parts of the Eastern Arctic, the sea ice season is reduced by up to one month. CDOM drives 48% of the summertime changes in SST, suggesting that an increase in its concentration will amplify the observed Arctic surface warming. Additionally, the CDOM effect alters the vertical diffusion, advection, and non-local vertical mixing of heat. The shortwave heating and vertical diffusion terms account for a large part of the Arctic-wide changes in the heat budget throughout the year. On the contrary, in the Atlantic sector, differences in the sub-surface heating can be largely determined by advective and non-local mixing processes in spring and winter. In the Norwegian Sea, the sub-surface wintertime indirect dynamical effect is 2.7 times larger than the effect of shortwave heating. These results underline the potential of indirect changes in advective and mixing processes in intensifying or dumping the direct effect of CDOM at the sub-surface.

The changes induced by CDOM feed back on phytoplankton and CDOM itself, leading to higher annual mean surface concentrations for both of them. On the contrary, phytoplankton reduces at the sub-surface resulting in a 16.6% overall biomass decrease in the upper 100 m. The areas where light limits phytoplankton growth, expand at the expense of nutrient limitation. In spring, reduced light availability causes a phytoplankton bloom delay and an increase in nutrient concentrations. However, in summer the excess of nutrients together with the light limitation confine phytoplankton growth in a few tens of meters from the ocean surface leading to an intensification and delay of the end of the bloom, especially at the Barents Sea. These findings indicate that a future increase of CDOM will ignite a secondary positive feedback mechanism on the Arctic's surface warming, through increased phytoplankton and CDOM light absorption close to the surface.

Annotation: *The Arctic Mediterranean Sea comprises the Arctic Ocean and the Greenland, Iceland and Norwegian (the Nordic) Seas.*

### List of publications included in the thesis

Soppa, M. A., Pefanis, V., Hellmann, S., Losa, S. N., Hölemann, J., Martynov, F., Heim, B., Janout, M. A., Dinter, T., Rozanov, V. and Bracher, A. (2019). Assessing the influence of water constituents on the radiative heating of Laptev Sea shelf waters. *Frontiers in Marine Science*, 6 (221), 1-13. doi: <https://doi.org/10.3389/fmars.2019.00221>

Pefanis, V., Losa, S. N., Losch, M., Janout, M. A. and Bracher, A. (2020). Amplified Arctic surface warming and sea-ice loss due to phytoplankton and colored dissolved material. *Geophysical Research Letters*, 47, e2020GL088795. doi: <https://doi.org/10.1029/2020GL088795>

### Publications not included in the thesis

Nakoudi, K., Ritter, C., Böckmann, C., Kunkel, D., Eppers, O., Rosanov, V., Mei, L., Pefanis, V., Jäkel, E., Herber, A., Maturilli, M. and Neuber, R. (2020). Does the Intra-Arctic Modification of Long-range Transported Aerosol Affect the Local Radiative Budget?. *Remote Sensing*, 12(13), 2112. doi: <https://doi.org/10.3390/rs12132112>



# Contents

<b>Abstract</b>	<b>v</b>
<b>List of Publications</b>	<b>vii</b>
<b>1 Introduction</b>	<b>1</b>
1.1 Motivation . . . . .	1
1.2 Theoretical background . . . . .	6
1.2.1 Inherent optical properties . . . . .	6
1.2.2 Optically-active water constituents . . . . .	7
1.2.3 Apparent optical properties . . . . .	11
1.2.4 Radiative transfer theory . . . . .	12
1.3 Scope of the thesis . . . . .	16
1.4 Thesis outline . . . . .	17
<b>2 Materials and methods</b>	<b>19</b>
2.1 Radiative transfer model simulations . . . . .	19
2.1.1 <i>In situ</i> data . . . . .	19
2.1.2 Ocean colour remote sensing retrievals . . . . .	20
2.1.3 Model description (SCIATRAN) . . . . .	21
2.1.4 Radiative transfer model evaluation . . . . .	23
2.1.5 Radiative heating simulations . . . . .	23
2.1.6 Spatial distribution of heating . . . . .	26
2.2 Coupled ocean-biogeochemical model simulations . . . . .	27
2.2.1 The MIT general circulation model . . . . .	27
2.2.2 The JRA-55 atmospheric reanalysis . . . . .	29
2.2.3 Heat budget equation . . . . .	30
2.2.4 Surface heat flux components . . . . .	31
2.2.5 Vertical mixing parameterization (KPP) . . . . .	32
2.2.6 The Darwin biogeochemical model . . . . .	33

2.2.7	Phenological indices . . . . .	34
2.2.8	Phytoplankton growth limiting factors . . . . .	35
2.2.9	Model evaluation . . . . .	35
<b>3</b>	<b>Assessing the influence of water constituents on the radiative heating of Laptev Sea shelf waters</b>	<b>37</b>
3.1	Introduction . . . . .	37
3.2	Results . . . . .	38
3.2.1	Evaluation of the radiative transfer model . . . . .	38
3.2.2	Bio-optical effect of CDOM and TSM on the radiative heating . . . . .	40
3.2.3	Absorbed energy and radiative heating . . . . .	42
3.2.4	Sea ice melt and atmosphere-ocean heat flux . . . . .	44
3.2.5	Radiative heating distribution . . . . .	46
3.3	Conclusions . . . . .	48
<b>4</b>	<b>Amplified Arctic surface warming and sea ice loss due to phytoplankton and CDOM</b>	<b>51</b>
4.1	Introduction . . . . .	51
4.2	Model evaluation . . . . .	52
4.2.1	Sea ice . . . . .	52
4.2.2	Water constituents . . . . .	54
4.3	Accounting for the effect of biogeochemistry in light attenuation . . . . .	56
4.4	CDOM light absorption effect . . . . .	60
4.4.1	Surface heat flux components . . . . .	62
4.4.2	Heat budget analysis . . . . .	65
4.5	Discussion and implications . . . . .	71
4.6	Conclusions . . . . .	74
<b>5</b>	<b>Biogeochemical implications of light absorption by CDOM in the Arctic Ocean and the subarctic seas</b>	<b>77</b>
5.1	Introduction . . . . .	77
5.2	Model nutrients evaluation . . . . .	78
5.3	Implications of light absorption by CDOM . . . . .	80
5.3.1	Light, biomass, and nutrients . . . . .	80
5.3.2	Phytoplankton growth limiting factors . . . . .	85
5.3.3	Phytoplankton phenology . . . . .	90

5.4	Conclusions	91
<b>6</b>	<b>Conclusions and outlook</b>	<b>93</b>
6.1	Main outcomes	93
6.2	Outlook	97
	<b>Bibliography</b>	<b>99</b>
	<b>Acknowledgements</b>	<b>113</b>
<b>A</b>	<b>Appendix A</b>	<b>115</b>
A.1	Heat budget analysis	115
A.1.1	Robustness	115
A.2	Phytoplankton phenology	118
<b>B</b>	<b>Appendix B</b>	<b>121</b>
B.1	Model output	121
B.2	Model configuration	121
	<b>Declaration of Authorship</b>	<b>133</b>





# Chapter 1

## Introduction

### 1.1 Motivation

The rise of global temperatures over the course of the last century, referred to as global warming, is one of the greatest challenges for humanity. Although a global mean increase of  $0.85^{\circ}\text{C}$  has been estimated over the 1880-2012 period (IPCC, 2013), the temperature changes exhibit strong temporal and zonal variability (Fig. 1.1). During the last decades, surface air temperature in the Arctic has increased at least twice as much as the global average, a phenomenon known as Arctic Amplification (Serreze et al., 2009; Serreze and Barry, 2011; Wendisch et al., 2017). As shown in Figure 1.1, the last decade's annual and zonal mean surface temperature increase over the Arctic ( $> 66^{\circ}\text{N}$ ) exceeds  $2^{\circ}\text{C}$ , compared to the reference period (1946-1980).

Although the mechanisms that trigger Arctic Amplification are not yet fully understood (Serreze and Barry, 2011), the phenomenon has been linked to the retreat and thinning of sea ice. From 1979 to 2012, the minimum sea ice extent in September has been dropping by 13% per decade, leading to a total reduction of more than 30% (Stroeve et al., 2012). Subsequently, the 13 lowest Arctic sea ice extents in the satellite record history have been observed in the last 13 years (2007-2019) (Perovich et al., 2019). The most pronounced retreat took place in 2012, where summer sea ice extent reached a minimum record of  $3.4 \times 10^6 \text{ km}^2$  (Parkinson and Comiso, 2013). Climate model projections suggest that the Arctic Ocean may become ice free (sea ice area  $< 10^6 \text{ km}^2$ ) in summer, before the year 2050 (SIMIP Community, 2020). Another striking discovery is that the Arctic shelf seas are expected to become seasonally ice free in the current decade (Onarheim et al., 2018).

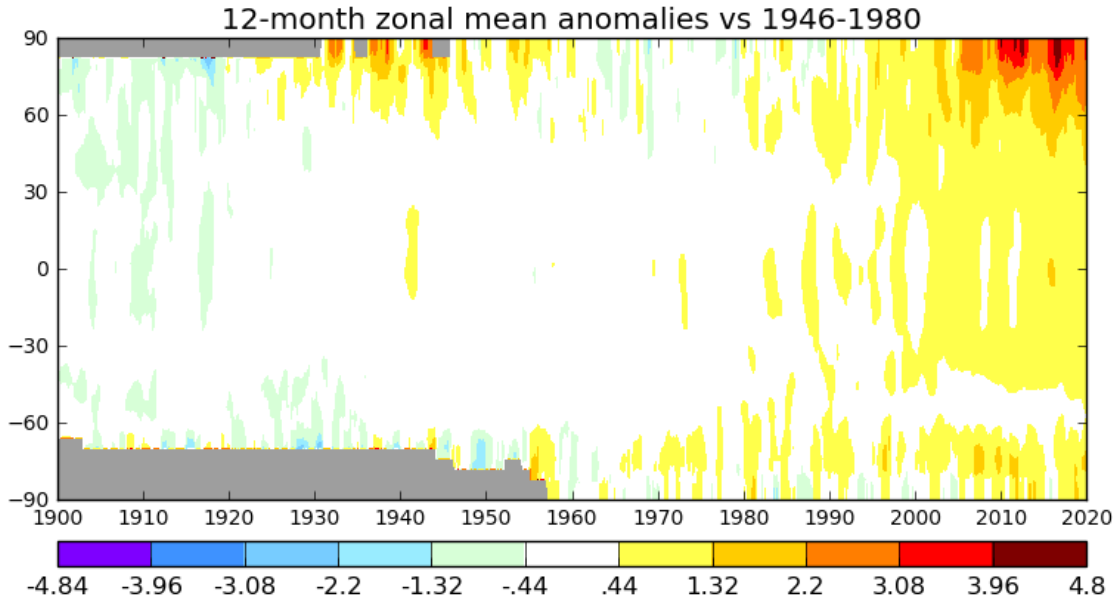


FIGURE 1.1: Time series of annual mean surface air temperature anomalies, zonally averaged, with respect to the 1946–1980 period. Data come from the Land-Ocean-Temperature index (LOTI) and the NOAA/NCEI’s Extended Reconstructed Sea Surface Temperature (ERSST) v5. The unit in the colorbar is  $^{\circ}\text{C}$ , while the y axis denotes latitudes. Credit for the data and the figure: NASA Goddard Institute for Space Studies, available at: [https://data.giss.nasa.gov/gistemp/zonal\\_means/index.html](https://data.giss.nasa.gov/gistemp/zonal_means/index.html)

The Arctic is a region susceptible to various feedback mechanisms, like the sea ice albedo, water vapor, and temperature lapse rate feedback (Pithan and Mauritsen, 2014). Sea ice melting, due to rising air temperatures, decreases the surface albedo and increases the absorption of solar radiation by the ocean (Serreze and Barry, 2011). From 1979 to 2011, the Arctic albedo has decreased from 0.52 to 0.48, followed by an additional solar energy input of  $6.4 \text{ W m}^{-2}$  into the Arctic Ocean (Pistone, Eisenman, and Ramanathan, 2014). Larger open water regions increase air-sea heat exchange, intensify surface evaporation, and enhance the warming of the adjacent air (Bintanja and Andry, 2017).

Although the global mean precipitation is expected to increase by only 2% per degree of global warming (Held and Soden, 2006), the projected trends in the Arctic (4.5% per degree of temperature change) are much larger (Bintanja and Selten, 2014). Apart from the net precipitation increase, the warming in the Arctic also contributes to the thawing of the upper permafrost and the thermal erosion of the shorelines (Grosse

et al., 2016).

The aforementioned changes are accompanied by observed increases in freshwater discharge to the Arctic Ocean. Observations from the 2003-2005 period reveal rates of Pan-Arctic freshwater discharge in the order of 3600 km<sup>3</sup> per year (Syed et al., 2007). During the period from 1936 to 1999, the discharge from the six largest rivers of the Eurasian basin has increased by 7% (Peterson et al., 2002). Likewise, recent observational records from 19 large Arctic rivers show a consistent increase (9.8%) in the annual discharge over 30 years (1977-2007) (Overeem and Syvitski, 2010). Climate models project a discharge increase in the order of 5 to 25%, compared to 2000, by the year 2100 (Walsh, 2005).

In the northern hemisphere's permafrost regions soil stores approximately 50% of the estimated global subterranean organic carbon pool (Tarnocai et al., 2009). The progressive permafrost thawing, accompanied by increased precipitation and freshwater discharge, is expected to result in higher loads of dissolved organic matter (DOM) and suspended matter entering the Arctic Ocean. In five major Arctic rivers (Yenisey, Lena, Ob, Mackenzie, and Yukon), increasing discharge is linked to significantly elevated DOM concentrations, with a total annual flux of 16 teragrams (Tg) (Raymond et al., 2007). Overall, estimates of the total input of DOM to the Arctic Ocean are between 25 and 36 Tg (Raymond et al., 2007). Under a warming Arctic climate, the DOM flux to the Arctic Ocean in West Siberia, is expected to increase by 29 to 46% in 2100 (Frey and Smith, 2005).

Increased riverine DOM loading to the Arctic Ocean involves a broad range of physical and biogeochemical implications. A fraction of DOM is an optically active water constituent that absorbs ultraviolet (UV, 290 – 400 nm) and visible light (VIS, 400 – 700 nm) efficiently (Roesler and Perry, 1995) and is referred to, as coloured or chromophoric dissolved organic matter (CDOM). In the western Arctic Ocean, CDOM light absorption is responsible for almost 76% of the total non-water absorption in the 443 nm wavelength, whereas phytoplankton and Non-Algal Particles (NAP) absorption contribute by about 16% and by less than 1%, respectively. In the eastern and central Arctic Ocean, CDOM may account for up to 85% of the total non-water absorption, while phytoplankton and NAP for 12% and 3%, respectively (Gonçalves-Araujo et al., 2018).

The presence of high CDOM concentrations in the Arctic waters leads to enhanced absorption of solar energy in the mixed layer (Pegau, 2002; Hill, 2008; Granskog et al., 2015; Kim, Gnanadesikan, and Pradal, 2016; Soppa et al., 2019). Moreover, it has been reported that particle absorption can equally (to CDOM) contribute to the observed enhanced summer warming of surface waters in the Chukchi Sea (Hill, 2008). By increasing the surface water temperature, CDOM has the potential to significantly contribute to the sea ice retreat (Hill, 2008; Soppa et al., 2019; Pefanis et al., 2020). Likewise, it reduces the photosynthetically available radiation (PAR) that phytoplankton in the Arctic is so much dependant on. On the other hand, it may reduce the UV light at the surface that is harmful for aquatic organisms (Stedmon and Markager, 2001). CDOM by influencing the optical properties of seawater, has also important implications for remote sensing algorithms, and thus, for the monitoring of the Arctic Ocean (Heim et al., 2014).

Although a major source of CDOM in the river-influenced Arctic shelf seas, is the degradation of plant material of terrestrial origin (allochthonous), in the oceanic environment, CDOM mainly originates from aquatic primary producers (autochthonous), namely the phytoplankton (Stedmon and Markager, 2001). Phytoplankton, apart from being the foundation of the marine food chain, is of pivotal importance for carbon fixation. Besides representing less than 1% of the Earth's photosynthetic biomass, it has been estimated that this marine microalgae is responsible for almost half of the Earth's photosynthesis (Field et al., 1998).

During the last 20 years (1998-2018), the changes in the Arctic system have been accompanied by a 57% increase of phytoplankton primary production (Lewis, Dijken, and Arrigo, 2020). Moreover, the delayed freeze-up of sea ice and the ocean's exposure to atmospheric forcing are linked to the more frequent development of a second phytoplankton bloom in fall (Ardyna et al., 2014). Phytoplankton productivity is also associated with the nutrient supply by advection (Popova et al., 2013), whose recent increase is responsible for the northward expansion of phytoplankton in the Atlantic sector (Oziel et al., 2020).

The ongoing climate change in the Arctic indicates major changes in the phytoplankton abundance and composition in the future. Apart from its biogeochemical

implications, phytoplankton strongly absorbs the penetrating solar radiation; a process that is spectrally varying according to its composition (further discussed in Section 1.2.2). Early studies (Lewis et al., 1990; Siegel et al., 1995) based on *in situ* measurements and satellite remote sensing showed that high chlorophyll-a concentrations (indicator of phytoplankton biomass) were associated with increased radiative heating in the upper ocean. In the Arctic, biologically-induced surface warming, by enhancing sea ice melting, increases light availability for phytoplankton, which in turn may amplify the warming (Lengaigne et al., 2009).

In numerical ocean general circulation models, the penetration of solar radiation needs to be parameterized. The choice of parameterization may affect the circulation significantly, as well as the upper ocean water masses (Cahill et al., 2008) and their transformation rates (Groeskamp and Iudicone, 2018). Compared to parameterizations with constant light attenuation depths, numerical models with interactive biogeochemistry simulate higher sea surface temperatures (SST) that are related to stronger absorption by high chlorophyll-a concentrations (Oschlies, 2004; Manizza et al., 2005; Wetzel et al., 2006; Lengaigne et al., 2009; Patara et al., 2012). Nevertheless, most of the existing knowledge is based on studies focusing on other parts of the global ocean, and particularly in mid-latitude and tropical regions (e.g. Oschlies, 2004; Marzeion et al., 2005; Groeskamp and Iudicone, 2018). Apart from the limited research in the Arctic Ocean, the vast majority of the studies accounting for the effect of biogeochemistry investigated solely the effect of phytoplankton (Manizza et al., 2005; Lengaigne et al., 2009; Patara et al., 2012; Park et al., 2015). In a step forward, Kim, Pradal, and Gnanadesikan (2015) parameterized light absorption due to CDOM and detritus in an Earth system model by prescribing interannually-averaged and vertically constant absorption estimates from satellite data. This method, however, does not resolve important aspects of the seasonal cycle nor the feedback of increasing surface temperature and modified ocean dynamics on the distribution of CDOM, and hence the absorption. In this study, CDOM is incorporated as a prognostic model variable in the underwater light attenuation scheme so that it interacts with the changes induced by its presence. Based on this interactive model configuration, this thesis aims to address two of the research questions defined in Section 1.3.

## 1.2 Theoretical background

### 1.2.1 Inherent optical properties

When photons interact with water there can be two cases. The photons may disappear, and their energy will be converted to another form (such as heat), a process called absorption. Otherwise, the photons may change their direction and/or wavelength, a process called scattering. For understanding the fate of solar radiation as it passes through the air-sea interface into water, we need a measure of the extent to which water absorbs and scatters light.

The water's light absorption and scattering properties at any wavelength are described by its inherent optical properties (IOPs). The IOPs comprise the absorption coefficient  $\alpha(\lambda)$ , the scattering coefficient  $b(\lambda)$  and the volume scattering function  $\beta$ . The magnitudes of the IOPs depend only on the properties of the medium - in the case of seawater on its constituents - and not on the ambient light environment. An important feature of IOPs is that they are conservative properties, therefore, the absorption and scattering coefficients of the various in-water constituents are independent and, thus, can be treated additively.

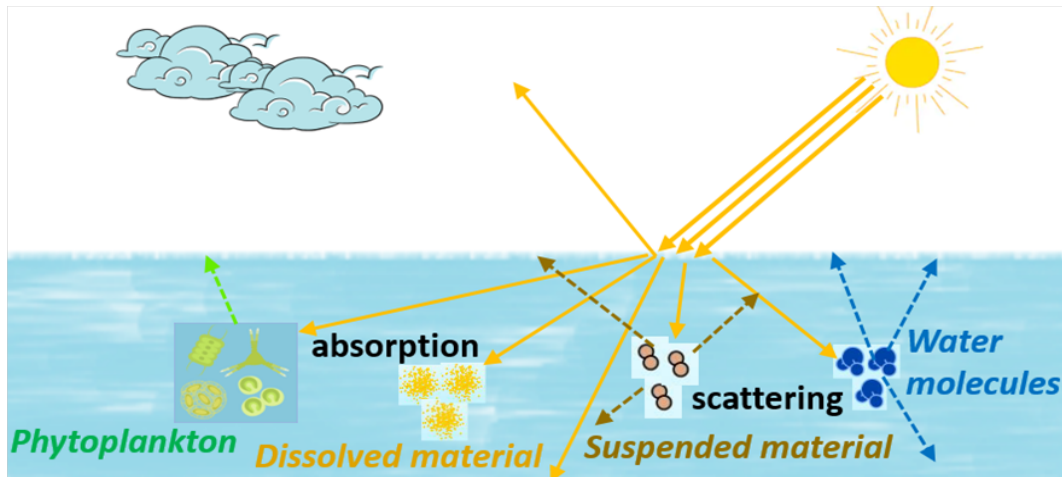


FIGURE 1.2: A schematic showing the optically active water constituents which absorb or scatter the incoming solar radiation.

### 1.2.2 Optically-active water constituents

Light is attenuated in the ocean through its scattering and absorption by optical constituents such as seawater itself, phytoplankton, CDOM, and suspended material (or non-algal particles) (Fig. 1.2). Since IOPs can be treated additively, the total absorption within seawater  $\alpha(\lambda)$  ( $\text{m}^{-1}$ ) is the sum of the absorption by each individual component (Fig. 1.3):

$$\alpha(\lambda) = \alpha_w(\lambda) + \alpha_{ph}(\lambda) + \alpha_{CDOM}(\lambda) + \alpha_{NAP}(\lambda) \quad (1.1)$$

where  $\alpha_w(\lambda)$  is the wavelength dependent absorption coefficient of seawater,  $\alpha_{ph}(\lambda)$  of phytoplankton,  $\alpha_{CDOM}(\lambda)$  of CDOM, and  $\alpha_{NAP}(\lambda)$  of non-algal particles.

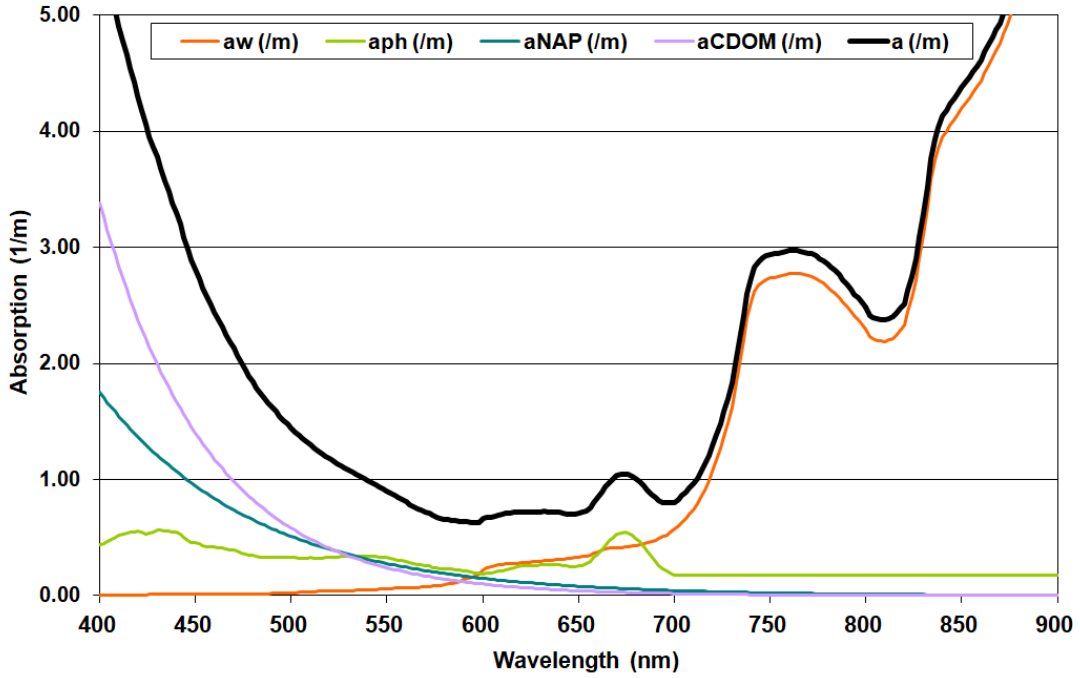


FIGURE 1.3: Spectral absorption coefficients ( $\text{m}^{-1}$ ) of water (aw), phytoplankton (aph, for a chlorophyll-a concentration of  $30 \text{ mg/m}^3$ ), NAP (aNAP, for a concentration of  $25 \text{ g/m}^3$ ), CDOM (aCDOM, for a CDOM absorption of  $1.6 \text{ m}^{-1}$  at  $443 \text{ nm}$ , and the sum of them (a).

Similarly to the absorption, the total scattering within seawater  $b(\lambda)$  ( $\text{m}^{-1}$ ) is the sum of the scattering by every component:

$$b(\lambda) = b_w(\lambda) + b_{ph}(\lambda) + b_{NAP}(\lambda) \quad (1.2)$$

where  $b_w(\lambda)$  is the wavelength dependent scattering coefficient of seawater,  $b_{ph}(\lambda)$  of phytoplankton, and  $b_{NAP}(\lambda)$  of non-algal particles. The contribution of CDOM to scattering is usually assumed to be negligible.

The aforementioned optically active water constituents and their properties are briefly described below.

## Seawater

Seawater both absorbs and scatters the incoming solar radiation. Its colour is attributed to the very weak absorption of green and blue light. Its absorption gradually starts to increase for wavelengths longer than 550 nm and becomes dominant in the red and infrared part of the spectrum (Fig. 1.3). Additionally, strong absorption may occur in the UV part, owing to the presence of dissolved oxygen (Kirk, 2011). Although water's absorption dependency on temperature is insignificant below 550 nm, the effect of temperature and ions concentration (salinity) may be non-negligible at longer wavelengths and higher temperatures (Röttgers, McKee, and Utschig, 2014). The scattering of light by seawater originates from fluctuations in the dielectric constant, due to the randomness of molecules motion. Similarly to absorption, scattering depends on temperature and salinity, as well as on the polarization of light (Buiteveld, Hakvoort, and Donze, 1994).

## Phytoplankton

Phytoplankton consists of various photosynthetic pigments (e.g. chlorophylls, biliproteins, and carotenoids) that absorb solar radiation mostly in the 400-500 and 650-700 nm wavelength bands (Fig. 1.3), but also in the UV wavelength range (Morrison and Nelson, 2004) (Fig. 1.4). Phytoplankton's spectral absorption characteristics are defined by their pigment composition and physiological state (Bricaud et al., 2004). As shown in Figure 1.4, every pigment exhibits unique absorption features. Among those pigments, chlorophylls exist in all phytoplankton cells, and cause two main absorption peaks. The primary peak is at the blue band (440 nm), while the secondary peak is met in the red part of the absorption spectra (675 nm). When other pigments are present, more absorption peaks may appear, or the absorption maximum in the



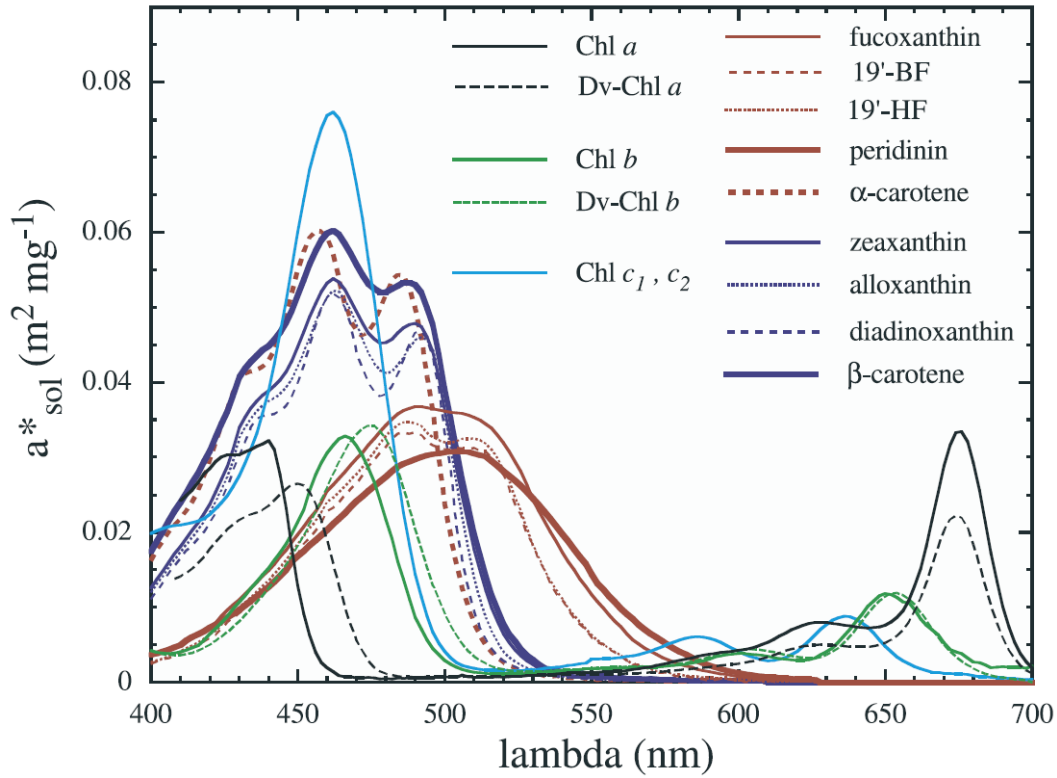


FIGURE 1.4: Weight-specific absorption spectra of the main phytoplankton pigments,  $a^*_{\text{sol}}$  (in  $\text{m}^2 \text{mg}^{-1}$ ). Absorption spectra of photosynthetic and non-photosynthetic carotenoids are shown in red and blue, respectively. Credit: Figure from Bricaud et al. (2004).

blue band may broaden.

Apart from absorption, phytoplankton contributes to the scattering of sunlight in the ocean. The extent of scattering depends on many factors, such as, the cell size, the shape, and the refractive index of its components, and thus, varies among species. When compared to particles, the scattering coefficients of phytoplankton are relatively low, except for coccolithophores (Bricaud, Bédhomme, and Morel, 1988).

## CDOM and Non-Algal Particles

CDOM is the optically measurable, or coloured, fraction of DOM and it is an important constituent in seawater. It can be quantified from the absorption or fluorescence of the material passing through a filter with pore size of approximately 0.2

$\mu\text{m}$ . CDOM comes from the degradation of plant material of both aquatic and terrestrial origin and comprises a complex group of chemical compounds mostly referred to as humic substances (Kirk, 2011). Its composition, however, differs based on the sources. Primary terrestrial sources (allochthonous) of CDOM are the rivers, which carry material from soils to the nearshore regions, while in open ocean regions *in situ* biological production (autochthonous) is the primary source (Coble, 2007).

As discussed in Section 1.1, CDOM highly absorbs ultraviolet (290–400 nm) and visible light (400–700 nm) (Roesler and Perry, 1995). A typical absorption spectrum is characterized by an approximately exponential decline towards longer wavelengths, with very low or zero absorption at the red end of the visible spectrum (Fig. 1.3). CDOM absorption spectra can be described by the following exponential function:

$$\alpha_{CDOM}(\lambda) = \alpha_{CDOM}(\lambda_0)e^{-S(\lambda-\lambda_0)} \quad (1.3)$$

where  $\alpha_{CDOM}(\lambda_0)$  is the light absorption coefficient at a reference wavelength ( $\lambda_0$ ) and  $S$  is the slope of the absorption spectrum within a given wavelength range. The ratios of absorption at different wavelength bands, which are independent of CDOM concentration, are used as indicators of its composition and origin.

Besides phytoplankton and CDOM, suspended material, or Non-Algal Particles, are also known to strongly absorb solar radiation. The absorption spectra of NAP ( $\alpha_{NAP}$ ) is very similar in form to that observed for CDOM (Fig. 1.3), and can be also expressed as an exponential decay:

$$\alpha_{NAP}(\lambda) = \alpha_{NAP}(\lambda_0)e^{-S(\lambda-\lambda_0)} \quad (1.4)$$

NAP may include heterotrophic organisms like bacteria, cells from phytoplankton and zooplankton, as well as mineral particles of both terrestrial (e.g. clays) and biogenic origin (e.g. shells). These particles are responsible for most of the in-water scattering in the majority of natural waters. The slope of the scattering spectrum ( $S_b$ ) can be represented by a power function:

$$b_{NAP}(\lambda) = b_{NAP}(\lambda_0) \left( \frac{\lambda}{\lambda_0} \right)^{-S_b} \quad (1.5)$$

where the selection of the reference wavelength ( $\lambda_0$ ) varies among studies (e.g. 442,

550 nm).

### 1.2.3 Apparent optical properties

The apparent optical properties (AOPs) depend both on the medium (IOPs) and the structure of the light field and are widely used for describing optically the water body. Following the nomenclature of Kirk (2011), a fundamental AOP is the surface radiance  $L(\theta, \phi)$  [W m<sup>-2</sup>] in a particular wavelength, which is the radiant flux of energy ( $dQ/dt$ ) in a given direction, per unit solid angle ( $d\omega$ ), per unit projected area ( $dS \cos \theta$ ):

$$L(\theta, \phi) = \frac{dQ}{dt dS \cos \theta d\omega} \quad (1.6)$$

The angular structure of the light field is expressed in terms of  $\theta$  and  $\phi$ , which denote the zenith and azimuth angle respectively. From the radiance another useful AOP can be derived, the plane parallel irradiance. At a specific point at the sea surface, the downwelling irradiance  $I_d$  can be obtained by integrating with respect to solid angle over the whole upper hemisphere:

$$I_d = \int_{2\pi} L(\theta, \phi) \cos \theta d\omega \quad (1.7)$$

In the same way, and by integrating over the lower hemisphere, the upwelling irradiance  $I_u$  can be derived:

$$I_u = \int_{-2\pi} L(\theta, \phi) \cos \theta d\omega \quad (1.8)$$

The difference between  $I_d$  and  $I_u$  is the net downwelling irradiance  $I$ :

$$I = \int_{4\pi} L(\theta, \phi) \cos \theta d\omega \quad (1.9)$$

In the ocean, the penetrating radiation diminishes with depth  $z$  following approximately an exponentially decaying function:

$$I(z, \lambda) = I_0(\lambda) e^{\int_0^z -K_d(z, \lambda) dz}. \quad (1.10)$$

where  $I_0(\lambda)$  is the net irradiance just before entering the water and  $K_d(\lambda)$  is the spectral diffuse attenuation coefficient for the net downwelling irradiance. The  $K_d$  is one of the most commonly used AOPs and it can be defined as:

$$K_d(z, \lambda) = -\frac{d \ln I(z, \lambda)}{dz} = -\frac{1}{I(z, \lambda)} \frac{dI(z, \lambda)}{dz} \quad (1.11)$$

A discretized version of the Equation 1.10, accounting for the  $K_d$ , is used in ocean general circulation models to parameterize the rate of change of the net irradiance with depth.

In ocean colour remote sensing (OCRS), the inherent properties of seawater can be inferred from AOP quantities like the remote sensing reflectance  $R_{rs}(\lambda)$  [sr<sup>-1</sup>]:

$$R_{rs}(\theta, \phi, \lambda) = \frac{L_w(\theta, \phi, \lambda)}{I_d(\lambda)}. \quad (1.12)$$

where  $L_w$  [W m<sup>-2</sup>] is the water-leaving radiance. The magnitude and the spectral shape of  $L_w$  provides valuable insights on the type and concentration of optically active constituents in seawater. The retrieval of this information becomes possible with the deployment of bio-optical algorithms, either empirical or semi-analytical.

#### 1.2.4 Radiative transfer theory

The radiative transfer equation (RTE) describes the behavior of radiance within a medium. Following the nomenclature of the [Ocean Optics Web Book](#) (accessed on January 2021 according to the [2020 Creative Commons Attribution license](#)), the light field can be considered in the form of many beams of electromagnetic radiation of various wavelengths passing in all directions through each point of the medium. A single beam of radiance  $L$  and wavelength  $\lambda$  is propagating in a direction  $(\theta, \phi)$ , as shown in Figure 1.5. The processes affecting the beam are:

- 1) Loss of photons from the beam through extinction of the light by conversion of radiant energy to non-radiant energy (absorption)
- 2) Loss of photons from the beam through scattering towards other directions without change in wavelength (elastic scattering)

- 3) Loss of photons from the beam through scattering with change in wavelength (inelastic scattering)
- 4) Gain of photons by the beam through scattering from other directions without change in wavelength (elastic scattering)
- 5) Gain of photons by the beam through scattering from other directions with change in wavelength (inelastic scattering)
- 6) Gain of photons by the beam through creation of photons by conversion of non-radiant energy into radiant energy (emission)

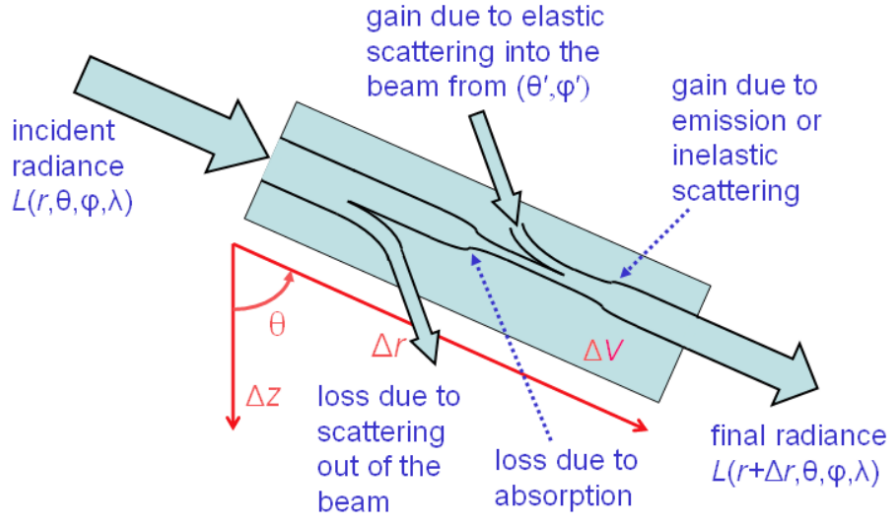


FIGURE 1.5: Illustration of a single beam of radiance and the processes affecting it as it propagates a distance  $\Delta r$ . Source: <http://www.oceanopticsbook.info>.

These six processes will be given quantitative forms, so they can be expressed in the RTE. A beam of initial radiance  $L(r)$  propagating from point  $r$  to the point  $r + \Delta r$ , will then have radiance  $L(r + \Delta r)$ . The change in radiance, due to absorption, will be proportional to the incident radiance and can be written as:

$$\frac{\Delta L(r + \Delta r, \theta, \phi, \lambda)}{\Delta r} = -\alpha(r, \lambda) L(r, \theta, \phi, \lambda) \quad (1.13)$$

The minus sign in Eq. 1.13 denotes the decrease of radiance, while  $\alpha(r, \lambda)$  is the proportionality constant, namely the absorption coefficient at wavelength  $\lambda$ .  $\alpha$  accounts both for the energy converted to non-radiant form ("true" absorption) and for the energy that is redistributed to different wavelengths (inelastic scattering).

Similarly, the loss due to elastic scattering can be written as:

$$\frac{\Delta L(r + \Delta r, \theta, \phi, \lambda)}{\Delta r} = -b(r, \lambda)L(r, \theta, \phi, \lambda) \quad (1.14)$$

where  $b(r, \lambda)$  is the scattering coefficient.

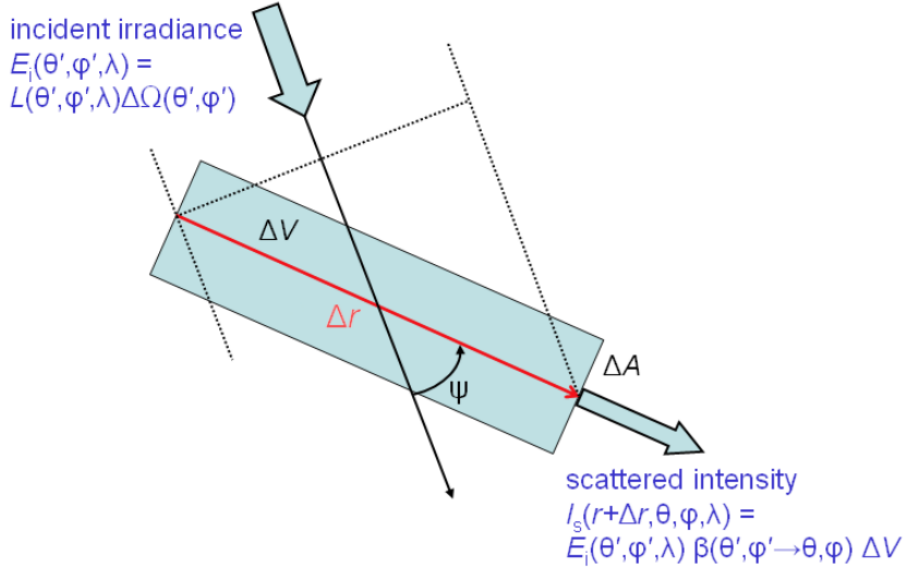


FIGURE 1.6: Illustration of a beam of radiance in direction  $(\theta', \phi')$  generating radiance in the direction of interest  $(\theta, \phi)$  by elastic scattering.

Source: <http://www.oceanopticsbook.info>.

The ambient light may be scattered elastically from other directions towards the beam direction  $(\theta, \phi)$  (Fig. 1.6). The integrated contribution from every direction, along the path length  $\Delta r$ , can be formulated as:

$$\frac{\Delta L(r + \Delta r, \theta, \phi, \lambda)}{\Delta r} = \int_0^{2\pi} \int_0^\pi L(\theta', \phi', \lambda)\beta(\theta', \phi' \rightarrow \theta, \phi; \lambda)\sin(\theta')d\theta'd\phi' \quad (1.15)$$

where  $\beta(\theta', \phi' \rightarrow \theta, \phi; \lambda)$  is the spectral volume scattering function.

Moreover, and for simplicity, a generic source function  $S$  representing the gain by any inelastic scattering from other wavelengths or emission process, can be introduced. However, each process like fluorescence by chlorophyll or CDOM, or Raman scattering by water molecules, needs a separate mathematical formulation to specify  $S$ .

$$\frac{\Delta L(r + \Delta r, \theta, \phi, \lambda)}{\Delta r} = S(r, \theta, \phi, \lambda) \quad (1.16)$$

Summarizing, the net change in radiance with distance, due to all six aforementioned processes, is the sum of the individual contributions of Eqs. 1.13 to 1.16. Changes arise from the optical properties of the medium and the ambient radiance in other directions:

$$\begin{aligned} \frac{\Delta L(r + \Delta r, \theta, \phi, \lambda)}{\Delta r} = & - [a(r, \lambda) + b(r, \lambda)]L(r, \theta, \phi, \lambda) \\ & + \int_0^{2\pi} \int_0^\pi L(\theta', \phi', \lambda) \beta(r; \theta', \phi' \rightarrow \theta, \phi; \lambda) \sin(\theta') d\theta' d\phi' \\ & + S(r, \theta, \phi, \lambda) \end{aligned} \quad (1.17)$$

For applications in oceanography, a  $z$ -coordinate system is normally used, where  $z$  is the depth with respect to the mean sea surface and is positive downward. According to Figure 1.5, changes in  $r$  are related to changes in  $z$  as  $dr = dz/\cos\theta$ . Assuming horizontal homogeneity for the ocean, Eq. 1.17 can be rewritten:

$$\begin{aligned} \frac{\cos\theta \Delta L(z + \Delta z, \theta, \phi, \lambda)}{\Delta z} = & - [a(z, \lambda) + b(z, \lambda)]L(z, \theta, \phi, \lambda) \\ & + \int_0^{2\pi} \int_0^\pi L(\theta', \phi', \lambda) \beta(z; \theta', \phi' \rightarrow \theta, \phi; \lambda) \sin(\theta') d\theta' d\phi' \\ & + S(z, \theta, \phi, \lambda) \end{aligned} \quad (1.18)$$

## 1.3 Scope of the thesis

Considering Arctic Amplification and the emerging ice-free waters during the Arctic summer, the in-water constituents able to attenuate the solar radiation have become more relevant than ever. This thesis aims to expand our current knowledge on the radiative effect of CDOM and the other optically active water constituents in the Arctic Mediterranean Sea.

As a first step, I investigate the potential of CDOM and suspended material in enhancing the radiative heating and the sea ice melting in the Laptev Sea, a shelf region heavily influenced by one of the largest river systems in the Arctic and the world. Despite its importance, the Laptev Sea, like most of the Arctic coastal regions, is operationally challenging resulting in limited observations, and hence, knowledge on the constituents' distribution and radiative effect. By exploiting ocean colour satellite retrievals in synergy with radiative transfer modelling it became possible for the first time to quantify the summertime spatial distribution of the radiative heating in the Laptev Sea.

As a next step, I upscale this one-dimensional and regional study by means of general circulation modelling for the entire Arctic Ocean and the subarctic seas. Building upon previous advances, the effect of CDOM, as a prognostic model variable, is incorporated for the first time into the scheme of the in-water shortwave radiation penetration. That way, CDOM interacts with the changes induced by its presence.

Within this context, the current thesis addresses the following three key research questions:

- Q1: What is the role of CDOM and total suspended matter in the radiative heating in the shelf waters of the Laptev Sea?
- Q2: How does the light attenuation by phytoplankton and CDOM contribute to the radiative heating and sea ice reduction in the Arctic Mediterranean Sea?



- Q3: How do changes in light attenuation due to CDOM affect biogeochemistry and the ecosystem?

The above research questions are answered by means of two model frameworks: the one-dimensional coupled ocean-atmosphere radiative transfer model **SCIATRAN** and the three-dimensional ocean general circulation model with biogeochemistry **Darwin-MITgcm**, in a global configuration.

## 1.4 Thesis outline

The current thesis is organized in 6 chapters, as follows:

Chapter 1 introduces the reader to the topic and briefly describes the relevant scientific background. It introduces the basic principles of Ocean Optics and radiative transfer theory.

Chapter 2 consists of two parts. In the first part, the methods applied and the data used for the radiative transfer model (SCIATRAN) simulations are described. The second part follows with a description of the utilized general circulation model (Darwin-MITgcm), and the relevant to Chapters 4 and 5 methodology.

Chapter 3 investigates the effect of CDOM and the other optically active water constituents on the radiative heating in the shelf waters of the Laptev Sea. This chapter is based on the study published in *Frontiers in Marine Science* (Soppa et al., 2019).

Chapter 4 is based on the study published in *Geophysical Research Letters* (Pefanis et al., 2020). By operating a numerical ocean model with biogeochemistry and sea ice (Darwin-MITgcm), the total, as well as the individual effects of phytoplankton and CDOM on light attenuation are examined. Furthermore, the implications of considering CDOM absorption, in surface warming and sea ice loss, are discussed. This is followed by a discussion on the contribution of the heat budget terms, and on the light

attenuation schemes in ocean models.

In Chapter 5 the effect of CDOM light absorption on the biogeochemical properties of the Arctic Ocean is examined. More specifically, the effect on phytoplankton growth, CDOM concentration, and macronutrients is discussed. Finally, the chapter shows the changes in the phytoplankton bloom (phenology) and in its growth limiting factors.

Chapter 6 summarizes the main findings and conclusions of the thesis along with an outlook for future research.

Annotations:

- *The Arctic Mediterranean Sea comprises the Arctic Ocean and the Greenland, Iceland and Norwegian (the Nordic) Seas.*
- *Throughout the thesis, the terms suspended material (SM), total suspended matter (TSM), and Non-Algal Particles (NAP) are used interchangeably. Similarly, in chapters 4 and 5, the terms light absorption and light attenuation are also used interchangeably, since scattering is not parameterized within the model.*

## Chapter 2

# Materials and methods

## 2.1 Radiative transfer model simulations

### 2.1.1 *In situ* data

The *in situ* dataset is composed of measurements of the CDOM absorption coefficient spectra ( $a_{\text{CDOM}}$ ), total suspended matter (TSM), chlorophyll-a (Chla), temperature and salinity taken during two Russian-German expeditions to the Laptev Sea. The expeditions TRANSDRIFT-XVII and TRANSDRIFT XIX took place from August 31 to October 9, 2010 and from August 25 to September 7, 2011, respectively. The sampling locations include large parts of the western and central Laptev Sea shelf, as well as coastal regions close to the Lena River Delta (Figure 2.1).

For validation of Chla and  $a_{\text{CDOM}}$  at 443 nm ( $a_{\text{CDOM}443}$ ) satellite products, surface measurements (first 2 m of the water column) from both expeditions were used. No radiometric measurements were taken during these expeditions. For evaluation of the RTM SCIATRAN and further RTM simulations, data from TRANSDRIFT-XVII were used. RT simulations were carried out using vertically resolved data of  $a_{\text{CDOM}}$  spectra, TSM, Chla, temperature and salinity (Section 2.1.5). Chla, temperature and salinity were measured every 1 m, whereas the vertical resolution of  $a_{\text{CDOM}}$  and TSM varied among the stations. A detailed description of water sampling and analysis for the TRANSDRIFT-XVII expedition can be found in Heim et al., 2014. The TRANSDRIFT XIX expedition was carried out with the same methodology of water sampling, analysis and instrumentation as for TRANSDRIFT-XVII. The data is available at: <https://doi.pangaea.de/10.1594/PANGAEA.897894>.

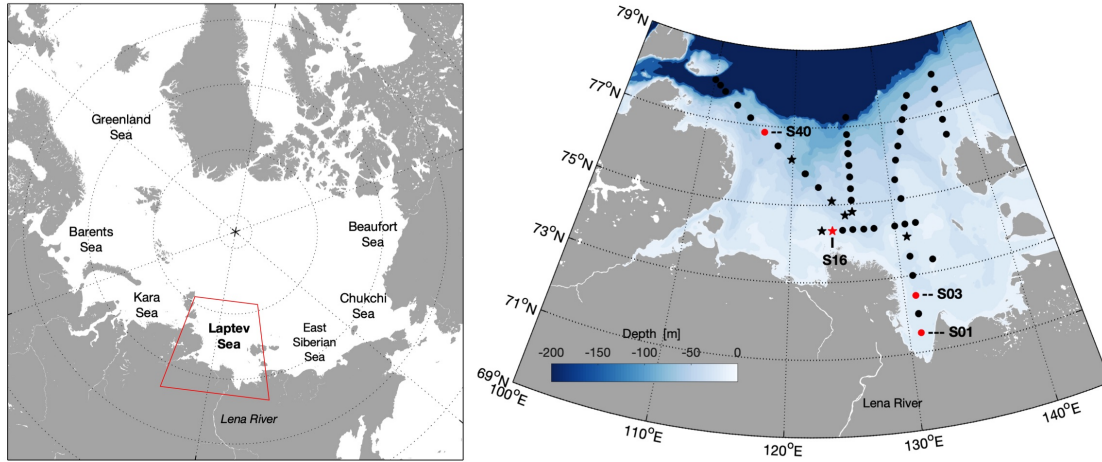


FIGURE 2.1: Study area and location of sampling stations of the TRANSDRIFT-XVII and TRANSDRIFT-XIX expeditions (black). Stations used for the radiative transfer simulations are in red and stations matched with the satellite data are marked as stars.

### 2.1.2 Ocean colour remote sensing retrievals

Daily MERIS Level 1b data of reduced resolution (1.2 km) were obtained for August and September 2010 and 2011, when the TRANSDRIFT expeditions took place (Section 2.1.1). The data were processed with the C2RCC and C2X algorithms that are based on a large database of radiative transfer simulations inverted by neural networks (Brockmann et al., 2016). C2X is a modified version of C2RCC with neural networks that have been trained for extreme ranges of the scattering and the absorption coefficients. The algorithms split into two major parts. A first set of neural nets is used to perform the atmospheric correction, getting the top of atmosphere radiances ( $L_{TOA}$ ) from the sensor and providing the water leaving radiances ( $L_W$ ). The second set of nets retrieves inherent water optical properties ( $a_{ph}(443)$ ,  $a_{CDOM}(443)$ , absorption coefficient of detritus at 443 nm, scattering coefficient of marine particles at 443 nm and scattering coefficient of white particles at 443 nm) and apparent optical properties (e.g. irradiance attenuation coefficient at 489 nm) from the  $L_W$ . Chlorophyll-a concentration (Chla) is determined from  $a_{ph}(443)$  using a scaling factor of 21. The Chla product was also modified using a Chla scaling factor of Örek et al. (2013) ( $Chla=7.8 a_{ph}(442)$  assuming  $a_{CDOM}(442) = a_{CDOM}(443)$ ) derived from measurements carried out in the Lena River in June and July 2011, hereafter called C2RCC Laptev Sea.

To compare the satellite products and in situ measurements the root mean squared

error (RMSE), bias, slope and determination coefficient were used (for Chla in log 10 space). To derive high quality match-ups, we (jointly with Dr. Mariana Soppa) checked the spatial homogeneity over a 3 x 3 pixel box centered on the location of the in situ data (for satellite and in situ data taken on the same day). Following Bailey and Werdell (2006), match-ups were regarded as valid if more than 50% of the nine pixels were not flagged after applying the atmospheric correction (AC) flags (Rtosa\_OOS, Rtosa\_OOR, Rhov\_OOR, and l1\_flags) and if the median coefficient of variation (ratio of the standard deviation to the median value) of the remaining pixels was lower than 0.15 in remote sensing reflectances at 412, 443, 490, and 560 nm. The median values of Chla and  $a_{CDOM}(443)$  were then used for comparison with the in situ data.

### 2.1.3 Model description (SCIATRAN)

The coupled atmosphere–ocean radiative transfer model (RTM) SCIATRAN release version 3.7.1 (Rozanov et al., 2002; Rozanov et al., 2014; Rozanov et al., 2017) was used for the radiative heating simulations. SCIATRAN is freely available at <http://www.iup.physik.uni-bremen.de/sciatran> along with a detailed User’s Guide. The model covers a spectral range from 0.18 to 40  $\mu\text{m}$ , while simulations were carried out from 0.3 to 0.9  $\mu\text{m}$ . The radiative transfer equation was solved by means of the scalar discrete ordinate technique, while the model was run in pseudo-spherical mode, where the attenuation of the direct solar light is calculated in a spherical atmosphere and all scattering processes are solved in a plane-parallel atmosphere.

The atmospheric model of SCIATRAN includes thermal emission, absorption by several trace gases, Rayleigh scattering and scattering by aerosol and cloud particles. The ocean surface reflection properties are described by the bidirectional reflection function taking into account Fresnel effects and a wind roughened ocean-atmosphere using wind speed values derived from MERIS L1b data and extracted using SNAP (represents the wind speed at 10 m height). The solar spectrum is derived from the MODerate spectral resolution atmospheric TRANsmittance algorithm and computer model (MODTRAN) 3.7 for a spectral range from 300 to 900 nm interpolated (1 nm) and convolved with a Gaussian full width at half maximum function. For the trace

gases I used the spectral parameters and the climatologies provided by HITRAN 2012 database. The aerosol properties were selected as in Rozanov et al. (2017). The aerosol optical thickness (AOT) was set to 0.09 at the 500 nm reference wavelength, based on measurements from the Aerosol Robotic Network (AERONET) site in Tiksi (71.6°N, 128.9°E) at the shore of the Laptev Sea. Rotational Raman scattering and polarization effects were not included in the simulations.

The ocean model consists of biooptical models as described in Blum et al. (2012). Chlorophyll-a specific phytoplankton absorption coefficient is based on Prieur and Sathyendranath (1981) and Haltrin (2006), and mass-specific absorption spectrum of non-algal particles based on Örek et al. (2013). The pure water absorption ( $a_w$ ) spectrum is a merged spectrum based on Smith and Baker, 1981 for 200-300 nm with transition to Sogandares and Fry, 1997 between 300-340 nm, Sogandares and Fry (1997) for 340-380 nm, Pope and Fry (1997) for 380-725 nm, Smith and Baker (1981) for 725-800 nm and Segelstein (1981) for 800-1150 nm. Following Röttgers, McKee, and Utschig (2014), a correction to account for the dependency of light absorption coefficient on seawater temperature and concentration of ions (i.e. the salinity of seawater) was further implemented. A wavelength independent refractive index of seawater, equal to 1.338, is also considered. The pure seawater volume scattering function (VSF) is estimated according to the approximation of Buiteveld, Hakvoort, and Donze (1994), which describes scattering resulting from density and temperature fluctuations in the medium.

The scattering properties of the particulate matter in the water follow the approximation proposed by Kopelevich (1983) with the concentrations of small and large particles determined following Haltrin (1999). No effects of vibrational Raman scattering and fluorescence by CDOM or Chlorophyll-a are included in the simulations. Finally, the pure seawater depolarization ratio is set equal to 0.09 at atmospheric pressure.

### 2.1.4 Radiative transfer model evaluation

To evaluate SCIATRAN's simulating capabilities, the simulated  $L_{\text{TOA}}$  was compared against MERIS  $L_{\text{TOA}}$  from Level 1b data (Reduced Resolution, 1.2-km resolution). The MERIS imaging geometry information (solar zenith angle, satellite viewing angle and azimuth angle) was extracted using the SNAP software for the specific day and location of the stations and then was implemented in the RTM. Simulated hyperspectral  $L_{\text{TOA}}$  were convolved with the MERIS spectral response functions to compute band-weighted average radiance values for each nominal band center ( $j$ ):

$$L_{\text{TOA}}(\lambda_j) = \sum_{i=1}^n L_{\text{TOA}}(\lambda_i) RSR(\lambda_i) \quad (2.1)$$

where  $RSR$  is the MERIS relative spectral response function.

Simulated  $L_{\text{TOA}}$  and MERIS  $L_{\text{TOA}}$  were compared using the metrics described in section 2.1.2. Match-ups were extracted using SNAP software and were considered valid if MERIS  $L_{\text{TOA}}$  data were not flagged (cosmetic, duplicated, glint risk, suspect, bright and invalid) and satellite - *in situ* measurements were taken maximum 5 hours apart. This first quality control reduced the initial number of match-ups from 20 to six data points. A visual inspection of the images identified two other stations cloud covered further reducing the number of valid match-ups to four data points. In addition, because the water constituents influence the shape and magnitude of the  $L_{\text{W}}$ , the RTM SCIATRAN was also be evaluated by investigating the spectral distribution of the  $L_{\text{W}}$  at the four selected stations for simulations (Figure 2.1, stations circled in red). Note that the stations used for the simulations were not necessarily the same with the stations where good match-ups with MERIS  $L_{\text{TOA}}$  were obtained (Fig. 2.1, black stars).

### 2.1.5 Radiative heating simulations

As input parameters in the simulations, I used *in situ* profiles of CDOM absorption spectra, Chla, TSM, temperature, and salinity. To demonstrate the heating effect of large concentrations of the water constituents CDOM and TSM, simulations were performed for four stations of the TRANSDRIFT-XVII expedition (Figure 2.1, stations circled in black and blue, Table 2.1). The simulated stations were selected because

they presented the highest and lowest values of  $a_{\text{CDOM}}(443)$  among all sampled stations with changing TSM and Chla concentrations (Table 2.1).

TABLE 2.1: CDOM absorption ( $a_{\text{CDOM}}$  in  $\text{m}^{-1}$ ), Chla ( $\text{mg}/\text{m}^3$ ), TSM ( $\text{g}/\text{m}^3$ ) at two meters depth (except for  $a_{\text{CDOM}}$  at station 40, S40, sampled at 5 m) and wind speed ( $U$  in  $\text{m}/\text{s}$ ).

Station	Date	Longitude	Latitude	Bottom Depth	Temperature	Salinity	$a_{\text{CDOM}}(443)$	TSM	Chla	$U$
S01	09.09.10	131.00	71.5	14	7.66	7.80	1.77	1.60	2.03	4.5
S03	09.09.10	131.00	72.47	18	7.77	7.02	1.67	0.40	1.95	3.9
S16	13.09.10	123.99	74.33	17	4.10	19.05	1.08	7.20	0.84	9.1
S40	19.09.10	116.69	76.84	42	-0.19	28.04	0.20	0.17	0.40	3.4

To assess only the effect of the water constituents on the radiative heating, I simulated the spectrally integrated downwelling ( $E_d$ ,  $\text{W}/\text{m}^2$ ) and upwelling irradiances ( $E_u$ ,  $\text{W}/\text{m}^2$ ) at a depth  $z$ , for July 1 at  $76^\circ\text{N}$ ,  $126^\circ\text{E}$ , and for 24 solar zenith angles (representing hourly resolution) from 300 to 800 nm. All metrics refer to an integral over one day except for the sea ice melt rate.

The net irradiance ( $E_n$ ,  $\text{W}/\text{m}^2$ ) was determined as:

$$E_n(z) = E_d(z) - E_u(z) \quad (2.2)$$

From the net irradiance summed over the course of a day I estimated the absorbed energy at every vertical layer in the water ( $E_{\text{nabs}}$ ,  $\text{KJ}/\text{m}^3$ ), based on the provided depth grid  $dz$ , as:

$$E_{\text{nabs}}(dz_i) = (E_n(z_{i+1}) - E_n(z_i))/dz_i \quad (2.3)$$

with  $i$  ranging from zero to the maximum depth ( $z$ ).

Simulations were performed for different scenarios, including and excluding absorbers. The difference in the net absorbed energy ( $\Delta E_{\text{nabs}}$ ) was determined for example, by calculating the difference between ( $E_{\text{nabs}}$ ) at S01 (highest  $a_{\text{CDOM}}$ ) and at S40 (lowest  $a_{\text{CDOM}}$ ).



The difference in the absorbed energy ( $\Delta E_{nabs}$ ) for the upper 2 m can be translated in terms of radiative heating (RH,  $^{\circ}C$ ) as:

$$\Delta RH = \frac{\Delta E_{nabs}}{\rho_s V c_p} \quad (2.4)$$

where  $\rho$  is the density of seawater measured *in situ* ( $kg/m^3$ ),  $V$  is the volume of water (i.e.  $2 m^3$ ), and  $c_p$  is the seawater specific heat ( $4100 J/kg K$ ).

Following the method described by Hill (2008), I estimated the potential increase in the rate of sea ice melt ( $\Delta(dH/dT)$ , mm/h) caused by the presence of CDOM and TSM (considering that all  $E_{oabs}$  is converted to ice melt):

$$\frac{dH}{dT} = \frac{\Delta E_{nabs}}{\rho L} \quad (2.5)$$

where  $\Delta E_{nabs}$  ( $KJ/m^2$ ) is the difference in absorbed energy due to  $a_{CDOM}$  and TSM estimated from our simulations (as in equation 2.3 but given per hour),  $\rho$  is the density of sea ice ( $900 kg/m^3$ ) and  $L$  is the latent heat of fusion of sea ice ( $300 KJ/kg$ ).

I further investigated the feedback resulting from changes in CDOM and TSM to the surface heat flux across the ocean-atmosphere interface. The difference in the summed heat flux ( $\Delta Q_{sum}$ ) was determined as the sum of the differences in the sensible heat flux ( $Q_{sen}$ ), the latent heat flux ( $Q_{lat}$ ), and the longwave radiation ( $Q_{lw}$ ). Assuming that the atmosphere does not change,  $\Delta Q_{sen}$  and  $\Delta Q_{lat}$  were determined as:

$$\Delta Q_{sen} = \rho_a c_{pa} c_H U_{10} (-T_{with} + T_{without}) \quad (2.6)$$

$$\Delta Q_{lat} = \rho_a L_v c_E U_{10} (-q_{with} + q_{without}) \quad (2.7)$$

where  $\rho_a$  denotes the air density ( $1.22 kg/m^3$ ),  $c_{pa}$  is the specific heat of air at constant pressure ( $1003 J/kgK$ ),  $c_H$  and  $c_E$  are bulk transfer coefficients ( $9.7 \times 10^{-4}$  and  $1.5 \times 10^{-3}$ , respectively and both unitless),  $U_{10}$  is the wind speed at 10 m height (m/s) derived from MERIS.  $T_{with}$  is the *in situ* surface water temperature, which includes the influence of the water constituents, and  $T_{without}$  is the *in situ* surface water temperature minus  $\Delta RH$  (both in  $^{\circ}K$ ).  $L_v$  is the latent heat of evaporation of water ( $2.45 \times 10^6 J/kg$ ),  $q_{with}$  and  $q_{without}$  are the air specific humidities (both unitless) respectively. The specific humidities were calculated with the COARE-Met Flux Algorithm

([https://coaps.fsu.edu/COARE/flux\\_algor/](https://coaps.fsu.edu/COARE/flux_algor/)) using MERIS wind speed (average value of wind speed at selected stations), the respective sea surface temperature and atmospheric pressure (1012.5 mbar).

The  $Q_{lw}$  was determined based on the longwave SCIATRAN simulations from 800 to 1190 nm. In the computation of heat flux components I considered the upper 1 m of the water column.

### 2.1.6 Spatial distribution of heating

The spatial analysis of radiative heating was simulated with satellite information of Chla,  $a_{CDOM}(443)$ , TSM and SST for August 4, 2010; the least cloudy satellite image. More specifically, the C2RCC Laptev Sea Chla and C2RCC  $a_{CDOM}(443)$  MERIS products were used after the evaluation of the satellite retrievals (Section 3.1 in Soppa et al. (2019)). CDOM absorption spectra were derived from the  $a_{CDOM}(443)$  product using a spectral slope value of 0.018 (Matsuoka et al., 2014). The TSM product was derived from the C2RCC algorithm.

Temperature was estimated from SST using the Group for High Resolution Sea Surface Temperature (GHRSSST) Multi-scale Ultra-high Resolution (MUR) SST data (Naval Oceanographic Office, 2018) that combines information from microwave and infrared sensors and represents the temperature at 1 m depth. Salinity (S) was estimated empirically from the satellite retrieved  $a_{CDOM}(443)$  using a linear relationship derived from *in situ* measurements TRANSDRIFT XXVII and assuming  $a_{CDOM}(440) \approx a_{CDOM}(443)$ :

$$S = -9.95148a_{CDOM440} + 32.49 \quad (2.8)$$

Considering the lack of vertically resolved information from remote sensing, and that the shelf areas of the Laptev Sea are very shallow (Figure 2.1), homogeneous profiles of temperature and salinity were assumed. The vertical homogeneity in the upper 10 m can be also seen in the *in situ* profiles from the TRANSDRIFT XXVII expedition. To properly model the coupled atmosphere-ocean radiative transfer it is necessary to choose a water depth deeper than the penetration depth of photons in the ocean. Here I assumed a constant bottom depth of 10 m because at all the simulated stations the radiation was absorbed within the upper 5 m of the water column. Moreover, by choosing a shallower depth than the actual water depth I was able to

significantly speed up the computation. Constant light conditions were selected during the simulations representing August 4, 2010, using an average solar zenith angle for the day at  $74^\circ N$  and  $140^\circ N$ . Because the mean value of the first attenuation depth was 2.6 m, the vertical distribution of  $Chla$ ,  $a_{CDOM}(443)$  and TSM were set homogeneous.

To investigate the increase in the RH due to the water constituents, I estimated the  $\Delta E_{nabs}$  by subtracting the minimum  $E_{nabs}$  observed in the region, representing the clearest water, from the  $E_{nabs}$  of each pixel. As a second step, I calculated  $\Delta RH$  as in Equation 2.4, using a constant  $\rho_s$  value of  $1014 \text{ kg/m}^3$ . The spatial distribution of  $\Delta RH$  was computed as described in Section 2.1.5 for the *in situ* station simulations and assuming constant wind speed of 5 m/s, so that  $\Delta RH$  would only respond to changes in SST due to the bio-optical effect of the water constituents.

## 2.2 Coupled ocean-biogeochemical model simulations

### 2.2.1 The MIT general circulation model

For the purpose of the coupled ocean-biogeochemical simulations, I used a model configuration of the Massachusetts Institute of Technology general circulation model (MITgcm, Marshall et al., 1997) based on a cubed-sphere grid (Menemenlis et al., 2008). Each face of the cube consists of 510 by 510 grid cells allowing a mean horizontal grid spacing of 18 km. Vertically, there are 50 layers with thicknesses between 10 m near the surface (upper 100 m) to 450 m at the maximum model depth of 6150 m. As described in Losch et al. (2010), bathymetry comes from (Smith and Sandwell, 1997) and from the General Bathymetric Charts of the Oceans (GEBCO) one arcminute bathymetric grid. Here, the non-linear equation of state of Jackett and McDougall (1995), written in terms of potential temperature, is used. Regarding advection, a 7th-order monotonicity-preserving scheme (Daru and Tenaud, 2004) is used. In the current setup, there is no explicit horizontal diffusivity, while horizontal viscosity follows Leith (1996). Finally, the time-mean river run-off from Large and Nurser (2001) is applied globally. In the Arctic Ocean, monthly mean climatological forcing for the river run-off, based on the Arctic Runoff Data Base (ARDB), is specified. The run-off

fields, which initially have  $1^\circ$  resolution, are interpolated bilinearly to the model grid.

Three different parameterizations for light penetration with depth were deployed. The first used constant attenuation coefficients for longwave (IR) and shortwave (VIS) radiation following Paulson and Simpson (1977) (Eq. 2.9a). This is the default parameterization in the MITgcm and was used for the control experiment (CTRL). The second one (GREEN) accounted for the self-shading effect of phytoplankton (Eq. 2.9b and 2.9c), and the third (YELLOW) additionally took into account the light absorption by CDOM (Eq. 2.9b and 2.9d). The corresponding vertical profiles of chlorophyll-a ([Chl]) and CDOM ([CDOM]) were computed by the Darwin model. A limitation, however, is the lack of a parameterization for the riverine CDOM. The equations can be written as:

$$I_{(z)} = I_{\text{IR}} \cdot e^{-k_{\text{IR}} z} + I_{\text{VIS}} \cdot e^{-k_{\text{VIS}} z} \quad (2.9a)$$

$$I_{\text{pen}}(z) = 0.4 \cdot I \cdot e^{-k_{\text{pen}}(z) z} \quad (2.9b)$$

$$k_{\text{pen}}(z) = k_w + k_c \cdot [\text{Chl}](z) \text{ or} \quad (2.9c)$$

$$k_{\text{pen}}(z) = k_w + k_c \cdot [\text{Chl}](z) + k_{\text{CDOM}} \cdot [\text{CDOM}](z) \quad (2.9d)$$

where the diffuse attenuation coefficients ( $k_{\text{IR}}$ ,  $k_{\text{VIS}}$ ) and the light partitioning correspond to Jerlov water type I (Jerlov, 1976). To be consistent with the control run, I accounted for the longwave radiation to be fully attenuated in the first vertical layer and the penetrative part ( $I_{\text{pen}}$ ) to be 40% of the total flux ( $I$ ) (Eq. 1b).  $k_w$  ( $0.04 \text{ m}^{-1}$ ) is the spectrally averaged attenuation coefficient for pure seawater, while  $k_c$  ( $0.04 \text{ (mmol chl/m}^3\text{)}^{-1}$ ) and  $k_{\text{CDOM}}$  ( $10 \text{ m}^2\text{/mmol P}$ ) are for chlorophyll and CDOM. The  $k_{\text{CDOM}}$  coefficient was calculated given specific CDOM absorption spectra as described in Dutkiewicz et al. (2015).

The available light depends on the present sea ice conditions:

$$Q_{sw_{net}} = Q_{sw_{water}}(1 - c) + Q_{sw_{ice}}c \quad (2.10)$$

$$Q_{sw_{ice}} = f_{ice}Q_{sw}(1 - \alpha_{ice})e^{-1.5h_{ice}} \quad (2.11)$$

where  $c$  is the fractional sea ice cover,  $h_{ice}$  is the ice thickness,  $f_{ice}$  is the ice short-wave radiation penetration factor (0.3), and  $\alpha_{ice}$  is the sea ice albedo.  $Q_{sw}$  denotes the incoming shortwave radiation,  $Q_{sw_{net}}$  is the net downward shortwave heat flux as a result of water and ice fractions ( $Q_{sw_{water}}$  and  $Q_{sw_{ice}}$ , respectively). It should be noted, however, that the light does not penetrate the sea ice if it is covered by snow.

As initial conditions for the MITgcm, I use the model state described in Losch et al. (2010). Their simulation was initialized in January 1979, with temperature and salinity fields obtained from the Polar Science Center Hydrographic Climatology (PHC) 3.0 (Steele, Morley, and Ermold, 2001). The Darwin model initialized on 1 January 2000 by a state obtained from the model setup described in Losa et al. (2019). The period from 2000 to 2006 is assumed to be sufficiently long to get the upper ocean biogeochemistry in a quasi-steady state (Clayton et al., 2017). The analysis focuses on 10-day averages over 2007-2016, a period including the three years characterized by the most ice-free conditions during the Arctic summer (2007, 2012, 2016). Therefore, a special emphasis is given to 2012, which was the year with the summer sea ice extent minimum record (Parkinson and Comiso, 2013), and 2016, which was characterized by a record-late freeze-up in the central Arctic (Petty et al., 2018).

### 2.2.2 The JRA-55 atmospheric reanalysis

The MITgcm is forced by 3-hourly atmospheric conditions from the Japanese 55-year reanalysis (JRA-55, Kobayashi et al., 2015) over the period of 1992 - 2019. The JRA-55 uses a 4Dvar data assimilation scheme, and the provided fields have an average spatial resolution of  $0.56^\circ$ . Surface winds, temperature, humidity, downward shortwave and longwave radiation, as well as precipitation, are converted to heat, freshwater,

and wind stress fluxes using the (Large and Yeager, 2004) bulk formulae. In order to transfer the JRA-55 fields from source to the model grid, bilinear interpolation is applied to the buoyancy forcing terms, and bicubic interpolation to the wind velocity components.

### 2.2.3 Heat budget equation

The equation of heat conservation in the re-scaled height coordinate system ( $z^*$ ), can be written as:

$$\frac{\partial(s^*\theta)}{\partial t} = -\nabla_{z^*}(s^*\theta\mathbf{V}) - \frac{\partial(\theta w)}{\partial z^*} + s^*F_\theta + s^*D_\theta \quad (2.12)$$

where  $\theta$  is potential temperature,  $\mathbf{V} = (u, v)$  and  $w$  are the total horizontal and vertical velocities, respectively.  $F_\theta$  is the total local forcing accounting for shortwave heating and surface heat exchanges (Section 2.2.4, Eq. 2.15 - 2.20).  $D_\theta$  is the term accounting for the diffusive mixing processes according to the KPP scheme, described in Section 2.2.5 (Eq. 2.21).

The  $z^*$  coordinate is defined as:

$$z^* = \frac{z - n(x, y, t)}{H(x, y) + n(x, y, t)}H(x, y) \quad (2.13)$$

where  $H$  is the ocean depth,  $n$  is the sea surface height, and  $z$  is the unscaled vertical coordinate that ranges from  $-H$  to 0.  $s^*$  is a scale factor:

$$s^* = 1 + n/H \quad (2.14)$$

$\nabla_{z^*}$  and  $\partial/\partial z^*$  are the horizontal and vertical divergences, respectively, in the frame of the  $z^*$  system.

### 2.2.4 Surface heat flux components

The air-sea heat flux  $Q$  is computed by summing estimates of its components:

$$Q = Q_{SW} + Q_{LW} + Q_{sen} + Q_{lat} \quad (2.15)$$

The net shortwave radiation flux ( $Q_{SW}$ ) is the net difference between the downwelling ( $SW \downarrow$ ) and the upwelling ( $SW \uparrow$ ) shortwave radiation:

$$Q_{SW} = SW \downarrow - SW \uparrow \quad (2.16)$$

Likewise, the net longwave radiation ( $Q_{LW}$ ) is the net difference between the downwelling infrared (IR) radiation ( $LW \downarrow$ ) and the upwelling ( $LW \uparrow$ ), which comprises the IR radiation emitted by the ocean and the portion of downwelling IR radiation that is reflected.  $Q_{LW}$  can be expressed as:

$$Q_{LW} = LW \downarrow - LW \uparrow \quad (2.17)$$

The heat flux associated with the upwelling longwave radiation emitted the ocean, is given by:

$$LW \uparrow_{ocean} = -\sigma\epsilon(SST)^4 \quad (2.18)$$

where  $\sigma$  is the Stefan-Boltzmann constant and  $\epsilon$  is the surface emissivity.

The turbulent fluxes are estimated from bulk formulae (Large and Yeager, 2004). The flux of sensible heat ( $Q_{sen}$ ) is a function of the temperature difference between the ocean and the atmosphere:

$$Q_{sen} = \rho_\alpha C_{Pair} C_H U \Delta\theta \quad (2.19)$$

where  $\rho_\alpha$  the atmospheric air density at the surface,  $C_{Pair}$  is the specific heat of air (1004 J/kg/K),  $C_H$  is the dimensionless transfer coefficient for sensible heat,  $U$  is the magnitude of the wind at the surface, and  $\Delta\theta$  is the air-sea difference in potential temperature.

Similarly, the turbulent flux of latent heat ( $Q_{lat}$ ) is directly related to the evaporative component of the freshwater flux ( $E$ ):

$$Q_{lat} = L_v E = L_v \rho_\alpha C_E U (q_{air} - q_{sat}) \quad (2.20)$$

where  $L_v$  is the latent heat of evaporation,  $C_E$  is the transfer coefficient for evaporation,  $q_{air}$  is the near-surface air specific humidity, and  $q_{sat}$  is the specific humidity of saturated air.

### 2.2.5 Vertical mixing parameterization (KPP)

For the parameterization of vertical mixing in MITgcm, the so-called KPP scheme by Large, McWilliams, and Doney (1994) is used. Following Losch et al. (2010), a meridionally and vertically varying background vertical diffusivity is considered. The vertical diffusivity at the surface is  $4.4 \times 10^{-6} \text{ m}^2 \text{ s}^{-1}$  at the Equator,  $3.6 \times 10^{-6} \text{ m}^2 \text{ s}^{-1}$  north of  $70^\circ\text{N}$ , and  $1.9 \times 10^{-5} \text{ m}^2 \text{ s}^{-1}$  south of  $30^\circ\text{S}$  and between  $30^\circ\text{N}$  and  $60^\circ\text{N}$ . On the vertical, diffusivity increases to  $1.1 \times 10^{-4} \text{ m}^2 \text{ s}^{-1}$  at the maximum depth of 6150 m.

The KPP scheme treats a variety of unresolved processes involved in vertical mixing, such as shear instability, and internal wave activity. At every model's grid cell, the scheme determines a boundary layer depth ( $h$ ) based on a bulk Richardson number critical value. Below the boundary layer ( $z < h$ ), the fluxes are only local. Within  $h$ , mixing is enhanced by the stabilizing or destabilizing effect of surface forcing, namely buoyancy and momentum. That boosts the penetration of the properties of the boundary layer into the thermocline.

The vertical flux  $\overline{w\theta}$  of potential temperature  $\theta$  (or momentum) within the scheme is composed of a gradient-flux term (proportional to the property's vertical divergence  $\partial_z^* \theta$ ), and a non-local term  $\hat{\gamma}_\theta$  that enhances the gradient-flux mixing:

$$\overline{w\theta} = -K_\theta \left( \frac{\partial \theta}{\partial z^*} - \hat{\gamma}_\theta \right) \quad (2.21)$$

where  $K_\theta$  is the eddy diffusivity. The non-local term  $\hat{\gamma}$  does not depend on the vertical gradient of temperature and it further enhances mixing when the water column



is unstable. Apparently,  $\hat{\gamma}$  represents eddies with scales that are comparable to the variation of the background gradient of temperature ( $\partial\theta/\partial z$ ).

For the purposes of this thesis, the following parts in the KPP scheme within MITgcm have been modified. To compute the fraction of solar shortwave flux penetrating to the bottom of the mixing layer ( $KPPfrac$ ), the effect of chlorophyll-a and CDOM is taken into account:

$$KPPfrac(z) = 0.4e^{-k_{pen}(z)} \quad (2.22)$$

where  $k_{pen}$  is calculated from the Equation 2.9c for GREEN, and the Equation 2.9d for the YELLOW simulation. Similarly, the buoyancy forcing ( $bfc$ ) is defined as:

$$bfc(z) = bo_{surf} + bosol(z)(1 - 0.4e^{-k_{pen}(z)}) \quad (2.23)$$

where  $bo_{surf}$  is the surface turbulent buoyancy forcing ( $m^2/s^3$ ), and  $bosol$  is the surface radiative buoyancy forcing ( $m^2/s^3$ ).

### 2.2.6 The Darwin biogeochemical model

A version of the Darwin ocean biogeochemical model (based on Dutkiewicz et al. (2015) and adapted according to Losa et al. (2019)) coupled to the MITgcm is used to simulate the dynamics of CDOM, as well as of two zooplankton and six phytoplankton functional types (PFTs). These PFTs can be seen as analogues of small and large diatoms, other large non-silicified eukaryotes (represented by *Phaeocystis*), *Prochlorococcus*-like picophytoplankton, nitrogen fixers, and coccolithophores. The model configuration uses 42 tracers in total to describe the cycling of carbon (C), phosphorus (P), nitrogen (N), silicon (Si), iron (Fe), and oxygen (O) through inorganic, living, dissolved, and particulate phases.

As described in Losa et al. (2019), two distinct size classes have been introduced for diatoms. The first class corresponds to small diatoms, which are slightly silicified and can grow fast at lower latitudes. The second one represents large diatoms that are strongly silicified and consist of slowly growing cells at high latitudes (Quéguiner,

2013). Furthermore, a coccolithophore physiology with high affinity for nutrients (Paasche, 2001), and ability to escape grazing control, has been considered (Losa et al., 2006). Although nitrogen fixers and *Prochlorococcus*-like prokaryotes are of minor importance in the northern hemisphere’s high latitudes, they help maintaining a reasonably good performance of the model globally (Losa et al., 2019). Table 2.2 illustrates some of the most important traits of the PFTs included in the current setup.

TABLE 2.2: Biogeochemical model internal parameters and traits, where *Phaeo* refers to *Phaeocystis*, *Prochlor* to *Prochlorococcus*, N-fixers to nitrogen fixing phytoplankton and *cocco* to coccolithophores. (Table adapted from Losa et al., 2019)

Param	Units	large diatoms	<i>Phaeo</i>	small diatoms	<i>Prochlor</i>	N-fixers	<i>cocco</i>
$P_{max}^C$	day <sup>-1</sup>	1.79	1.59	2.16	1.09	0.31	1.23
$\beta$	-				1.25		
$r_{j,k=1}$	-	0.8	0.78	0.2	0.2	0.6	0.58
$r_{j,k=2}$	-	0.16	0.156	1.0	1.0	0.12	0.12
$w_{sink}$	m day <sup>-1</sup>	0.77	0.23	0.10	0.03	0	0.23
$\phi_{max_j}$	mmolC (mol photons) <sup>-1</sup>	40	40	40	40	40	40
$\overline{a_j^*}$	m <sup>2</sup> mgChla <sup>-1</sup>	0.02	0.02	0.02	0.02	0.02	0.02
$m_{pj}$	day <sup>-1</sup>	0.04	0.05	0.1	0.1	0.1	0.05
$mfunc$	-	silicified		silicified			calcifier

$P_{max}^C$  is the maximum photosynthetic rate at 30°C;  $\beta$  is the photoinhibition parameter, applied to *Prochlorococcus*;  $k_{sat}$  is the growth half-saturation constant;  $r_{j,k}$  denotes the palatability factor of the particular PFT ( $j = 1, 2, \dots, 6$ ), grazing of phytoplankton for small or micro-zooplanktons ( $k = 1, 2$ );  $w_{sink}$  is the sinking rate;  $\phi_{max_j}$  is the maximum quantum yield of carbon fixation;  $\overline{a_j^*}$  is the spectrally averaged phytoplankton-specific light absorption;  $m_{pj}$  is the mortality rate; finally,  $mfunc$  determines the biomineralizing function.

## 2.2.7 Phenological indices

The phenology of diatoms (small and large) and haptophytes (*Phaeocystis* and coccolithophores) was examined by calculating phenological indices, as described in Soppa, Völker, and Bracher (2016), based on a threshold method for total chlorophyll-a (Tchl-a) proposed by Siegel, Doney, and Yoder (2002). More specifically, the bloom start and end date were taken into account. These indices were calculated over the year 2012 for the partial diatoms chlorophyll-a but also for haptophytes. This time period

covers the summer sea ice extent minimum record (Parkinson and Comiso, 2013), and the months after this event.

### 2.2.8 Phytoplankton growth limiting factors

The spatial distribution of the limiting factors for large diatoms, coccolithophores, and *Phaeocystis*, in the upper 30 m during the growing season (April–September), have been calculated. To plot the limiting factors distribution I follow Schneider et al. (2008), where the nutrient with the lowest Michaelis–Menten coefficient, in a given location is seen as limiting.

The limitations by  $\text{PO}_4$  and Si (in  $\text{mmol P m}^{-3}$  and  $\text{mmol Si m}^{-3}$ ) are parameterized following the Michaelis–Menten formulation:

$$N_{\text{lim}_i} = \frac{N_i}{N_i + k_{\text{sat}_{ji}}} \quad (2.24)$$

where  $k_{\text{sat}_{ji}}$  is the half-saturation constant of nutrient  $i$ , for phytoplankton  $j$  (Table 2.3). Following Dutkiewicz et al. (2015), Nitrogen is available in three forms: nitrate ( $\text{NO}_3$ ), nitrite ( $\text{NO}_2$ ), and ammonia ( $\text{NH}_4$ ):

$$N_{\text{Nlim}_j} = \frac{\text{NO}_3 + \text{NO}_2}{\text{NO}_3 + \text{NO}_2 + k_{\text{IN}_j}} e^{-\Psi_{\text{NH}_4}} + \frac{\text{NH}_4}{\text{NH}_4 + k_{\text{NH}_4j}} \quad (2.25)$$

where  $k_{\text{IN}_j}$  is the half-saturation constant of  $\text{IN} = \text{NO}_3 + \text{NO}_2$ ,  $k_{\text{NH}_4j}$  is the half-saturation constant of  $\text{NH}_4$ , and reflects the fixed nitrogen uptake inhibition by ammonia. Light and temperature are limiting when the Michaelis–Menten coefficients are above 0.7.

### 2.2.9 Model evaluation

The simulated sea ice is evaluated given sea ice concentration and sea ice extent data from the NOAA/NSIDC Climate Data Record of Passive Microwave sea ice Concentration, Version 3 (Peng et al., 2013): <https://nsidc.org/data/G02135/versions/3>.

TABLE 2.3: Biogeochemical model parameters of the nutrient-specific limitation for large and small diatoms, *Phaeocystis* (*Phaeo*), *Prochlorococcus* (*Prochlor*), nitrogen fixing phytoplankton (N-fixers), and for coccolithophores (*cocco*).

Parameter	large diatoms	<i>Phaeo</i>	small diatoms	<i>Prochlor</i>	N-fixers	<i>cocco</i>
$k_{sat_N}$ ( $mmol\ N\ m^{-3}$ )	0.451	0.106	0.053	0.007	-	0.086
$k_{sat_P}$ ( $mmol\ P\ m^{-3}$ )	0.028	0.007	0.003	0.0004	0.004	0.0054
$k_{sat_{Si}}$ ( $mmol\ Si\ m^{-3}$ )	0.450	-	0.06	-	-	-
$k_{NH_4_j}$ ( $mmol\ N\ m^{-3}$ )	0.225	0.053	0.0265	0.0035	-	0.043

For the evaluation of the simulated nutrients by the current Darwin-MITgcm setup, data from the World Ocean Atlas 2018 (WOA, Garcia et al., 2018) is used. WOA provides a set of global climatological fields at 102 standard depth levels, and for inorganic nutrients, it comes with  $1^\circ$  horizontal resolution. However, in many parts of the Arctic Ocean the measurements are very sparse, compared to other areas of the global ocean, both spatially and temporally. Furthermore, WOA observations cover the 1955-2010 period that is almost out of range of the simulated period here. Due to computational and storage limitations, the 2012-2014 simulated period is considered for the comparison against WOA. This time span includes the year 2012 that most of the analysis in Chapters 4 and 5 is focused on, as well as the two following years which are typical (physically and biogeochemically) of the entire simulated period.

The simulated surface chlorophyll-a concentrations and CDOM absorption are compared against satellite remote sensing measurements. More specifically, surface chlorophyll-a concentrations (Gohin, Druon, and Lampert, 2002) from the merged GlobColour product (<ftp://ftp.hermes.acri.fr/GLOB/merged/>) are used. Additionally, the observed surface absorption of colored dissolved and detrital matter (CDM) at 443 nm (Werdell et al., 2013) from the NASA GSF Center, is used: (<https://oceandata.sci.gsfc.nasa.gov/MODIS-Aqua/Mapped/Monthly>). Although CDM accounts for the absorption from both detritus and dissolved material, it is the most suitable remote sensing product to compare against simulated CDOM.

## Chapter 3

# Assessing the influence of water constituents on the radiative heating of Laptev Sea shelf waters

### 3.1 Introduction

The Laptev Sea in the Arctic Ocean is a vast Siberian shelf region that is highly influenced by the Lena River. Apart from being one of the largest rivers on Earth, the Lena River comprises the largest delta in the Arctic (Heim et al., 2014) and yields the highest annual flux of DOM to the Arctic Ocean (Stedmon et al., 2011; Holmes et al., 2012). The river peak discharge takes place in June and contributes heat and freshwater to the shallow Laptev Sea shelf. At the same time, it increases the sea ice melt rate and sets up the summer stratification (Janout et al., 2016). Here, I examine the potential of high concentrations of CDOM and suspended material in enhancing near-surface solar energy absorption, and hence, sea ice melt rates in the region.

With the synergy of satellite remote sensing, radiative transfer modelling (RTM), and *in situ* observations, I simulate the radiative heating in the surface and sub-surface shelf waters of the Laptev Sea. More specifically, I employ a coupled ocean-atmosphere radiative transfer model (RTM) and simulate the in-water radiative heating based on measurements of CDOM spectral absorption ( $a_{\text{CDOM}}$ ,  $\text{m}^{-1}$ ), TSM ( $\text{g}/\text{m}^3$ ) and chlorophyll-a concentration (Chla,  $\text{mg}/\text{m}^3$ ) from the TRANSDRIFT XVII expedition carried out in September 2010. Additionally, the potential of using ocean colour satellite retrievals in the RTM to investigate the spatial variability of radiative heating is shown.

### ***Contributions:***

Most of this chapter's results have been published in *Frontiers in Marine Science* (Soppa et al., 2019). Dr. Mariana Soppa, firstly validated the MERIS chlorophyll-a, TSM, and  $a_{CDOM}(443)$  retrievals from C2RCC and C2X algorithms (Section 2.1.2) against *in situ* measurements to determine the best products for later use in the radiative transfer simulations. For more information on the validation of the ocean colour algorithms, the reader is referred to Section 2.2 and 3.1 of Soppa et al. (2019). Then, we jointly performed the match-up analysis to evaluate the SCIATRAN simulations, by comparing simulated top-of-atmosphere radiances ( $L_{TOA}$ ) to MERIS  $L_{TOA}$  (Section 3.2.1).

As a next step, I set up the coupled radiative transfer model SCIATRAN, conducted the numerical simulations, and carried out the analysis to investigate how changes in the water constituents impact the radiative heating of Laptev Sea surface waters looking at specific TRANSDRIFT XVII stations (Section 2.1.4, data provided by Dr. Jens Hölemann). Finally, I used retrieved satellite data of  $a_{CDOM}(443)$ , TSM, Chla (data provided by Dr. Mariana Soppa), and sea surface temperature as input to the model, and I performed the simulations for quantifying the spatial distribution of radiative heating (Section 2.1.6) in the surface waters of the Laptev Sea.

*Further details on the authors' contributions to this study, can be found [here](#).*

## **3.2 Results**

### **3.2.1 Evaluation of the radiative transfer model**

The evaluation of SCIATRAN radiative transfer model shows that the radiative processes are well implemented in the model. The simulated top-of-atmosphere radiance ( $L_{TOA}$ ) is in agreement with the matched  $L_{TOA}$  from MERIS (Figures 3.1, 3.2). Statistics per band show greater uncertainties at the wavelengths closer to the ozone absorption bands (560 to 681 nm, bands 5 to 8) (Figure 3.1 and Table 3.1). Uncertainties

in the RTM may originate from the input data (e.g. imprecise characterization of the atmospheric aerosol particles) and formulation of the radiative transfer processes in the model (Blum et al., 2012). Figure 3.2 depicts the simulated SCIATRAN spectrum at S35 compared against matched MERIS-L1b  $L_{\text{TOA}}$ . The simulated  $L_{\text{TOA}}$  has very similar spectral shape and magnitude with the satellite measured one.

TABLE 3.1: Statistical results of the validation of the SCIATRAN simulated  $L_{\text{TOA}}$  against the MERIS  $L_{\text{TOA}}$  per band.

Band	Band center (nm)	r	RMSE	Bias	Slope	N
1	413	0.98	1.85	1.78	1.02	4
2	443	0.99	0.36	0.27	1.00	4
3	490	0.94	0.90	-0.71	0.90	4
4	510	0.82	1.56	-1.29	0.71	4
5	560	0.34	2.38	-1.77	0.16	4
6	620	0.38	1.53	-1.04	0.15	4
7	665	0.40	1.25	-0.86	0.13	4
8	681	0.46	1.10	-0.72	0.14	4
9	708	0.78	0.70	-0.38	0.23	4
10	753	0.99	0.65	0.24	0.19	4
11	761	0.90	1.49	-1.47	0.01	4
12	778	0.98	0.65	0.29	0.16	4
13	865	0.82	0.59	0.26	0.07	4
14	885	0.72	0.61	0.31	0.05	4
15	900	0.67	0.70	-0.51	0.02	4

Figure 3.3 presents the water-leaving radiance ( $L_{\text{W}}$ ) spectrum of stations selected for the radiative heating simulations. The magnitude and shape of  $L_{\text{W}}$  reflect the influence of the optically active water constituents. Stations with higher concentrations of constituents (continuous lines) are characterized by lower values of  $L_{\text{W}}$  in the visible part of the spectra, as well as flatter spectra than S40, with lower concentrations of absorbers (dashed line).

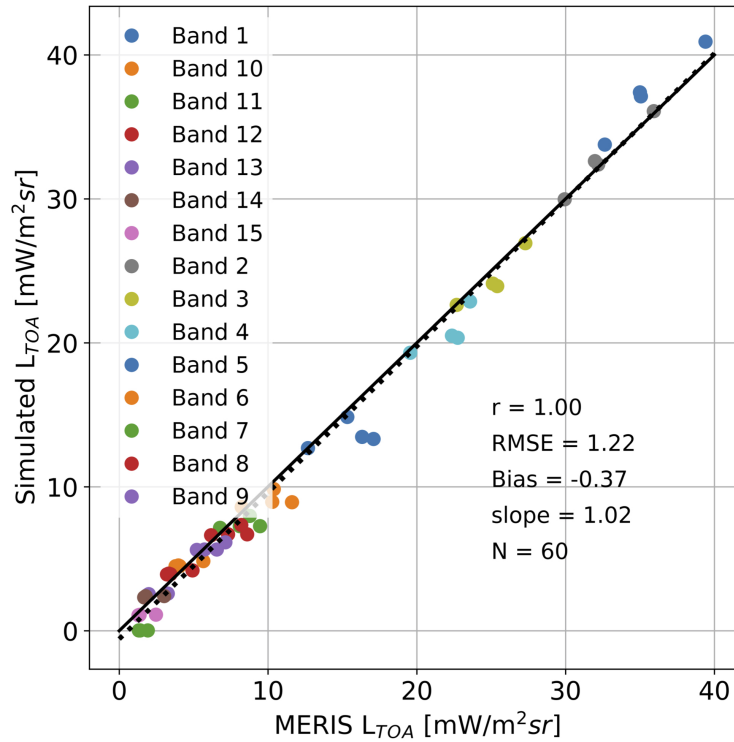


FIGURE 3.1: Scatter plot of SCIATRAN simulated  $L_{TOA}$  against MERIS  $L_{TOA}$  in the visible and near infrared spectral bands.

### 3.2.2 Bio-optical effect of CDOM and TSM on the radiative heating

Figure 3.4 shows  $a_{CDOM}$  spectra, temperature and salinity profiles of S01 (yellow), located on the inner shelf close to the main branches of the Lena River, and S40 (blue), located on the northwestern Laptev Sea shelf. The presence and concentration of CDOM and TSM are associated with the proximity to the Lena River Delta, indicating that river input and coastal erosion comprise the main sources of water constituents, as shown by several studies (e.g. Stedmon et al. (2011) and Holmes et al. (2012)). The influence of the fresh river water on S01 can be seen by the much higher  $a_{CDOM}$ , temperature and lower salinity compared to S40, which is under the influence of open ocean waters entering the central Laptev Sea (Bauch and Cherniavskaia, 2018). S01 presents  $a_{CDOM}(443)$  values almost nine times higher in comparison to S40.

It is also likely that the CDOM and TSM concentrations were higher before the TRANSDRIFT-XVII expedition. Other studies report maximum concentrations of CDOM and silica flux from the Lena River to the Arctic in spring (Stedmon et al.,



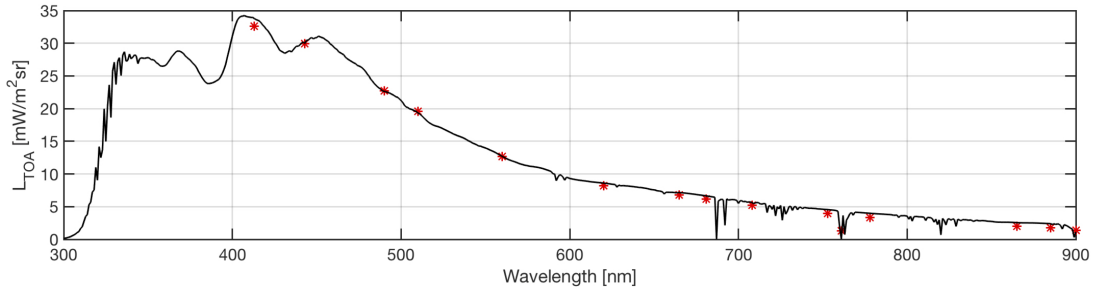


FIGURE 3.2: Comparison of SCIATRAN simulated (black) and MERIS-L1b (red) LTOA at S35.

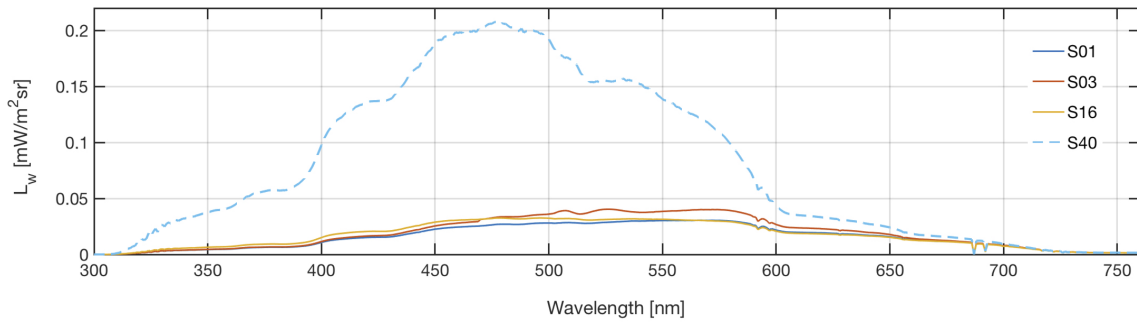


FIGURE 3.3: Simulated water-leaving radiance ( $L_W$ ) spectra of stations selected for radiative heating simulations.

2011; Holmes et al., 2012). In summer, when the TRANSDRIFT-XVII expedition took place, the loads of CDOM and TSM are generally lower and the waters over the shelf are dominated by river runoff, sea ice melt, and marine and polynya waters (Bauch and Cherniavskaia, 2018). On interannual time scales, the river water transport and ocean circulation on the Siberian shelves is controlled by two summer atmospheric regimes linked to the Arctic Oscillation (AO) (Morison et al., 2012). During a positive phase of AO, cyclonic atmospheric circulation prevails with northerly winds advecting Lena River water eastwards along the coast into the East Siberian Sea. The opposite holds true during a negative phase, as found during TRANSDRIFT-XVII, when prevailing southerly winds allow the Lena River plume to move north- and westward. Besides large-scale atmospheric circulation, regional wind patterns influence the extent of the river plume on monthly time scales (Dmitrenko et al., 2005; Janout et al., 2015).

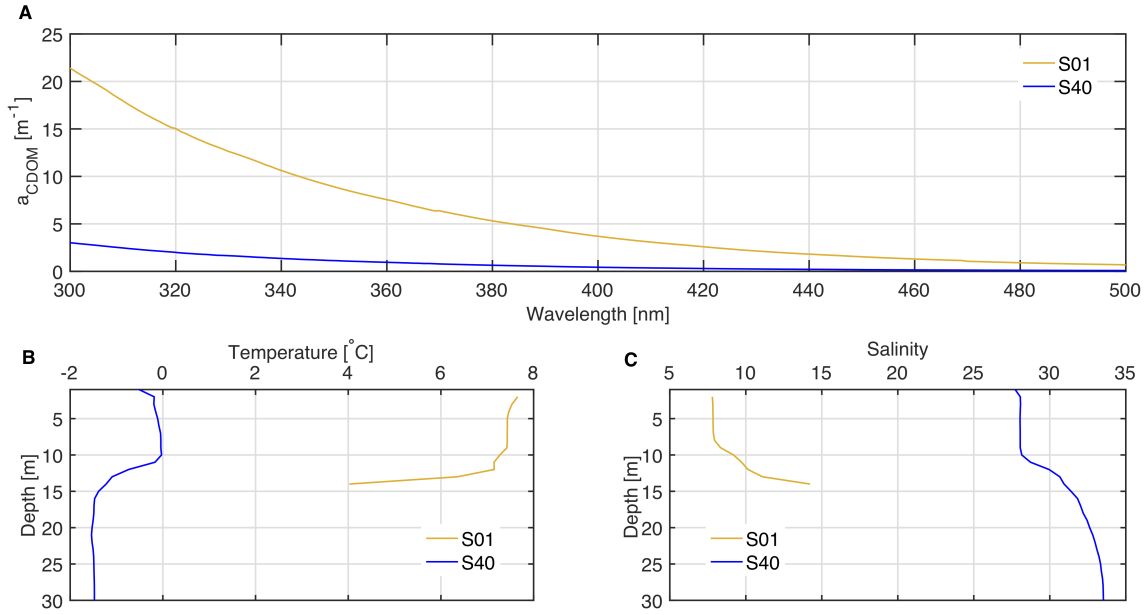


FIGURE 3.4: A) CDOM absorption spectra ( $a_{CDOM}$ ) at 5 m depth, B) temperature profiles, and C) salinity profiles of S01 (yellow) and S40 (blue), measured *in situ*.

### 3.2.3 Absorbed energy and radiative heating

Profiles of the absorbed energy per layer ( $E_{nabs}$ , Eq. 2.3) show that in high CDOM and TSM regimes, the incident solar radiation is strongly absorbed in the first meter of the water column and almost fully attenuated in the upper three meters (Figure 3.5A). A closer look at S03 (Figure 3.5B), also a high  $a_{CDOM}$  station but with lower concentrations of TSM than S01, shows a turning point at about 1.7 m; below this depth less energy is available under the presence of CDOM. A similar turning point pattern is found at S16 in the absence of CDOM and TSM, but at shallower depths (Figure 3.5C). As expected, in the marine-influenced waters of S40, where the concentration of CDOM, TSM, and Chla are low, the radiation penetrates deeper compared to the river-influenced stations and in turn, some of the heat could be trapped in or below the pycnocline.

The fate of heat trapped in the interior water column generally depends on the physical processes that dominate the ocean dynamics. For instance, (Janout et al.,

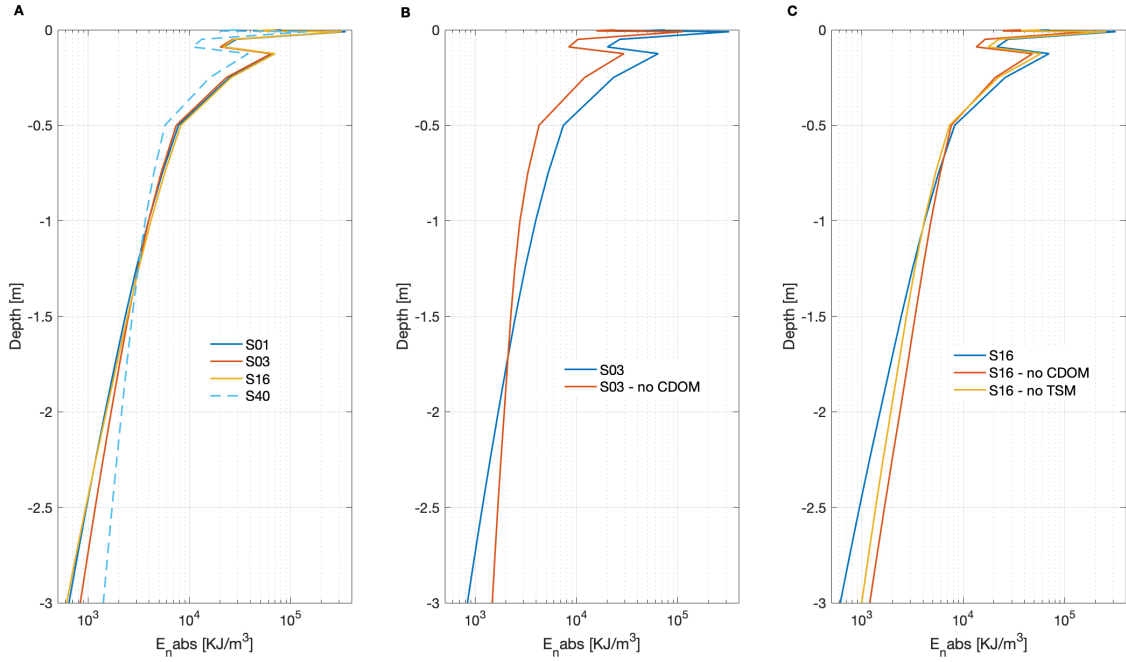


FIGURE 3.5: (A) Profiles of daily absorbed energy ( $E_{nabs}$ , normalized by  $dz$ ) including all absorbers. (B) Profiles of daily absorbed energy ( $E_{nabs}$ , normalized by  $dz$ ) at S03 including all absorbers (blue) and without CDOM (red). (C) Profiles of daily absorbed energy ( $E_{nabs}$ , normalized by  $dz$ ) at S16 including all absorbers (blue), without CDOM (red), and without TSM (orange).

2016) discussed observations of warm ( $0^{\circ}\text{C}$ ) waters near the seafloor due to downward mixing of summer-warmed near-surface waters by tidal mixing and other processes. The warm waters that are episodically observed in the interior water column by oceanographic moorings could well affect the sea ice cover if released towards the surface. However, whether warm waters are released back to the surface or they are mixed with near-freezing shelf waters at depth remains unclear. In the Canadian Basin of the Arctic Ocean, Timmermans (2015) found the presence of a near-surface temperature maximum, associated with a solar-heated water mass stored under the mixed layer. By use of high-resolution measurements, Timmermans (2015) was able to identify the upward release of heat and estimated that this process contributed to 25% of sea ice loss.

When CDOM is switched off in the simulation at S03 (other absorbers are kept), there is a decrease of  $\sim 76\%$  in the daily absorbed energy in the upper 2 m of the water column (Table 3.2).  $E_{nabs}$  at S01 (shelf region) is  $\sim 43\%$  higher relative to S40,

underlining the role of CDOM in the river influenced waters of the Laptev Sea. TSM presence also plays a notable role on how much energy is absorbed in the surface waters. However, even when considering the highest TSM value measured in the field, at S16, the concentration is not high enough to exceed the optical influence of CDOM in terms of  $E_{nabs}$  (Figure 3.5C).

The higher daily absorbed energy by CDOM and TSM increases the radiative heating (RH). There is a  $\Delta RH$  of  $\sim 0.8$  °C in the top 2 m when CDOM absorption is included in the simulations at S03, and of  $\sim 0.2$  °C when TSM is included in the simulations at S16 (Table 3.2). A comparison between S01 and S40 shows an increase in RH of approximately 0.6 °C. The  $\Delta RH$  induced by CDOM and TSM is maximum in the upper meter of the water column at S01 and S16 and for both stations less energy is deposited at greater depths.

The net surface warming and possible steeper thermoclines may have a stabilizing effect, leading to more intense stratification and to lower mixed layer depths (MLD) as the surface becomes warmer and the underneath layer colder. This effect may not be that prominent in areas very close to Lena Delta, which are directly influenced by the river outflow. However, surface heating may affect the stratification in open ocean regions of the Laptev Sea and other regions in the Arctic Ocean. Surface light attenuation induced by CDOM and TSM limits the available energy in the MLD, leading to stronger stratification and less vertical turbulent mixing, with profound importance on primary productivity, ocean circulation, air-sea interaction, and sea ice melting.

### 3.2.4 Sea ice melt and atmosphere-ocean heat flux

The potential contribution of CDOM to sea ice melting rate is approximately 0.3 mm/h at S03 (Table 3.2). In comparison,  $\Delta(dH/dt)$  (Eq. 2.5) caused by energy absorption due to TSM is lower,  $\sim 0.1$  mm/h at S16, whereas the combined effect of the water constituents leads to a  $\Delta(dH/dt)$  of  $\sim 0.4$  mm/h. In waters influenced by the Lena River plume, there is an increase of 0.2 mm/h in the ice melt rate relative to the marine-influenced waters. Given the bio-optical influence on the radiative heating in the Laptev Sea, a future with an amplified Arctic warming, and hence, increased river

runoff could have significant consequences for sea ice.

TABLE 3.2: Absorbed energy absolute difference ( $\Delta E_{\text{nabs}}$ , KJ/m<sup>2</sup>) and relative difference ( $\% \Delta E_{\text{nabs}}$ ), as well as radiative heating ( $\Delta \text{RH}$ , °C), ice melting rate ( $\Delta(\text{dH}/\text{dt})$ , mm/h), sensible ( $\Delta Q_{\text{sen}}$ , W/m<sup>2</sup>), latent ( $\Delta Q_{\text{lat}}$ , W/m<sup>2</sup>) heat flux, and net longwave radiation ( $\Delta Q_{\text{lw}}$ , W/m<sup>2</sup>) differences for the selected scenarios.

Scenarios	$\Delta E_{\text{nabs}}$	$\% \Delta E_{\text{nabs}}$	$\Delta \text{RH}$	$\Delta(\text{dH}/\text{dt})$	$\Delta Q_{\text{sen}}$	$\Delta Q_{\text{lat}}$	$\Delta Q_{\text{lw}}$
S01 - S01 no CDOM	5290	33.6%	0.64	0.23	-7.42	-11.60	0.00
S03 - S03 no CDOM	6523	75.9%	0.79	0.28	-7.14	-11.16	0.00
S16 - S16 no TSM	1575	10.9%	0.19	0.07	-4.91	-6.36	-0.85
S16 - S16 pure sea water	8959	127.4%	1.08	0.38	-21.16	-26.16	-0.85
S01 - S40	4704	42.6%	0.57	0.20	-5.87	-5.51	13.5

The bio-optical influence on the SST affects the atmosphere-ocean heat exchange as well. Considering that the *in situ* measured SST during both expeditions (Table 2.1) was influenced by water constituents, the difference between *in situ* SST and  $\Delta \text{RH}$  represents SST without the bio-optical influence. In this case, for air temperature of 6.7 °C (average air temperature for the location and time of the measurements from ERA-Interim reanalysis) at S01 and S03, SST would be warmer than the overlying atmosphere in both cases, with and without the influence of CDOM, and hence, the sensible heat would be transferred from the ocean to the atmosphere (Table 3.2). At S16 on the other hand, in all scenarios, the atmosphere is warmer than the ocean, but the presence of TSM and other optically active water constituents reduces the temperature gradient between ocean and atmosphere and also decreases the sensible heat uptake by the ocean. The effect of TSM leads to an increase of the heat flux to the atmosphere ( $\Delta Q_{\text{sum}}$ , Eq. 2.6 - 2.7) of  $\sim 12$  W/m<sup>2</sup> and, as expected, would lead to more oceanic heat uptake by  $\sim 48$  W/m<sup>2</sup> ( $\Delta Q_{\text{sum}}$ ) at S16 in comparison to the bio-optical free scenario. The small but positive value of  $\Delta Q_{\text{lw}}$  when comparing S01 and S40 is likely attributed to the influence of salinity rather CDOM and TSM in the RTM, but it needs to be further investigated.

### 3.2.5 Radiative heating distribution

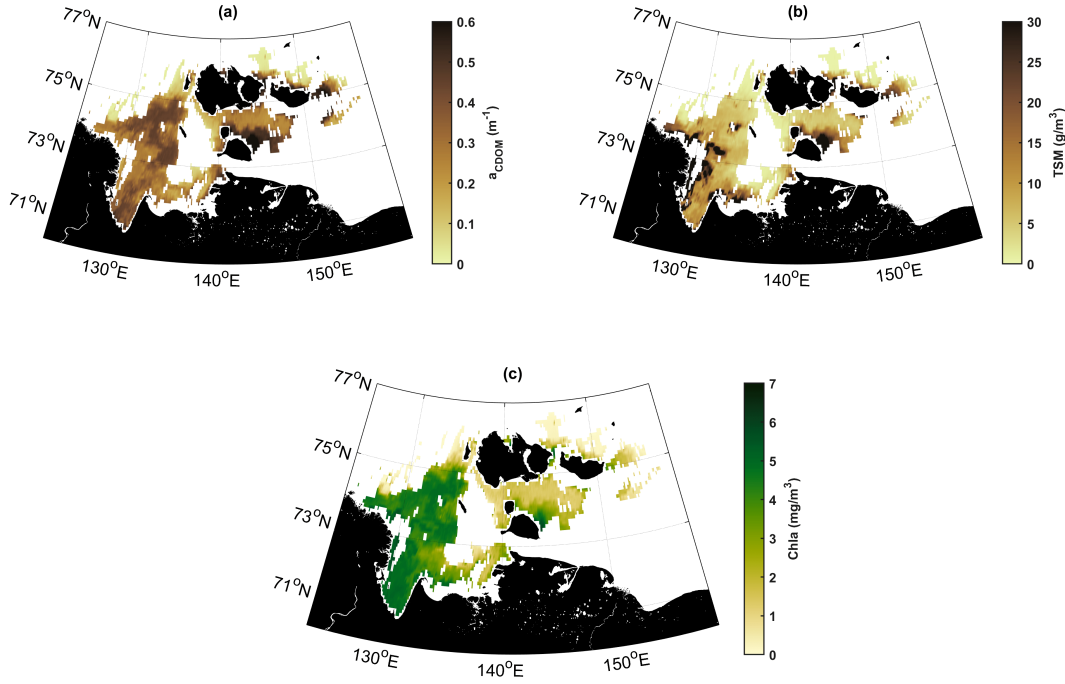


FIGURE 3.6: Spatial distribution of the MERIS retrieved surface: a) CDOM absorption at 443 nm, b) TSM concentration, and c) chlorophyll-a concentration in the Laptev Sea, on August 4, 2010.

By combining satellite remote sensing and radiative transfer modelling, the study is extended and the spatial distribution of the radiative heating in the Laptev Sea for a typical summer day is investigated. Figure 3.6 shows the spatial distribution of the retrieved CDOM absorption, TSM, and chlorophyll-a concentration from the MERIS products, on August 4, 2010. Regions close to the Lena Delta exhibit very high concentrations of TSM, which exceed  $30 \text{ g/m}^3$ . Similarly, very high CDOM absorption ( $0.5 \text{ m}^{-1}$ ) and elevated chlorophyll-a concentrations ( $5 \text{ mg/m}^3$ ), compared to the outer shelf regions, are observed.

The spatial patterns of  $E_{n\text{abs}}$ ,  $\Delta\text{RH}$  and  $\Delta Q_{\text{sum}}$  confirm that the water constituents have a significant influence on the radiative heating in the Laptev Sea surface waters. Here only the spatial distribution of  $\Delta\text{RH}$  is shown (Figure 3.7), as the patterns are very similar for all three parameters (because  $E_{n\text{abs}}$ ,  $\Delta\text{RH}$  and  $\Delta Q_{\text{sum}}$  are interrelated according to the Equations 2.3 - 2.7). The highest  $E_{n\text{abs}}$  occurred over river-influenced waters, where also the  $\Delta\text{RH}$  and  $\Delta Q_{\text{sum}}$  are higher as in our simulations. The values of  $\Delta\text{RH}$  and heat fluxes could also be higher considering that the C2RCC algorithm

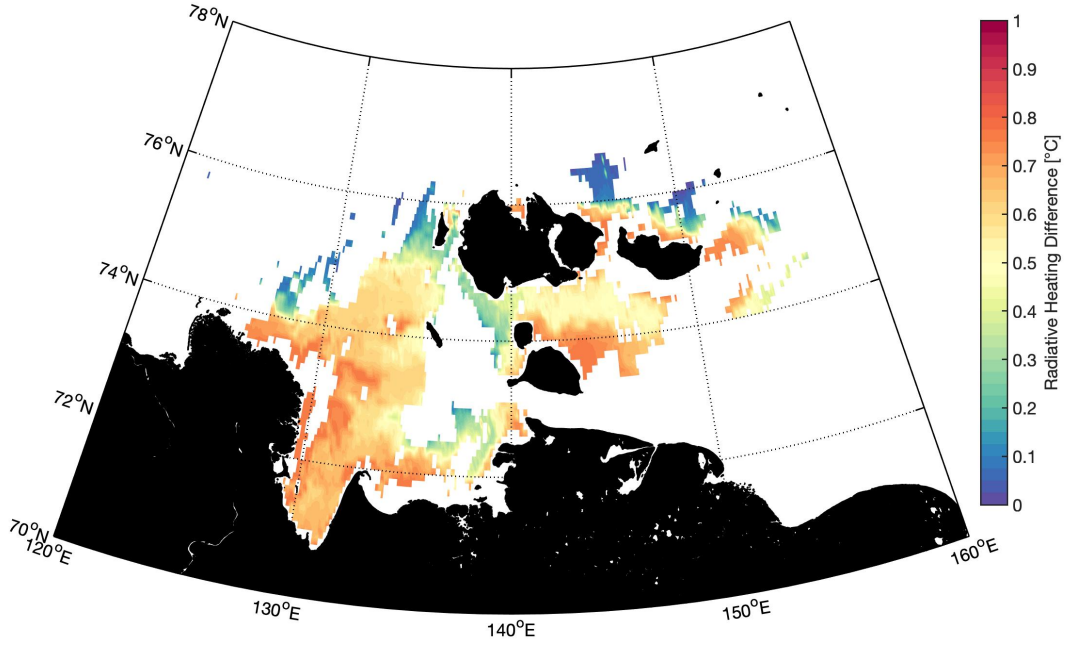


FIGURE 3.7: Spatial distribution of radiative heating difference (1RH, integrated over one day) of the Laptev Sea surface waters (upper 2 m) for August 4, 2010.

underestimates  $a_{\text{CDOM}}(443)$  in the Laptev Sea.

An analysis of the relation between  $E_{\text{nabs}}$ ,  $a_{\text{CDOM}}(443)$ , TSM and Chla reveals a more complex nature of the relationship between the radiative heating and the water constituents that was not efficiently captured by point simulations (Figure 3.8). Although  $E_{\text{nabs}}$  increases with increasing  $a_{\text{CDOM}}(443)$ , the relationship becomes more complex for concentrations of TSM and Chla higher than  $10 \text{ g/m}^3$  and  $3 \text{ mg/m}^3$ , respectively. Under elevated concentrations of TSM and Chla, these particles may cause high scattering, and hence, increased light attenuation in the water; evidence that should be supported by in situ observations in the future.

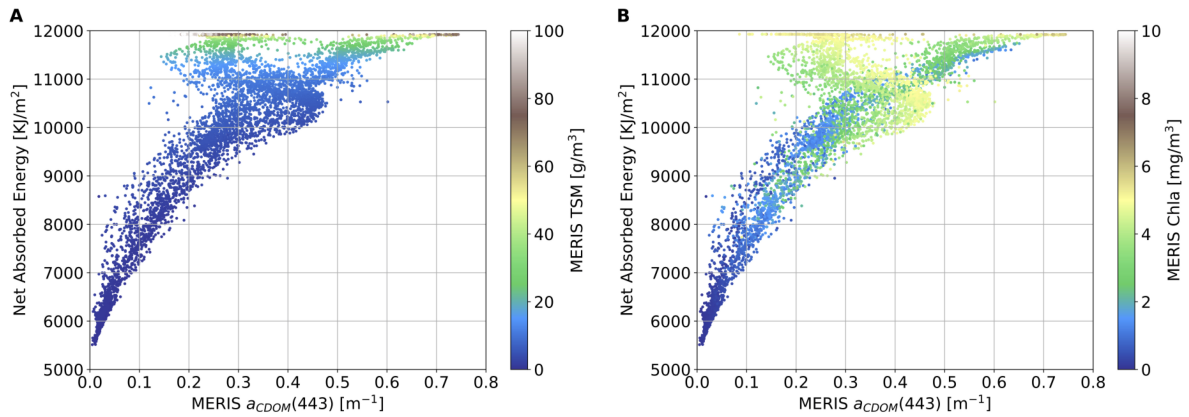


FIGURE 3.8: (A) Scatterplot of  $E_{nabs}$ ,  $a_{CDOM}(443)$  as a function of TSM. (B) Scatterplot of  $E_{nabs}$ ,  $a_{CDOM}(443)$  as a function of Chla.

### 3.3 Conclusions

The effect of optically active water constituents on the radiative heating of Laptev Sea shelf waters has been investigated with the synergy between satellite remote sensing, radiative transfer modelling and *in situ* observations. The results show that the radiative heating of Laptev Sea surface waters is strongly influenced by the concentration of CDOM and TSM. The presence of optically active constituents leads to enhanced absorption and deposition of energy in the upper 2 m of the water column. In the station with the highest CDOM absorption 43% more energy is absorbed (upper 2 m) compared to the station with the lowest absorption, leading to an increased radiative heating rate of 0.6 °C/day. Likewise, waters with a higher amount of CDOM/TSM show an increased sea ice melt rate compared to clearer waters and larger differences in the atmosphere-ocean heat flux. With the exploitation of satellite remote sensing retrievals and RTM, I quantify the spatial distribution of radiative heating in the Laptev Sea. The spatial patterns of radiative heating closely follow the distribution of the optically active water constituents, with the highest energy absorption taking place over river-influenced waters. From the above, it can be concluded that the presence of optically active water constituents can potentially intensify Arctic Amplification due to the positive feedback among radiative heating, near-surface temperature, and sea ice melting.

Conclusions have been drawn from both observational data from various sources and model results, where variables are missing or they are not accessible by observations. Accordingly, this study indicates that the lack of *in situ* measurements can be



compensated to some extent by satellite retrievals in synergy with radiative transfer modelling, which is especially valuable for inaccessible regions like the Laptev Sea. With the increased spatial resolution and temporal coverage of the Siberian shelf regions, future ocean colour sensors specially designed for optically complex waters can advance the investigation of the spatiotemporal variability of radiative heating in these regions.

This study confirms that the absorption of radiation by water constituents is an important parameter to be considered in 3D general circulation models as it affects radiative heating, surface ocean temperatures, and the air-sea heat fluxes. The current generation of coupled general circulation models can neither capture nor spectrally resolve the necessary details of the relevant to water constituents radiative transfer processes. The presented results constitute a step in this direction and aim at improving the parameterizations within general circulation models. A detailed and realistic representation of optical properties such as CDOM and TSM is necessary to accurately model coastal waters and shelf regions that are highly influenced by river runoff.



## Chapter 4

# Amplified Arctic surface warming and sea ice loss due to phytoplankton and CDOM

### 4.1 Introduction

The results of the previous chapter show that the radiative heating of Laptev Sea shelf waters is strongly influenced by the presence of optically active water constituents. It is shown that CDOM and TSM, and to some extent phytoplankton, drive the solar energy absorption in the upper meters of the water column, affecting the sea ice melt rates and the heat flux to the atmosphere. However, this study has been only a first step towards assessing the effect of the optically active water constituents on the Arctic Ocean's heat budget. Based on the previous chapter's findings, the need to investigate the effect of optical constituents within coupled 3D modelling studies, is emphasized.

In this chapter, I upscale the previous one-dimensional and regional study by means of 3D general circulation modelling for the entire Arctic Ocean and the subarctic seas. By operating an ocean biogeochemical model coupled to a general circulation model with sea ice (Darwin-MITgcm), the effect of phytoplankton and CDOM is incorporated into the in-water shortwave radiation penetration scheme. With this interactive parameterization, I examine how the light attenuation by phytoplankton and CDOM contributes to surface warming and sea ice reduction in the Arctic Mediterranean Sea. I quantify the changes attributed to the effect of CDOM and discuss the implications of light attenuation schemes in general circulation models.

In the first section (4.2), the simulated sea ice concentration and extent, as well as the optically active water constituents distribution are compared against observations. It is shown that the model simulates realistically these parameters. The contribution of light attenuation by phytoplankton and CDOM to surface warming and sea ice reduction in the Arctic Mediterranean Sea is examined in the next section (4.3). Section 4.4 deals with the individual effect of CDOM, which is identified as a significant driver of the observed changes. In the first part, its direct thermal effect is discussed, while the next part focuses on the contribution of particular terms of the heat budget that CDOM affects directly and indirectly. The chapter continues with a section discussing the implications arising from the assumptions used in ocean models and closes by discussing the main results, and by drawing conclusions.

### ***Contributions:***

Part of this chapter's results have been published in *Geophysical Research Letters* (Pefanis et al., 2020). I, together with Dr. Svetlana Losa, developed the part of the code within MITgcm to account for the effect of phytoplankton and CDOM into the in-water shortwave radiation penetration scheme. Then, I compiled the model, conducted the numerical simulations, carried out the analysis, and wrote the manuscript. Dr. Svetlana Losa, Dr. Martin Losch, Prof. Astrid Bracher, and Dr. Markus Janout, provided substantial guidance and important comments during the writing, editing, and review of the manuscript. Prof. Torsten Kanzow also provided substantial guidance and comments, especially for the Section 4.4 of this chapter.

## **4.2 Model evaluation**

### **4.2.1 Sea ice**

The first metric used for the sea ice model's evaluation is "sea ice concentration" (SIC). SIC describes the fraction of a model grid cell's surface that is covered by ice. Then "sea ice extent", which defines a region as either "ice-covered" or "ice-free", is derived. If a model grid cell has more ice concentration than a critical value, then the cell is labeled as "ice-covered". To be consistent with observations, the SIC threshold used

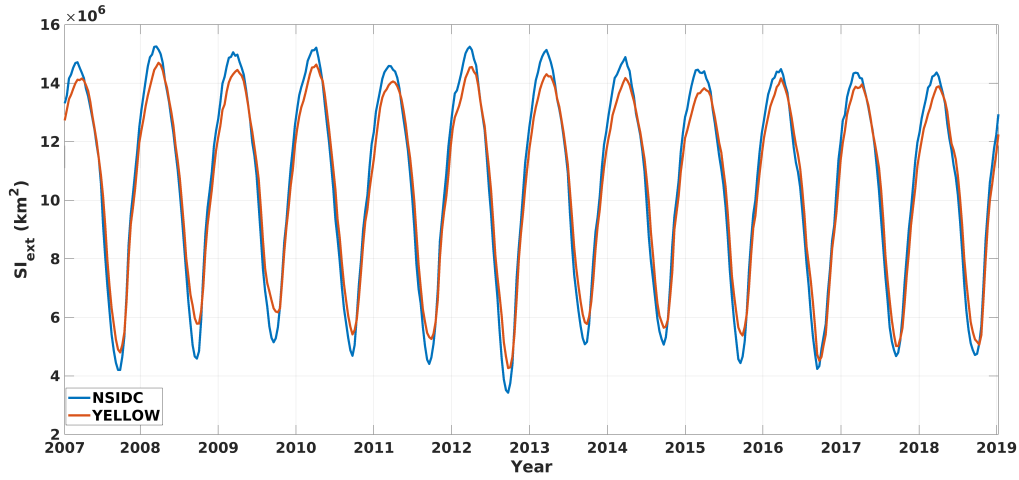


FIGURE 4.1: Temporal variation of observed (blue line) and simulated sea ice extent in YELLOW (red line), in the northern hemisphere during the 2007-2019 period. Data comes from the NOAA/NSIDC Climate Data Record of Passive Microwave sea ice Concentration, Version 3 (Peng et al., 2013)

to determine this labeling is 15%.

The simulated SIC and sea ice extent from the YELLOW run are compared against observations from passive microwave remote sensing. Figure 4.1 shows that the sea ice model within MITgcm simulates realistically the temporal variation of the northern hemisphere's sea ice extent during the 2007-2018 period. The simulated extent matches the observed seasonal cycle and variability. Although the model slightly underestimates the winter maximum extent and overestimates the summer minimums most of the years, it captures the observed trends and the overall sea ice decline. Moreover, it captures the summer sea ice extent minimum record in 2012 (Parkinson and Comiso, 2013), as well as the second and third lowest minimums in 2007 and 2016, respectively (Fig. 4.1).

As a next step for the evaluation of the sea ice model, the spatial distribution is compared against the passive microwave observations for the 2012 sea ice minimum, coming with an average horizontal resolution of 25 km (Fig. 4.2a, b). The general spatial pattern of the simulated sea ice distribution bears enough resemblance to satellite observations to be useful for this sensitivity study. The model reproduces the seasonal sea ice retreat along the Siberian and Alaskan coasts, but SIC is overestimated in the

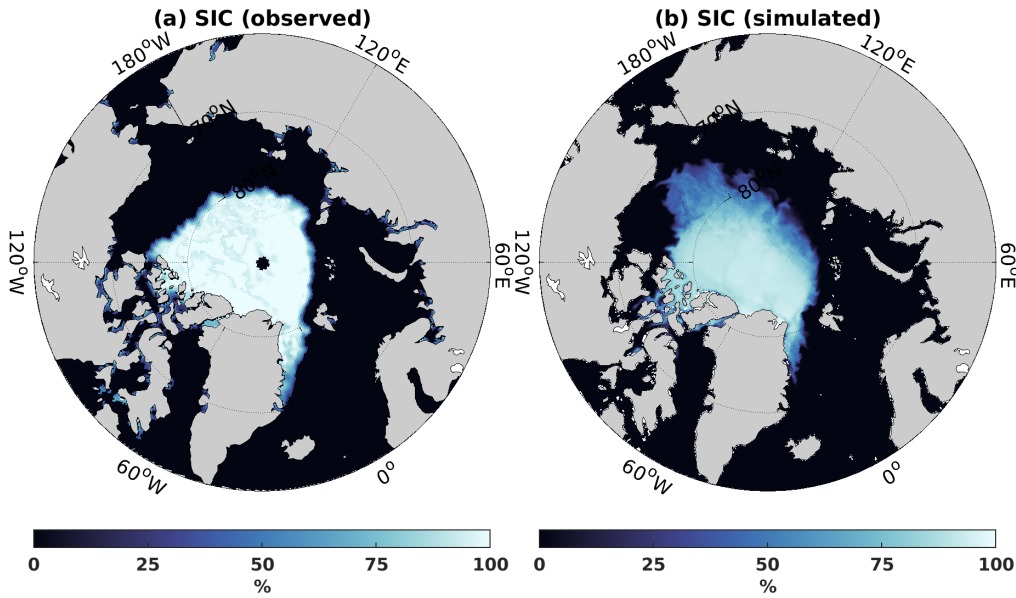


FIGURE 4.2: For September 2012: a) simulated SIC in YELLOW, b) observed SIC from the NOAA/NSIDC Climate Data Record of Passive Microwave sea ice Concentration, Version 3 (Peng et al., 2013).

Beaufort Sea and underestimated in areas close to the Laptev Sea (Fig 4.2b).

## 4.2.2 Water constituents

The simulated surface chlorophyll-a concentrations and CDOM absorption are found to be in a similar range to the observed chlorophyll-a concentrations and the absorption by coloured dissolved and detrital matter (CDM) (Fig. 4.3a-d). Except for some of the coastal regions, like the Kara Sea, they follow the observed spatial patterns. However, it should be minded that satellite chlorophyll-a estimates are known to be highly overestimated close to the Siberian shelf (Heim et al., 2014). Furthermore, CDM accounts for the absorption from both detritus and dissolved material. Despite its different definition, it is still the most suitable remote sensing product to compare against simulated CDOM.

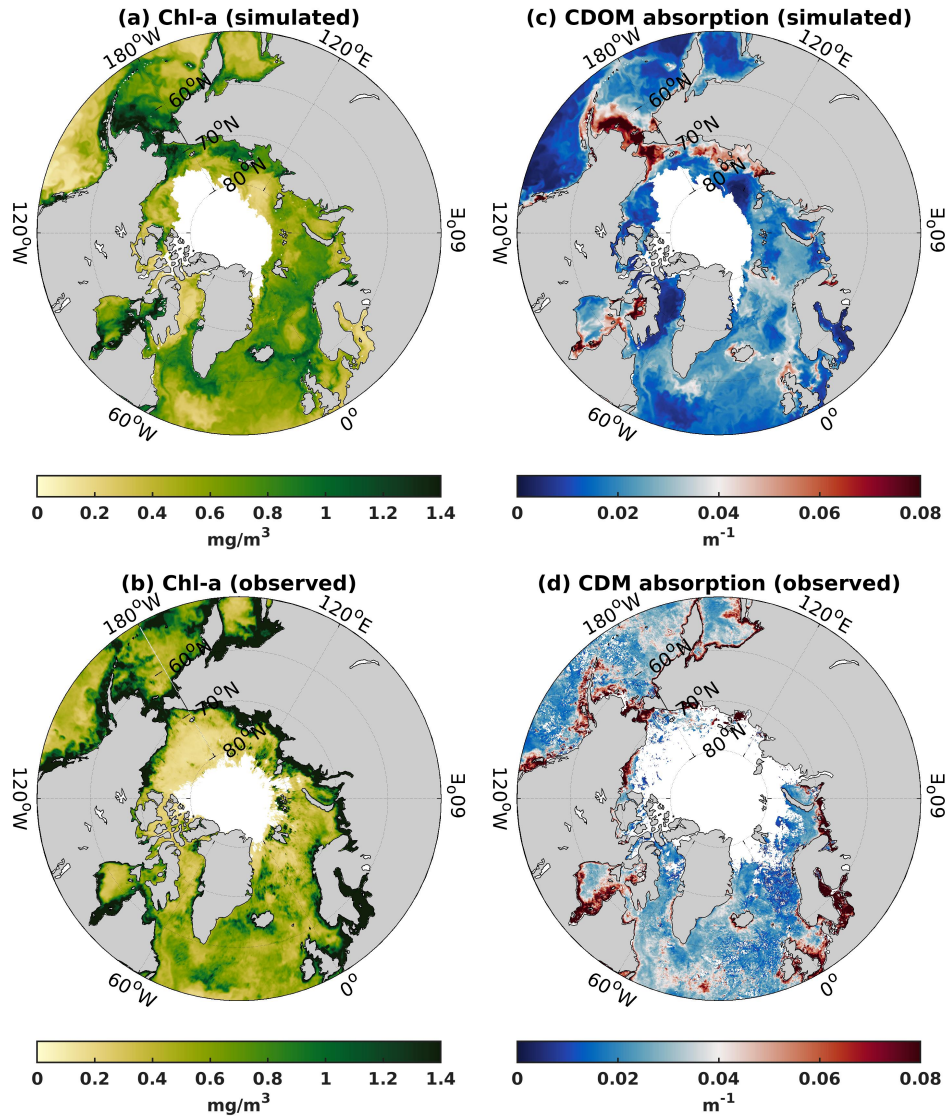


FIGURE 4.3: For September 2012: a) simulated surface chlorophyll concentrations in YELLOW, b) observed surface chlorophyll concentrations (Gohin, Druon, and Lampert, 2002) from the merged GlobColour product (<ftp://ftp.hermes.acri.fr/GLOB/merged/>), c) simulated surface absorption by CDOM in YELLOW, d) observed surface absorption of colored dissolved and detrital matter (CDM) at 443nm (Werdell et al., 2013) from the NASA GSF Center (<https://oceandata.sci.gsfc.nasa.gov/MODIS-Aqua/Mapped/Monthly/4km/>). Although CDM accounts for the absorption from both detritus and dissolved material, it is the most suitable remote sensing product to compare against simulated CDOM.

### 4.3 Accounting for the effect of biogeochemistry in light attenuation

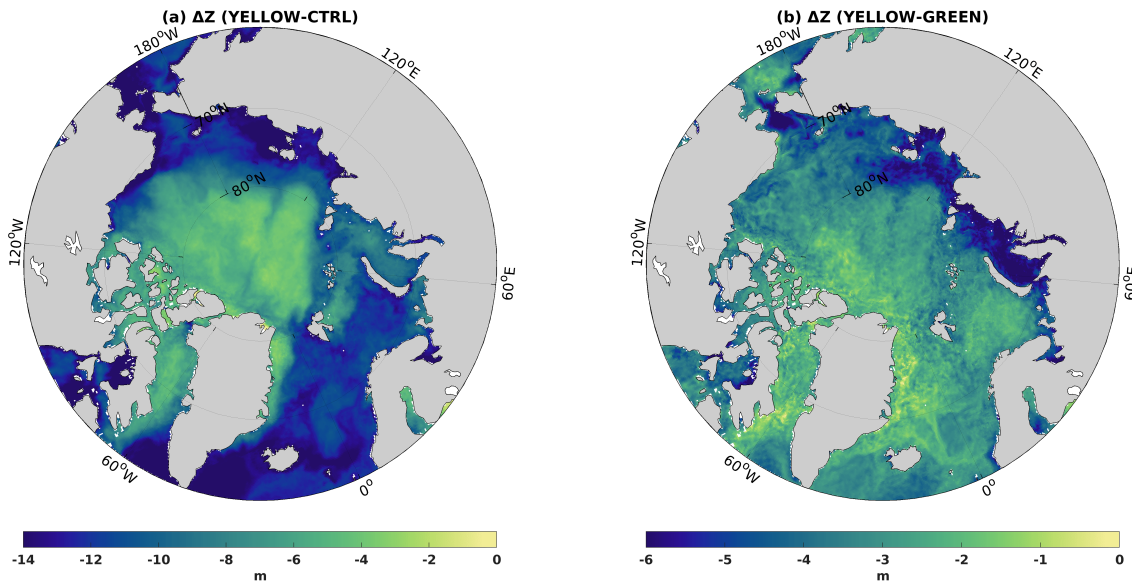


FIGURE 4.4: Light attenuation depth differences ( $\Delta Z$  in m) between: a) YELLOW and CTRL, b) YELLOW and GREEN. The light attenuation depth ( $Z$ ) is the reciprocal of the diffuse attenuation coefficient  $K_d$ . The values here account for the upper 10 m during the sunlit season, and when they are negative, they indicate a shallower light attenuation depth. The sunlit season is the time period when the mean shortwave downwelling radiation over the Arctic ( $> 66^\circ\text{N}$ ) exceeds 25% of the annual maximum. Depending on the year, it roughly corresponds to the period from April to September.

Including the effect of simulated chlorophyll-*a* and CDOM to the light attenuation parameterization (YELLOW), decreases the attenuation depth ( $Z$ , in m) comparing to CTRL (Fig. 4.4a). The attenuation depth is shallower throughout the entire Arctic Ocean and the sub-polar seas (Fig. 4.4a). The shallowing is more pronounced in the shelf and the Nordic Seas, where it reaches 18 m, reflecting the high surface concentrations of chlorophyll-*a* and CDOM there (Fig. 4.2a). On average, the attenuation depth decreases by 8.8 m or 38% compared to CTRL.

A part of this shallowing is attributed to CDOM, especially in the Siberian shelf (Fig. 4.4b). In some regions close to Greenland, there is either no difference, or a slight increase (not shown) in the attenuation depth in YELLOW, comparing to GREEN



experiment. This signal comes from the decreased attenuation by the chlorophyll-*a* term in regions and times of the year, where the CDOM effect is almost negligible. The attenuation depth differences range from 0.2 m to -9.1 m, with an average shallowing of 3.3 m or 18.9% in YELLOW, compared to GREEN. In terms of regional changes, the maximum shallowing is observed in Kara and Laptev Sea (-5.3 and -5.1 m on average, respectively), while in Baffin Bay and the Barents Sea it is limited to -2.7 and -2.9 m (Fig. 4.4b).

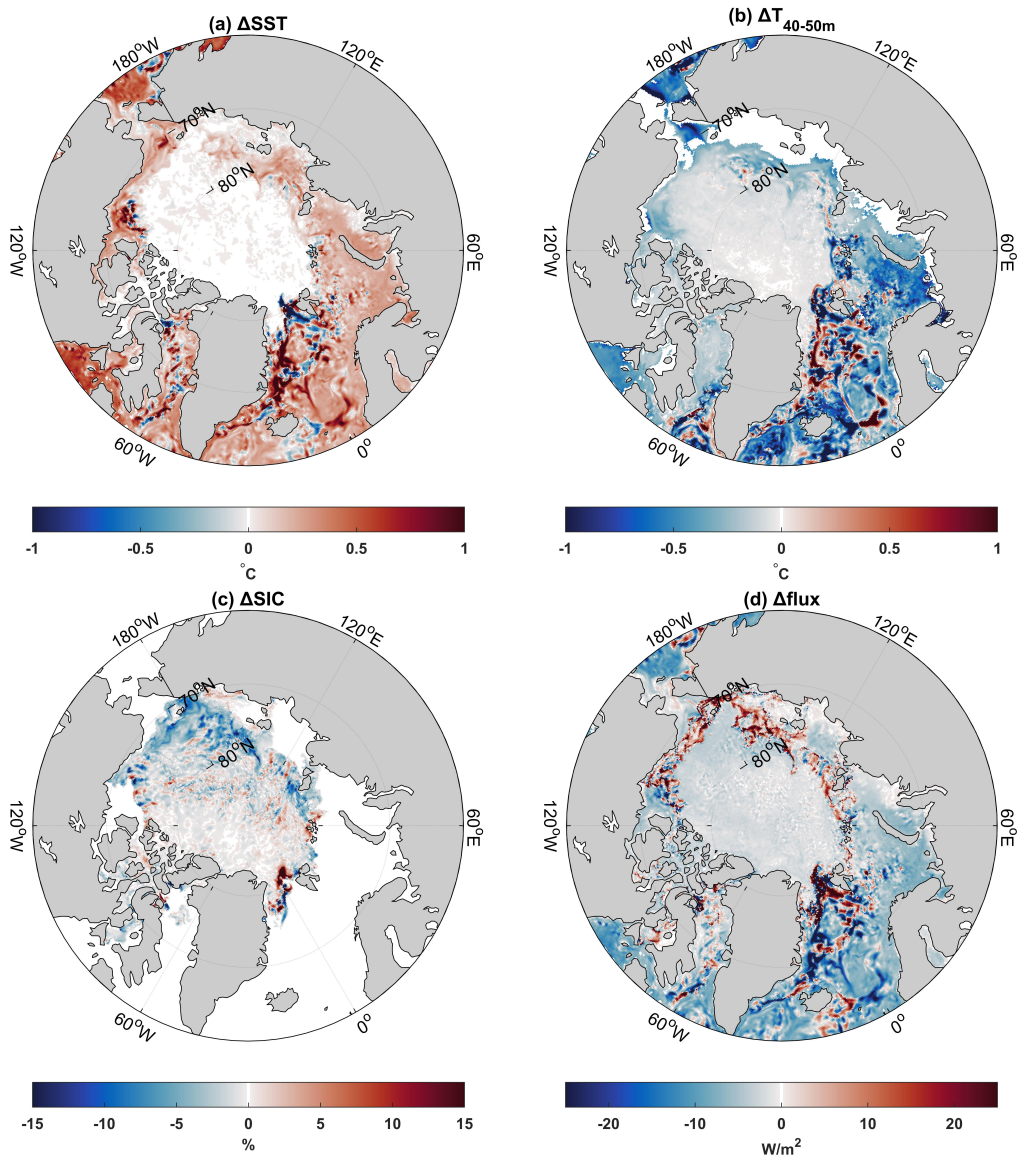


FIGURE 4.5: Mean differences between YELLOW and CTRL for: a) SST, b) 40-50 m temperature, c) SIC and d) surface heat flux (Eq. 2.15; positive changes indicate heat gain for the ocean), for August 2012.

Chlorophyll-a and CDOM, by shoaling the light attenuation depth, cause more heat absorption close to the surface of the ocean. Accounting for their effect on the model's light attenuation scheme leads to higher SST during summer (YELLOW-CTRL), almost in the entire Arctic. Surface temperature differences in summer are generally in the range of  $0.1 - 1^\circ\text{C}$  with the maximum increase observed in the Greenland Sea, being above  $1^\circ\text{C}$  (Fig. 4.5a). Limited surface cooling close to the sea ice edge is associated with a local increase of upwelling. Upwelling tends to dump the signal of the increased surface temperature by bringing colder waters from the sub-surface layer. Since the available heat at depth is reduced, the sub-surface layer is colder than in CTRL, almost everywhere (Fig. 4.5b). At the same time, sea ice is reduced mainly in the Eastern Arctic (Fig. 4.5c). With the dynamic attenuation due to chlorophyll-a and CDOM, the SIC distribution in the summer of 2012 is slightly improved (Fig. 4.2, Fig. 4.5c), compared to CTRL. Summertime surface warming induces more heat loss to the atmosphere (Fig. 4.5d) primarily through latent and sensible heat flux. The local heat gain close to the-sea ice edge, however, is directly linked to reduced SIC (Fig. 4.5d).

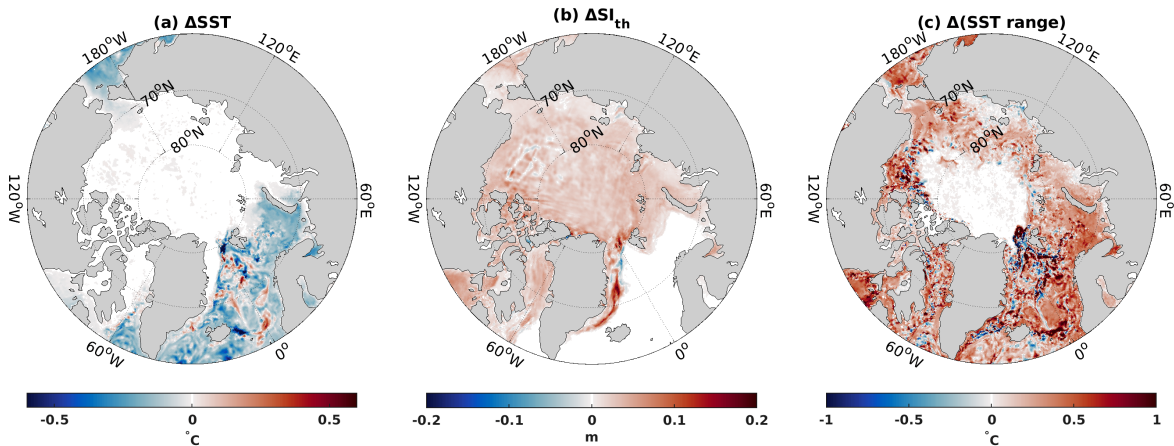


FIGURE 4.6: Mean differences between YELLOW and CTRL over 2007-2016, for: a) SST in December, b) Sea ice thickness ( $SI_{th}$ ) in February, c) annual range of SST. December and February are the wintertime months with the largest differences observed in SST and  $SI_{th}$ , respectively.

In contrast to the summertime surface warming, lower SSTs occur in winter (Fig. 4.6a). During wintertime, surface cooling leads to enhanced ice formation. The sea ice becomes thicker in the entire ice domain, with a maximum increase in the Greenland Sea (Fig. 4.6b). These changes are accompanied by an amplified seasonal cycle of

SST in the YELLOW run compared to CTRL (Fig. 4.6c), implying also changes in temperature extremes (Gnanadesikan, Kim, and Pradal, 2019). The latter may have ecological implications since many marine organisms live within a specific temperature range.

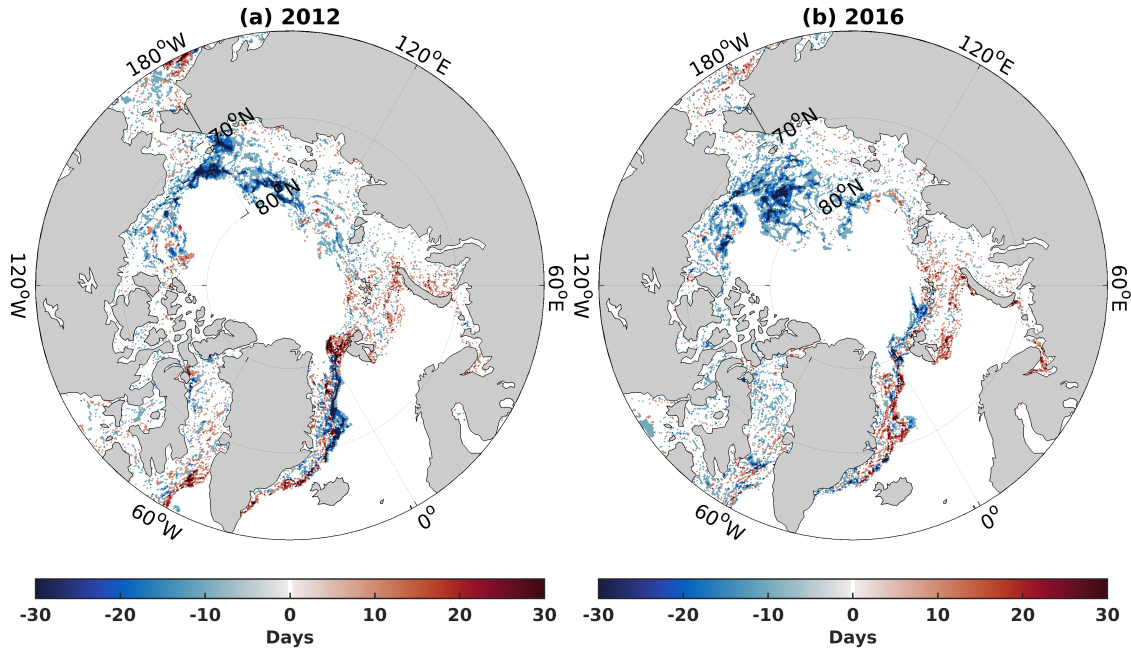


FIGURE 4.7: Difference between YELLOW and CTRL in days with more than 15% SIC, for a) 2012, and b) 2016.

To have a better look at the radiative effect of phytoplankton and CDOM on sea ice over the year, the ice-covered season in 2012 and 2016 is examined. This metric is defined as the number of days that a model's grid cell has more than 15% SIC. 2012 was the year with the summer sea ice extent minimum record (Parkinson and Comiso, 2013), while 2016 was characterized by a record-late freeze-up in the central Arctic (Petty et al., 2018). Consequently, some of the largest differences within the entire period (2007-2016) are observed in these two years. By accounting for the combined effect of phytoplankton and CDOM (YELLOW-CTRL), the ice-covered season is reduced by at least 10 days in an area of 1.05 and 0.95 million km<sup>2</sup>, in 2012 and 2016 respectively. In some parts of the Eastern Arctic and the Canadian basin, the decrease is in the order of one month (Fig. 4.7a,b). Apart from these years, a persistent reduction is observed in this part of the Arctic Ocean, throughout the simulated period. The shorter ice-covered season there is attributed to the fact that sea ice is

very thin during the summer melt onset and the autumn freeze-up (August–November, not shown). Hence, sea ice is particularly susceptible to small changes in SST, induced by the optical forcing of the water constituents.

Over the examined period (2007–2016), the mean SST of the warmest climatological month (July) in the Arctic Ocean increases by 0.3°C (YELLOW-CTRL). From June to September of 2012, 48% of the observed differences in the SST over the Arctic (YELLOW-GREEN) are attributed to the effect of CDOM. Furthermore, the ice-covered season in 2012 and 2016 is reduced by at least 10 days in an area of 0.54 and 0.59 million km<sup>2</sup>, due to the CDOM effect. These areas, with shorter ice cover, account for almost 50% of the total changes (YELLOW-CTRL), discussed in the previous paragraph. These findings prompt me to investigate in detail the individual effect of CDOM light absorption by comparing the YELLOW model run to the GREEN (Section 4.4).

## 4.4 CDOM light absorption effect

The majority of general circulation models, use either constant light attenuation depths or in case of the inclusion of interactive biogeochemistry, schemes that depend only on the concentration of chlorophyll-*a*. Here, it is shown that adding CDOM (YELLOW) to the chlorophyll-based attenuation scheme (GREEN), leads to further near-surface heat absorption, amplifying the summertime warming pattern induced by chlorophyll-*a* alone (Fig. 4.8a). By confining the heating from the solar radiation close to the surface, CDOM reduces the available heat with depth, and hence, it enhances the subsurface cooling (YELLOW-GREEN) (Fig. 4.8b). In summer, the effect of CDOM further reduces sea ice (Fig. 4.8c), while the warming of the surface ocean results in increased heat loss to the atmosphere (Fig. 4.8d).

In contrast to Kim et al., 2018b, the annual mean SST is slightly increased due to the CDOM absorption. The largest differences are observed in the sub-polar North Atlantic, with maximum warming in the Norwegian Sea, a region associated with advective transport from lower latitudes (Fig. 4.9). Whereas, a limited cooling effect takes place close to Greenland and in parts of the Iceland Sea over the 2007–2016

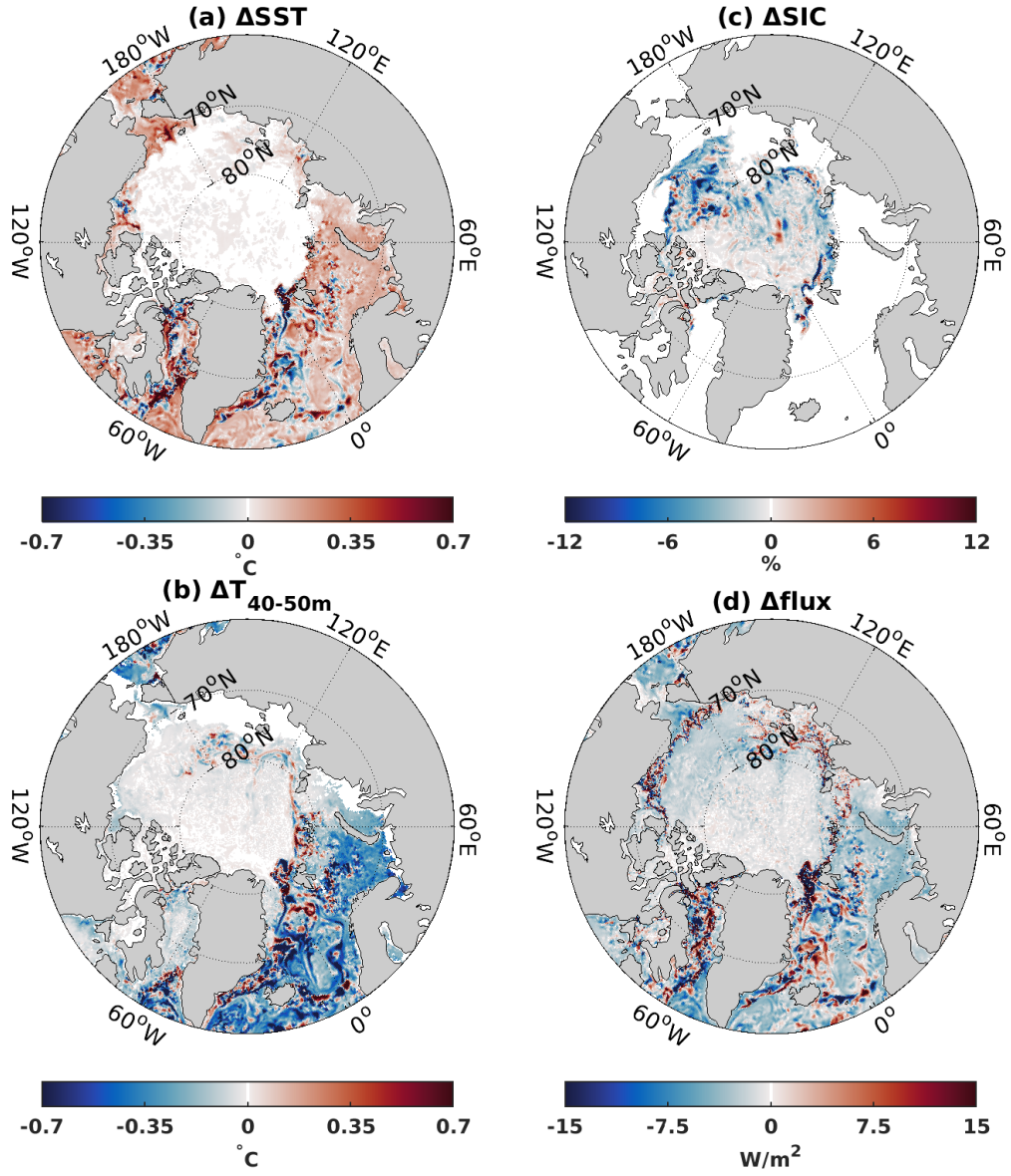


FIGURE 4.8: Mean differences between YELLOW and GREEN in the summer of 2016, for: a) SST, b) 40-50 m temperature, c) SIC and d) surface heat flux (Eq. 2.15). The temperature and heat flux differences are calculated for the August, while SIC for the September of 2016.

period.

The induced local changes in temperature result from the direct thermal effect of altering the light attenuation profile and the indirect dynamical effect, which affects the MLD (Fig. 4.10a). Two indirect mechanisms may cause a non-local effect: 1) differential surface heating along chlorophyll-a and CDOM concentration gradients induces horizontal density gradients, which modify the structure of geostrophic velocity



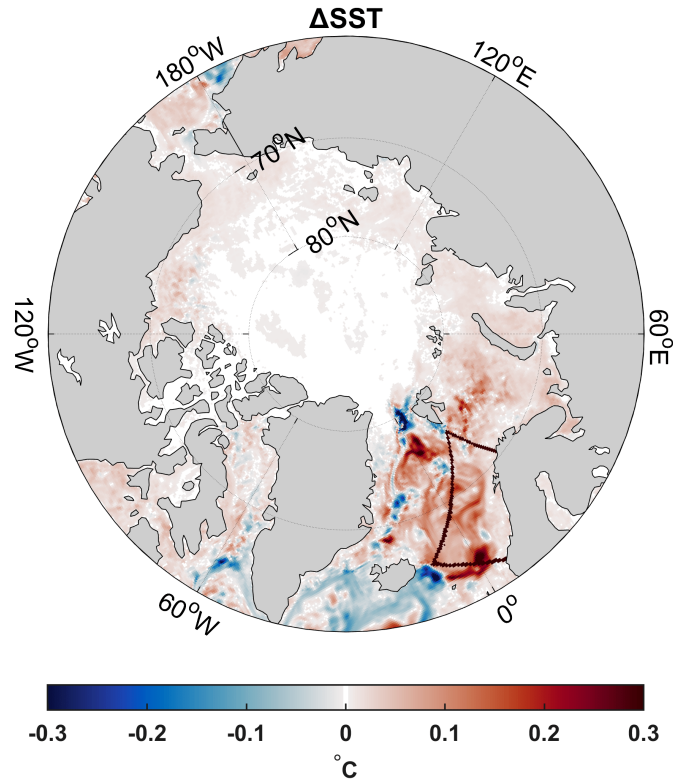


FIGURE 4.9: Annual mean SST differences (YELLOW-GREEN) for the 2007–2016 time period. The area enclosed by the black line is referred to the text as the Norwegian Sea.

and hence the advective flux (Fig. 4.10b), and 2) changes of SIC close to the sea ice edge also affect the density through insolation and salinity differences. In late spring and summer, the direct effect dominates due to high solar input and the development of the thermocline, but also due to the abundance of optical constituents. In contrast, there is little light in winter, and the upper ocean is known to be well mixed so that indirect effects, originating from the direct thermal effect in summer, may be important.

#### 4.4.1 Surface heat flux components

The surface heat flux is the exchange of heat, per unit area, crossing the ocean-atmosphere interface (Section 2.2.4). It comprises the radiative component split in a shortwave and a longwave part (Eq. 2.16 - 2.17), and the turbulent components which are the latent and the sensible heat flux (Eq. 2.19 - 2.20) depending on the

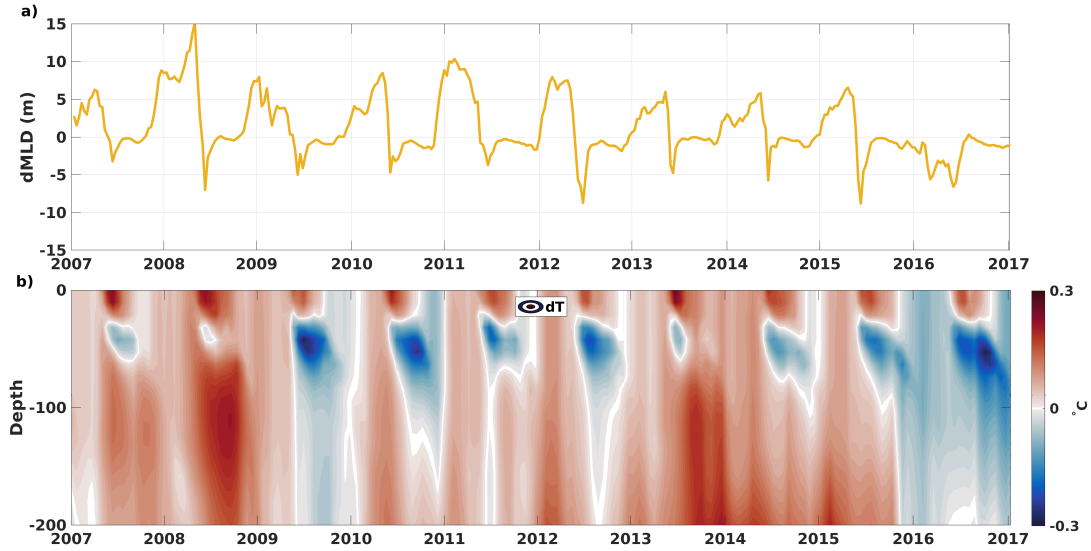


FIGURE 4.10: Mean differences (YELLOW-GREEN) in the Norwegian Sea (Fig. 4.9) in: a) the mixed layer depth (dMLD), b) the upper 200 m temperature profile (dT). The MLD differences for this region are on the order of 5% (winter) to 15% (summer).

temperature difference with the atmosphere, and on the evaporation.

In section 4.4, it is shown that accounting for the effect of CDOM on the light attenuation, increases the SST in summer, reduces sea ice, and induces more heat loss to the atmosphere. Figure 4.11 shows the spatial distribution of changes (YELLOW-GREEN) for every component of the surface heat flux, from June to September. By having a look first at the ice domain, the sea ice decline (Fig. 4.8 a) and thinning (not shown) allows more shortwave radiation to penetrate the ocean (Fig 4.11a), having an opposite sign effect to the total heat flux changes in the Arctic (Fig. 4.8 d). On the other hand, the turbulent fluxes of sensible and latent heat drive the summertime losses in the ice-free regions (Fig 4.11b,c). To a lesser extent, the ocean loses heat through the longwave radiation emitted from the surface (Fig 4.11d).

The examination of the monthly mean differences (Fig. 4.12) gives some insight of how the changes in the surface heat flux components evolve throughout the year. In correspondence with Figure 4.11, the summertime heat loss is primarily driven by the sensible and latent heat flux, and secondarily by longwave radiation, both in the entire Arctic (Fig. 4.12 left) and regionally (Fig. 4.12 middle, right). However, two

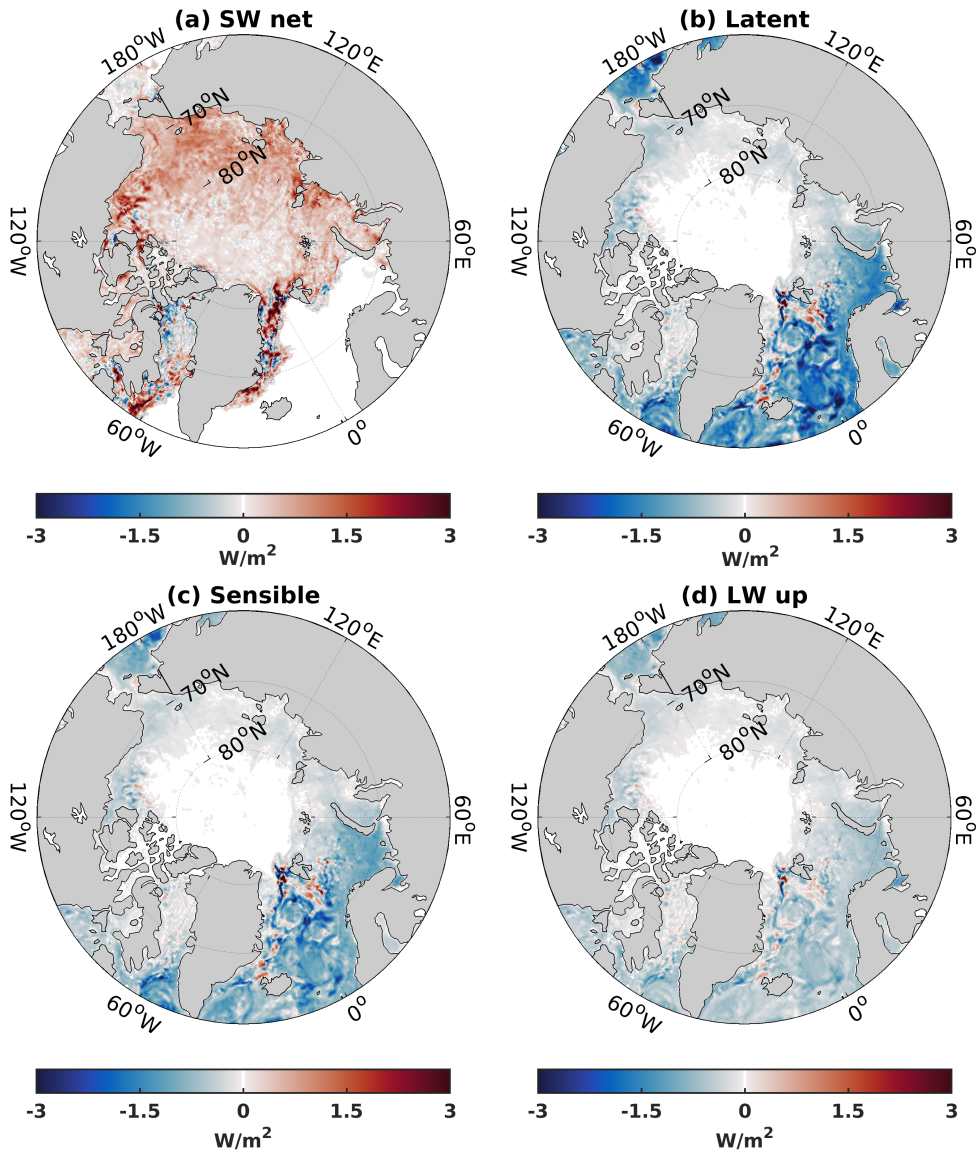


FIGURE 4.11: Mean differences between YELLOW and GREEN for: a) shortwave net radiation (SW net), b) latent heat flux, c) sensible heat flux and d) longwave upwelling radiation (LW up), from June to September (2007-2016) (Eq. 2.16 - 2.20).

distinct cases are identified. Regions close to the central Arctic, like the Laptev Sea ( $105\text{-}150^\circ\text{E}$ ), are directly affected by the extent of the sea ice during summer and early autumn. As a result, the differences in the shortwave heating term are larger than in the net upward heat flux (Fig. 4.12 middle), counterbalancing any temperature-induced losses there. In late autumn and winter, the formation of sea ice insulates the ocean from the atmosphere, alleviating any heat exchange (Table 4.1). On the contrary, in regions that are characterized of ice-free conditions most of the year, as



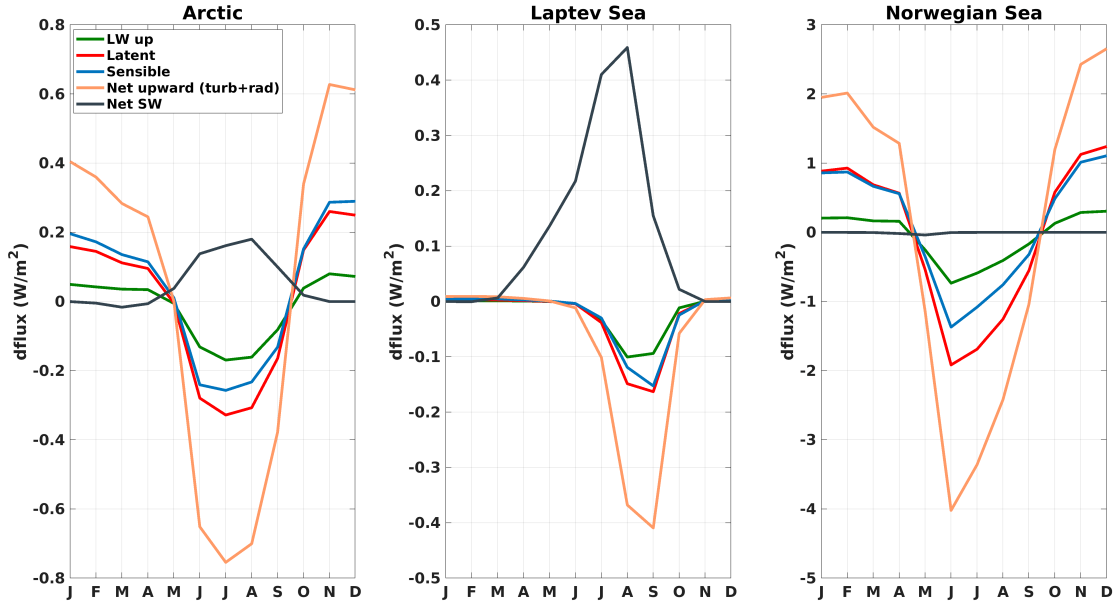


FIGURE 4.12: Monthly mean differences between YELLOW and GREEN for the components of the surface heat flux (2007-2016). **Left panel:** Average over the Arctic ( $>66^\circ N$ ). **Middle panel:** Average over the Laptev Sea. **Right panel:** Average over the Norwegian Sea. Net upward flux is the sum of the latent, sensible and longwave upwelling (LW up) fluxes (negative sign denotes heat loss for the ocean). Following Pabi, Dijken, and Arrigo (2008), as Laptev Sea is considered the region between  $105^\circ$  and  $150^\circ E$ .

the Norwegian Sea, the changes in surface shortwave heating are negligible (Fig. 4.12 right). Hence, there is nothing to balance the net heat loss during spring and summer. From June to September, the difference in heat loss (YELLOW-GREEN) is on average  $2.4 \text{ W/m}^2$  in the Norwegian Sea (Table 4.1). Since the surface layer is mostly colder during winter (YELLOW-GREEN), there is a decrease in sensible, latent and net longwave radiation heat losses (Fig. 4.12 left, right).

#### 4.4.2 Heat budget analysis

In order to understand the annual cycle of temperature differences when CDOM absorption is considered (YELLOW), I perform a heat budget analysis according to

TABLE 4.1: Differences (YELLOW-GREEN) in the surface heat flux components averaged over the Arctic ( $>66^\circ N$ ), the Laptev Sea, and the Norwegian Sea. Values are calculated for two seasons, the local summer and winter. Notation is the same as in figures 4.11 and 4.12. Please note that I have considered different months for the summer and winter seasons in every region. The unit is  $W\ m^{-2}$ .

Region	Season	SW net	Latent	Sensible	LW up	Net upward
Arctic	Jun to Sep	0.15	-0.27	-0.22	-0.14	-0.62
Arctic	Nov to Feb	0.00	0.20	0.24	0.06	0.50
Norwegian Sea	May to Sep	-0.01	-1.19	-0.78	-0.43	-2.40
Norwegian Sea	Nov to Feb	0.00	1.05	0.96	0.25	2.26
Laptev Sea	Jul to Sep	0.34	-0.12	-0.10	-0.08	-0.29
Laptev Sea	Nov to Apr	0.01	0.00	0.00	0.00	0.01

Equation 2.12. The heat budget terms governing temperature changes are investigated for the entire Arctic, but also for specific regions that are characterized by different balances, namely the Laptev and the Norwegian Sea. Below, the individual contribution of every term affecting the upper ocean heating is discussed.

### Local forcing

This heat budget component (Eq. 2.12,  $F_\theta$  term) accounts for the heating from shortwave radiation and for the surface heat exchange with the atmosphere (Section 2.2.4). It is the term most directly associated with changes in the light attenuation due to the presence of CDOM. Considering the penetrative nature of shortwave radiation, the contribution of this component is redistributed vertically. As shown in Section 4.4, CDOM confines heat absorption close to the surface, especially in the summer-time period. Consequently, a cooling effect of the local forcing term is observed at the sub-surface, mostly between 15 and 50 m (Fig. 4.13a, 4.14a, 4.15a). By integrating this effect ( $W\ m^{-3}$ ) over depth, the CDOM contribution can be expressed as a heat flux ( $W\ m^{-2}$ ). Therefore, during summer (as defined in Table 4.1), the integrated effect from 10 to 100 m leads to cooling by 1.55, 4.10, and 3.01  $W\ m^{-2}$  in the Arctic, Norwegian, and Laptev Sea, respectively (Table 4.2). During the local winter, however, a warming of 0.18  $W\ m^{-2}$  is observed in the Arctic, a cooling of 0.57  $W\ m^{-2}$  in the

Norwegian Sea, while there is almost zero effect in the Laptev Sea (Table 4.2).

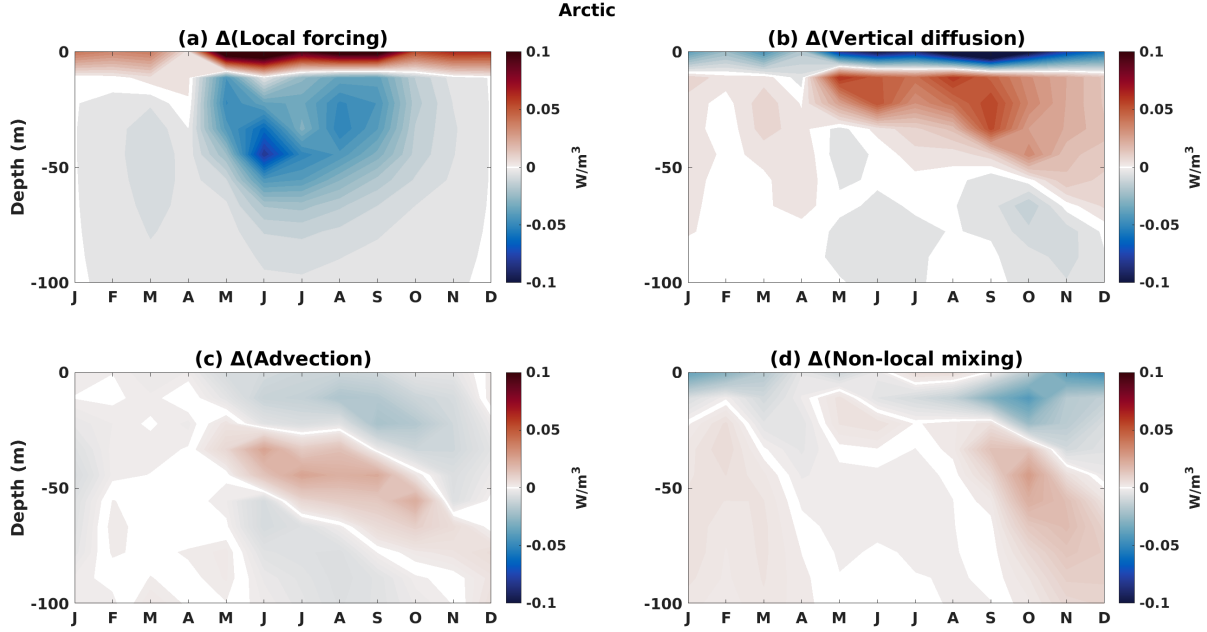


FIGURE 4.13: Monthly mean differences between YELLOW and GREEN in the components of the heat budget for the upper 100 m of the water column: a) in local forcing, b) in vertical diffusion, c) in advection, and d) in non-local mixing. The values are averages over the Arctic ( $>66^\circ N$ ) in  $W/m^3$ .

### Vertical diffusion

The vertical diffusion term (Eq. 2.12,  $D_\theta$  and Eq. 2.21, local term) is directly linked to the local forcing term. As shown in the previous paragraph, heat does not penetrate as deep when the CDOM effect is considered (YELLOW-GREEN). The vertical diffusion term diffuses the signal of increased shortwave heating at the surface, to larger depths. Therefore, a cooling effect of this term is observed at the surface, while diffusion at larger depths leads to warming (Fig. 4.13b, 4.14b, 4.15b).

Changes in vertical diffusion at the surface roughly balance the changes in short-wave heating in summer (Table 4.2). The depth until which vertical diffusion strongly

contributes to the temperature tendency depends on the region. In regions characterized by a very shallow mixed layer, like the Laptev Sea, its contribution is confined in the upper 30 to 40 m (Fig. 4.15b). On the contrary, in the Norwegian Sea, it may contribute to the entire upper 100-meter layer (Fig. 4.14b). In a temporal sense, the maximum of the vertical diffusion effect is observed in summer, which ranges from early May to late September depending on the region (Fig. 4.13b, 4.14b, 4.15b). In fall and winter, its effect at the sub-surface is larger than that of the local forcing term (Table 4.2). The integrated effect from 10 to 100 m and averaged over the local summer period, leads to sub-surface warming by 0.66, 1.66, and 1.58  $\text{W m}^{-2}$  in the Arctic, Norwegian, and the Laptev Sea respectively (Table 4.2). Similarly, the integrated warming in winter for these three regions is 0.36, 1.92, and 0.25  $\text{W m}^{-2}$  (Table 4.2).

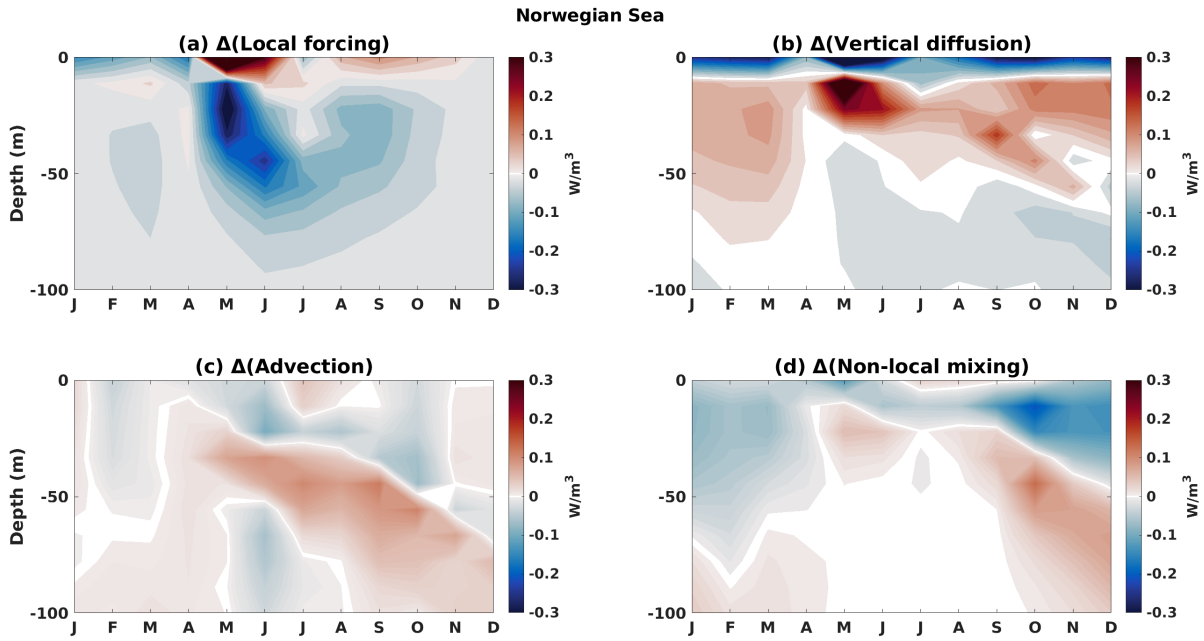


FIGURE 4.14: Same as Fig. 4.13, except for the values are averages over the Norwegian Sea in  $\text{W/m}^3$

## Advection

The tendency due to temperature advection in every dimension within the model, is represented by this term (Eq. 2.12, first two terms on the right hand side). As

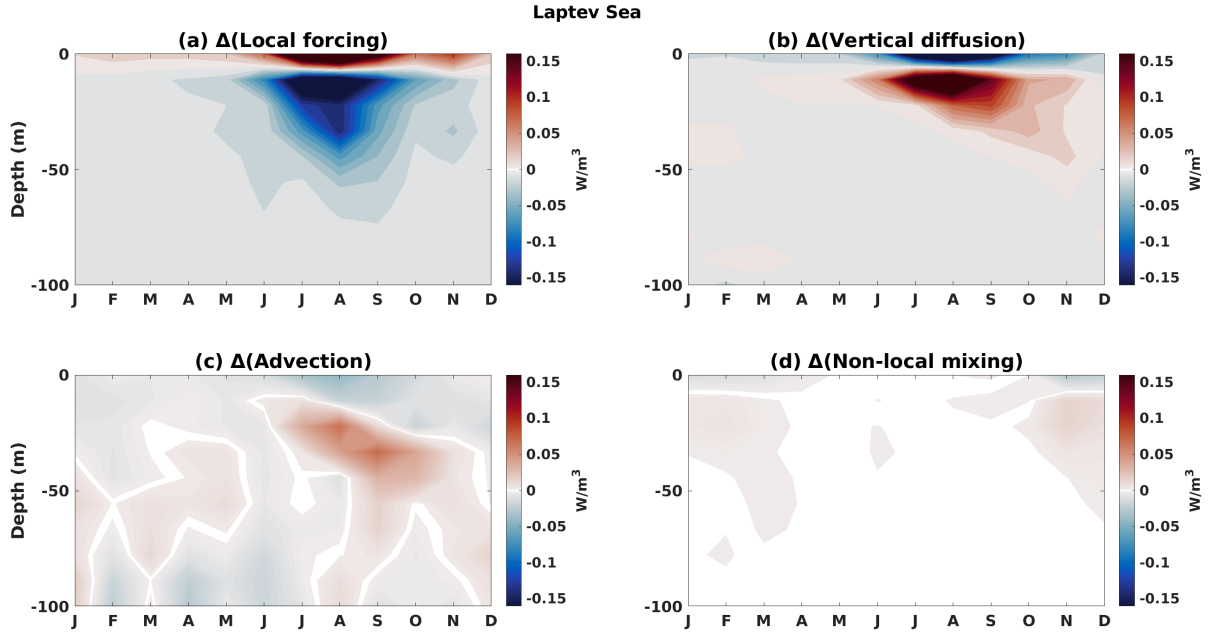


FIGURE 4.15: Same as Fig. 4.13, except for the values are averages over the Laptev Sea ( $105\text{-}150^\circ\text{E}$ ) in  $\text{W}/\text{m}^3$ .

discussed in Section 4.4, differential heating due to CDOM light absorption induces horizontal density gradients which modify the structure of velocity, and hence, the advective fluxes. In the YELLOW simulation, sub-surface heating by advection is observed most of the year. This effect is prominent from summer to winter in the Norwegian Sea (Fig. 4.14c), and from July to November in the Laptev Sea (Fig. 4.15c, Table 4.2). Over the Arctic, slight warming is observed from May to December in the sub-surface, and a minor contribution to cooling in the surface. The integrated advection effect from 10 to 100 m in summer, is a warming of 0.03, 1.21, and  $0.74 \text{ W m}^{-2}$  in the Arctic, Norwegian, and Laptev Sea, respectively (Table 4.2). Similarly, the wintertime effect is -0.13, 0.53, and  $0.07 \text{ W m}^{-2}$  (Table 4.2). In the Norwegian Sea, in particular, the sub-surface advection signal ( $0.53 \text{ W m}^{-2}$ ) is of the same order as the local forcing term ( $-0.57 \text{ W m}^{-2}$ ), counterbalancing its cooling effect. Summarizing, advection acts to cool the surface of the ocean (upper 10 m), and in almost every case leads to warming at the sub-surface (10-100 m).

### Non-local mixing

TABLE 4.2: Differences (YELLOW-GREEN) in the heat budget components averaged over the Arctic, the Laptev Sea, and the Norwegian Sea. Values are calculated for two seasons, the local summer and winter (as defined in Table 4.1). Every component is integrated over the first 10 m and from 10 to 100 m.  $F_{\text{local}}$  refers to the local forcing term, and the unit is  $\text{W m}^{-2}$  everywhere.

Region	Depth	Season	$F_{\text{local}}$	Diffusion	Non-local	Advection	Total
Arctic	0-10 m	Jun to Sep	1.14	-1.15	0.03	-0.10	-0.07
Arctic	0-10 m	Nov to Feb	0.53	-0.48	-0.39	-0.01	-0.34
Arctic	10-100 m	Jun to Sep	-1.55	0.66	-0.01	0.03	-0.87
Arctic	10-100 m	Nov to Feb	0.18	0.36	0.01	-0.13	0.41
Norwegian Sea	0-10 m	May to Sep	2.60	-3.12	-0.16	0.00	-0.68
Norwegian Sea	0-10 m	Nov to Feb	-0.54	-2.51	-0.47	-0.01	-3.52
Norwegian Sea	10-100 m	May to Sep	-4.10	1.66	0.01	1.21	-1.21
Norwegian Sea	10-100 m	Nov to Feb	-0.57	1.92	-2.05	0.53	-0.17
Laptev Sea	0-10 m	Jul to Sep	3.02	-2.59	0.02	-0.32	0.12
Laptev Sea	0-10 m	Nov to Apr	0.36	-0.22	-0.13	-0.03	-0.02
Laptev Sea	10-100 m	Jul to Sep	-3.01	1.58	-0.02	0.74	-0.71
Laptev Sea	10-100 m	Nov to Apr	-0.01	0.25	0.13	0.07	0.44

This term accounts for the tendency due to non-local mixing, arising from the KPP vertical mixing parameterization (Eq. 2.21, non-local term). It represents unresolved eddy mixing within the ocean boundary layer that is independant of the local vertical temperature gradient. Thus, it acts to redistribute heat vertically when the mixed layer becomes deep enough, namely, in autumn and winter. Adding CDOM light absorption, leads to cooling close to the surface in autumn and winter. Conversely, non-local mixing tends to warm the ocean below 25 m from September to December (Fig. 4.13d, 4.14d). The effect of this term is more pronounced in the Norwegian Sea in autumn and winter (Fig. 4.14d). The wintertime non-local mixing effect there, is 3.6 times larger than the effect of the local forcing term at the sub-surface (Table 4.2). The Laptev Sea on the other hand, that is strongly stratified most of the year, is affected to a much lesser extent ( $-0.02 \text{ W m}^{-2}$  from 10-100 m in winter) by the contribution of non-local mixing (Fig. 4.15d).

## Summary

The conducted quantitative analysis revealed the individual heat budget component's warming or cooling effect and examined their relative contribution. It has been shown that changes in heating can be attributed to different heat budget terms, depending on the region and on the time of the year. The differences in the local forcing term and vertical diffusion account for a large part of the changes in the heat budget close to the surface, especially in summer. However, in the Atlantic sector, differences in the sub-surface heating can be largely determined by advective and non-local mixing processes in spring and winter. In the Norwegian Sea, the sub-surface indirect dynamical effect (advection & non-local mixing) in winter is 2.7 times larger than the effect of the local forcing (Table 4.2). Additionally, the Arctic shelf seas (e.g. Laptev Sea) are strongly affected by shortwave heating and vertical diffusion close to the surface during the sunlit season, and by advection in deeper layers, especially in summer (Table 4.2).

The findings of this analysis underline the potential of indirect changes in advective and mixing processes in intensifying or dumping (depending on the sign) the direct thermal effect of CDOM at the sub-surface. Finally, a look at the monthly mean standard errors of every heat budget component versus their magnitude reveals that the changes in the local forcing term are the most robust (Fig. A.1, Fig. A.2, Fig. A.3). On the other hand, the advection term exhibits the largest interannual variability, especially in the Norwegian Sea (Fig. A.2c).

## 4.5 Discussion and implications

The underwater light attenuation scheme based on interactive biogeochemistry (YELLOW) increases the simulated summertime SST compared to the CTRL run consistent with previous work (Manizza et al., 2005; Lengaigne et al., 2009). However, some of the results shown here, such as the increased annual mean SST, do not agree with previous reports of reduced annual SST due to interactive biogeochemistry (Mignot et al., 2013) or increased winter-only SST in the Arctic (Wetzel et al., 2006). One reason for this difference may be the plethora of reference simulations that make the

comparison among different studies difficult (Table 4.3). The assumptions used to parameterize light penetration in the different control runs vary from constant light attenuation depths of 11 m (Wetzel et al., 2006) to 25 m (Oschlies, 2004) to fixed chlorophyll concentrations (Lengaigne et al., 2009; Mignot et al., 2013) or a vertically varying chlorophyll climatology (Park et al., 2015; Lim, Kug, and Park, 2018). Whether positively or neutrally buoyant phytoplankton groups are included in the sensitivity run, also makes a difference in the vertical temperature distribution (Sonntag and Hense, 2011).

TABLE 4.3: Parameterizations used in studies examining the bio-optical effect of phytoplankton or CDOM. Z denotes the light attenuation depth ( $Z = 1/K_d$ ), IR the infrared radiation, and VIS the visible radiation. Additionally, R stands for red band, G for green, and B for blue band.

Study	Control run	Light partitioning	Visible light partitioning
Oschlies 2004	Z = 25 m	57% IR 43% VIS	-
Wetzel et al. 2006	Z = 11 m	50% IR 50% VIS	-
Patara et al. 2012	Z = 23 m	58% IR 42% VIS	-
Manizza et al. 2005	Z = 23 m	58% IR 42% VIS	-
Lengaigne et al. 2009	Fixed Chla (0.06 mg/m <sup>3</sup> )	unclear	1/3 R 1/3 G 1/3 B
Mignot et al. 2013	Fixed Chla (0.06 mg/m <sup>3</sup> )	unclear	1/3 R 1/3 G 1/3 B
Park et al. 2015	Chla climatology	unclear	-
Kim, Gnanadesikan, and Pradal 2016	Simulated Chla	58% IR 42% VIS	50% R 50% GB
Lim, Kug, and Park 2018	Chla climatology	58% IR 42% VIS	-

Previous modelling efforts focused on the effect of phytoplankton on ocean physics. The CDOM effect was either not considered or constant values of its absorption were used in the model's light attenuation scheme (Kim, Gnanadesikan, and Pradal, 2016; Kim et al., 2018b; Gnanadesikan, Kim, and Pradal, 2019). In a step forward, Kim et al. (2018b), by prescribing interannually-averaged absorption estimates from a satellite dataset, suggested that increased CDOM and suspended material may slow down the global warming effect on the ocean. Prescribed averages, however, necessarily neglect both the seasonality of CDOM and the feedback of modified SST and ocean circulation on CDOM distribution. Here, CDOM has a seasonal cycle and interacts with the thermal and dynamical changes induced by its presence. Note however, that additional terrigenous sources of CDOM and suspended material are not included in



the current model setup. Depending on the region (Stedmon et al., 2011) and the time of the year (Juhls et al., 2020), CDOM absorption may be underestimated locally by up to ten times, compared to measured values (Heim et al., 2014; Juhls et al., 2019; Soppa et al., 2019). By accounting for the loading of major Arctic rivers, the CDOM effect in the Arctic shelf seas is expected to be larger than shown here. Results suggest that, due to permafrost thawing and increasing river runoff, a future increase of this material will amplify the observed Arctic surface warming.

For an even better account of optical constituents in biogeochemical ocean models, the light attenuation coefficients should be wavelength dependent. CDOM absorbs light disproportionately in the ultraviolet and blue bands (Roesler and Perry, 1995), while phytoplankton absorption occurs mostly in the 400-500 and 650-700 nm which is further spectrally varying due to its composition and physiological state (Bricaud et al., 1995). To be able to account for these effects in the future, multispectral parameterization schemes are required that consider their inherent spectral optical properties (absorption and scattering) correctly. Instead, current model setups use monochromatic (Oschlies, 2004; Patara et al., 2012), 2-band (Manizza et al., 2005; Kim et al., 2018b), or 3-band approximations (Lengaigne et al., 2009) for the visible light. Besides light partitioning, multispectral data of solar radiation are necessary if their effects shall be incorporated into the optical modules (Dutkiewicz et al., 2015).

As shown in the previous section, depending on the region and the time of the year, indirect changes in advective and mixing processes can significantly affect the heat budget. To adequately represent the relevant dynamical processes, a horizontal resolution in the order of 1 km in the open ocean is required for the model to be eddy-resolving (Wekerle et al., 2017). However, close to the Arctic coasts, a resolution in the order of a few hundred meters would allow to take into account the details of the coastline and the bathymetry (Fofonova et al., 2015). Vertically, a realistic representation of the radiative effect of the water constituents will require a resolution in the order of 1 m close to the surface of the ocean (Terhaar et al., 2019).

Climate models tend to underestimate sea ice decline in the Arctic (Stroeve et al., 2012), while model uncertainty remains very large (Senffleben, Lauer, and Karpechko, 2020). By including the dynamic attenuation due to chlorophyll-a and CDOM, the ice-covered season in 2012 reduces by up to one month in parts of the Eastern Arctic.

Overall, the induced temperature and sea ice changes observed here, are of the same order of magnitude as changes due to different ocean model setups for the Arctic Ocean (Holloway et al., 2007; Johnson et al., 2007). With the conducted forced simulations, however, the atmospheric response to the modulated SST and sea ice distribution cannot be assessed. Phytoplankton-induced changes in SST may affect the thermal energy flux to the atmosphere (Jolliff et al., 2012) as well as the wind stress patterns (Jolliff and Smith, 2014), amplify the Earth’s greenhouse effect (Patara et al., 2012) and modify the atmospheric circulation (Wetzel et al., 2006; Patara et al., 2012). As a last remark, it should be mentioned that the induced thermal and dynamical changes feedback to the distribution of phytoplankton and CDOM. Modifications in marine phytoplankton will have an additional impact on polar climate, by altering biogenic gas emissions to the atmosphere (Kim et al., 2018a).

## 4.6 Conclusions

In this chapter, it is shown that incorporating the effect of phytoplankton and CDOM into the in-water shortwave radiation penetration scheme in Darwin-MITgcm, increases the SST in summer and decreases sea ice concentration in the Arctic Ocean. Furthermore, their combined effect amplifies the annual range of temperature and reduces the ice covered season in by up to one month in parts of the Eastern Arctic. The examination of the individual CDOM effect reveals that it drives a significant part of the observed changes. In summer, CDOM amplifies the surface warming and sea ice loss induced by phytoplankton and reduces the available heat at depth. Surface warming is accompanied by increased heat loss, primarily through the turbulent fluxes of sensible and latent heat. Overall, the annual mean SST is moderately increased in most of the Arctic and especially in the Nordic Seas.

Apart from its direct thermal effect, CDOM induces indirect dynamical changes too. Its effect can alter the vertical diffusion, advection, and non-local vertical mixing. Different parts of the Arctic Ocean, are characterized by different balances. Although differences in shortwave heating and vertical diffusion account for a large part of the Arctic-wide changes in the heat budget throughout the year, in the Atlantic sector,

differences in the sub-surface heating can be largely determined by advective and non-local mixing processes in spring and winter. In the Norwegian Sea, the sub-surface indirect dynamical effect (advection & non-local mixing) in winter is 2.7 times larger than the effect of the local forcing. Whereas the Arctic shelf seas are mostly affected by shortwave heating and vertical diffusion close to the surface during the sunlit season, and by advection in deeper layers.

The results and the implications discussed here suggest that the radiative effect of phytoplankton and CDOM is a significant source of model predictive uncertainty. However, the vast majority of modelling studies have either neglected both of them or investigated solely the effect of phytoplankton. So far, the CDOM effect has been examined only by constant values of its absorption, neglecting the feedback of modified temperature and ocean circulation on its concentration. The results here, emphasize the need for treating appropriately the phytoplankton and CDOM variability and their optical properties in Earth system modelling studies involving sea ice and temperature projections. Further research accounting for the interactions of phytoplankton and CDOM with all the Earth system components needs to be carried out to assess their feedback to a changing climate.



## Chapter 5

# Biogeochemical implications of light absorption by CDOM in the Arctic Ocean and the subarctic seas

### 5.1 Introduction

The two previous chapters have shed light on the role of phytoplankton, CDOM, and suspended material in modulating the vertical distribution of incoming solar energy and affecting the thermal structure of the upper ocean. As described in Chapter 4, light absorption by phytoplankton and CDOM in a general circulation model increases the summertime SST and reduces sea ice, while it amplifies the annual range of temperature. It is also shown that CDOM drives a significant part of these changes through its direct thermal effect, but also through indirect changes in the dynamics of the ocean.

The above findings prompted me to investigate the effect of light attenuation by CDOM on the Arctic Ocean's biogeochemical properties. Previous modelling effort accounting for the CDOM effect on biogeochemistry considered temporally constant values of its absorption (Kim, Pradal, and Gnanadesikan, 2015). Consequently, the feedback of modified temperature and ocean circulation on its concentration was necessarily neglected. This chapter examines the potential of the changes induced by CDOM, in altering the Arctic Ocean's photosynthetically available radiation (PAR) and major nutrient distributions, and thus, primary production and CDOM concentration. The investigation is conducted in the sense that a potential increase of phytoplankton and CDOM concentration at the surface will increase light absorption, and thus, ignite a secondary positive feedback mechanism on the Arctic climate.

## 5.2 Model nutrients evaluation

For the evaluation of the biogeochemistry of the current Darwin-MITgcm setup, the model's mean dissolved inorganic nitrogen (DIN), phosphate ( $\text{PO}_4$ ), and silicate ( $\text{SiO}_2$ ) are compared against the World Ocean Atlas 2018 (WOA, Garcia et al., 2018). Although there is a plethora of dissolved inorganic nutrient measurements in many parts of the global ocean, very sparse data can be found in most of the Arctic Ocean. Consequently, most parts of the central Arctic were heavily interpolated and, therefore, have been masked in the following figures of the WOA data.

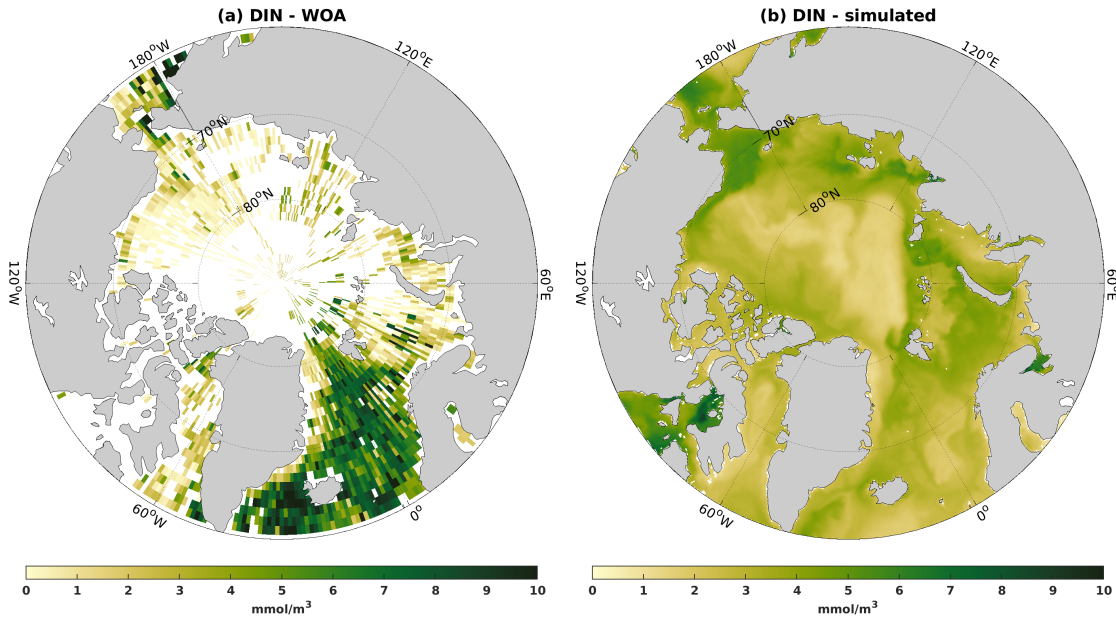


FIGURE 5.1: Mean upper 30 m dissolved inorganic nitrogen (DIN) concentration for: a) the World Ocean Atlas (WOA) 2018 (Garcia et al., 2018), b) the simulation YELLOW (2012-2014). Areas where no WOA measurements exist, have been masked (white) in panel (a).

Figure 5.1 shows the spatial distribution of the simulated DIN in the upper 30 meters of the ocean and the WOA-derived DIN for the same layer. In general, the model underestimates the concentration of DIN. The largest differences are observed in the Nordic Seas, where DIN is lower almost everywhere, compared to WOA. From Barents Sea to Chukchi, the simulated field (Fig. 5.1b) shows similar ranges to the

observations (Fig. 5.1a). The model captures the high near-surface DIN concentration in the Chukchi Sea, indicative of DIN supplied from the North Pacific Ocean. Additionally, it reproduces the decrease in DIN concentration in the Beaufort Sea and towards the central Arctic.

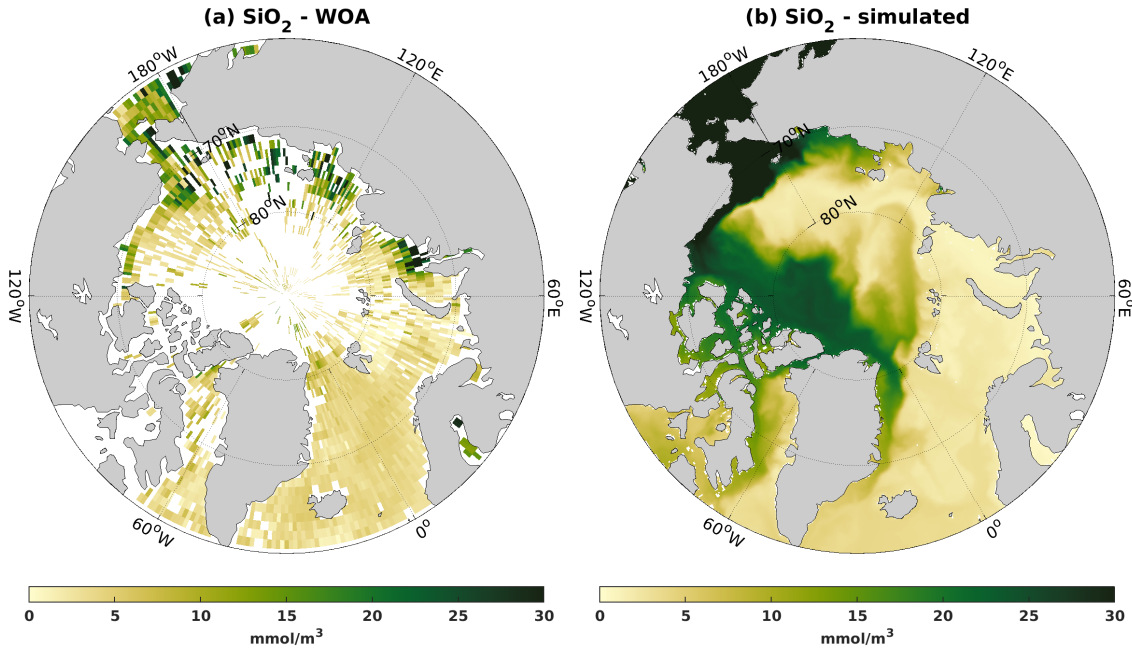


FIGURE 5.2: Same as Fig. 5.1, but for silicate ( $\text{SiO}_2$ ) concentration

Similarly to DIN, the WOA near-surface dissolved inorganic silicon field (Fig. 5.2a) exhibits high concentrations in the Chukchi Sea, but also across the Siberian coast. Silicon-rich water inflows from the North Pacific through the Bering Strait, while in the Siberian shelf Seas there is additional supply of Silicon from the rivers. The simulated silicate is characterized by elevated concentrations exceeding  $30 \text{ mmol m}^{-3}$  in the Chukchi Sea, the sub-polar North Pacific, and across the coast of the Beaufort Sea, in agreement with the observations (Fig. 5.2b). However, the model underestimates silicate close to the Siberian coast, due to the lack of riverine supply of nutrients in the current model setup. In the Canadian sector of the central Arctic, the high simulated silicate concentration cannot be thoroughly assessed, due to the extremely sparse observations in that region (Fig. 5.2a).

According to the observations, phosphate concentration is very high in Chukchi and Beaufort Sea, as well as in Baffin Bay and north of Greenland Sea (Fig. 5.3a).

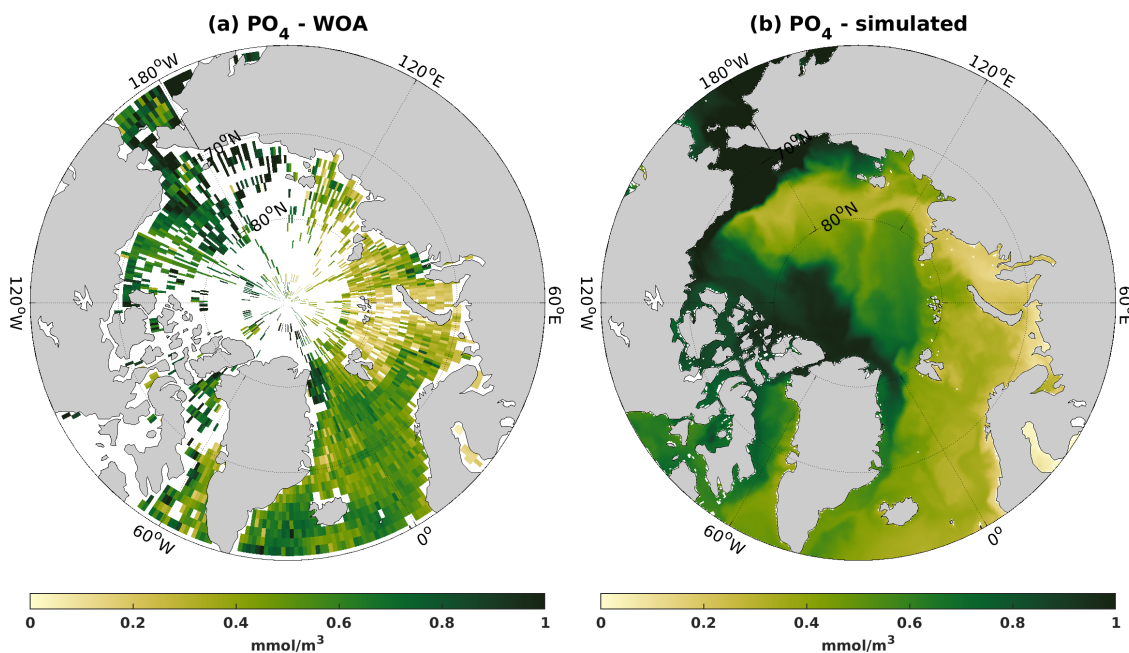


FIGURE 5.3: Same as Fig. 5.1, but for phosphate ( $\text{PO}_4$ ) concentration.

The simulated phosphate follows the observed spatial patterns and ranges in these regions. The model also captures to some extent the gradual decrease from the east Siberian shelf to Kara and Barents Sea (Fig. 5.3b). One explanation for the better model agreement of phosphate in the Siberian coast, compared to DIN and silicate, could be that the Arctic rivers are rich in DIN and silicate, but relatively poor in phosphate (Sakshaug, 2004). Consequently, the exclusion of riverine nutrient input wouldn't affect a lot the simulation of phosphate. Finally, phosphate is somewhat underestimated in the Atlantic sector, and mostly in the eastern part (e.g. Norwegian Sea).

## 5.3 Implications of light absorption by CDOM

### 5.3.1 Light, biomass, and nutrients

The thermal and dynamical effect of CDOM light absorption, described in the previous chapter, feeds back to the biomass of phytoplankton and the concentration of CDOM itself. In the simulation YELLOW, higher concentration of total chlorophyll-a



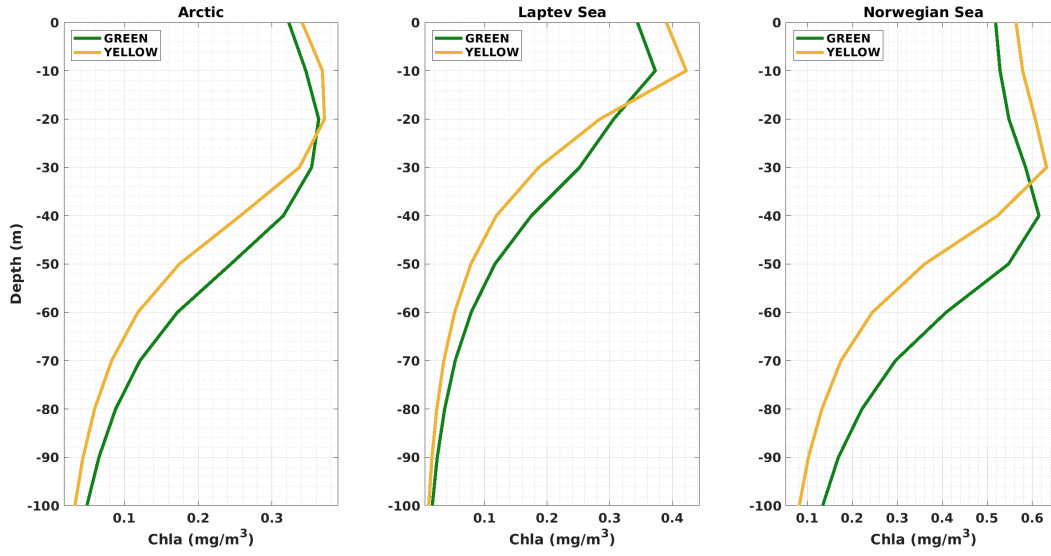


FIGURE 5.4: Annual mean differences of total chlorophyll-a concentration between YELLOW and GREEN for the upper 100 meters, over the 2007-2016 period for: the Arctic (**left panel**), the Laptev Sea (**middle panel**), and the Norwegian Sea (highlighted area of Figure 4.9) (**right panel**).

is observed close to the surface of the ocean. Through the simulated period (2007-2016), the total chlorophyll-a in the upper 20 meters increases on average by 6.1% in the Arctic, relative to the GREEN simulation (Fig. 5.4 left). On the contrary, at the sub-surface (20-100 m) it decreases by 22.3%, causing an overall decrease of 16.6% in the upper ocean (0-100 m). Similarly, in the Laptev Sea an increase of 13% is observed close to the surface (0-20 m) and a decrease of 22.3% from 20 to 100 m, and 16.6% in the upper 100 m (Fig. 5.4 middle). In the Norwegian Sea, increased total chlorophyll-a (9.2%) is observed over the upper 40 m, but a reduction of 35% from 40 to 100 m leads to an average decrease of 17.3% (Fig. 5.4 right). Depending on the region, the sub-surface chlorophyll-a maximum shifts by about 10 meters towards the surface (Fig. 5.4 left, right). This is not the case in Laptev Sea, a shallow stratified and light limiting shelf sea, where phytoplankton remains close to the surface (Fig. 5.4 middle).

Consistent with the observed annual mean changes in the total chlorophyll-a concentration, CDOM appears to change in a similar way in the upper 100 meters (Fig. 5.5). Over the same period, an increase is observed in the upper 40 to 60 m in all the examined regions (Arctic: 3.9% in the upper 50 m, Laptev Sea: 9.2% in the upper 40

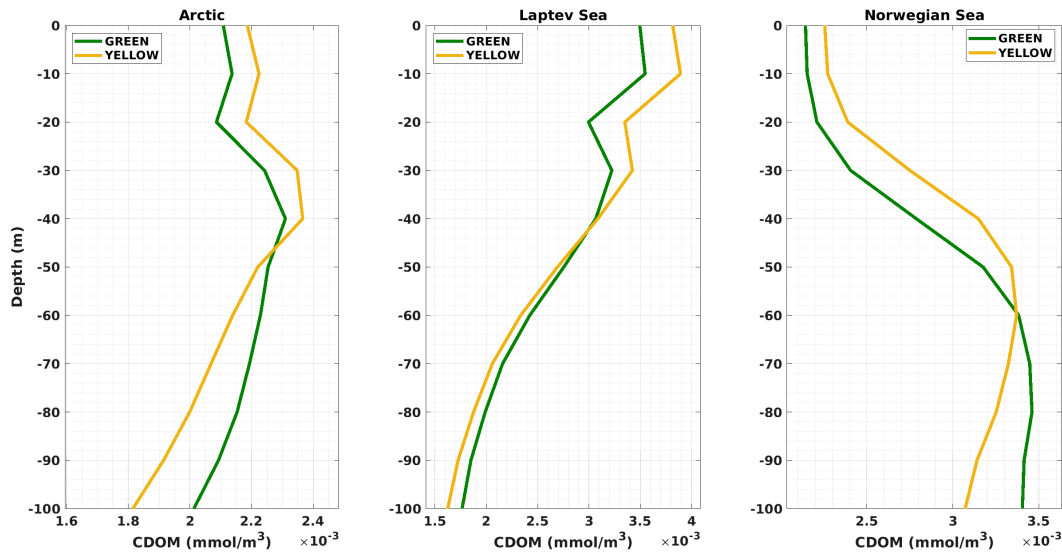


FIGURE 5.5: Annual mean differences of CDOM concentration between YELLOW and GREEN for the upper 100 meters, over the 2007-2016 period for: the Arctic (**left panel**), the Laptev Sea (**middle panel**), and the Norwegian Sea (**right panel**).

m, Norwegian Sea: 8.6% in the upper 60 m). On the contrary, CDOM in YELLOW is characterized by lower concentrations in the deeper ocean (Arctic: -5.4% over 50-100 m, Laptev Sea: -3.7% over 40-100 m, Norwegian Sea: -4.5% over 60-100 m), compared to the GREEN simulation.

Phytoplankton growth is controlled by light and nutrients availability, as well as grazing by zooplankton. However, the availability of light and nutrients is dependent on the physical processes taking place in the upper ocean. Changes in radiative heating, vertical mixing, advection, and sea ice cover, have the potential to affect significantly phytoplankton growth. For a better understanding on the CDOM-induced changes on the controlling mechanisms and their effect on phytoplankton, results from the Norwegian Sea are shown. This is a region previously described in Chapter 4, where some of the biggest changes (YELLOW-GREEN) both in physical and biogeochemical parameters are observed.

As described in the previous chapter (Section 4.4), the inclusion of CDOM absorption enhances light attenuation close to the surface. As a result, CDOM decreases

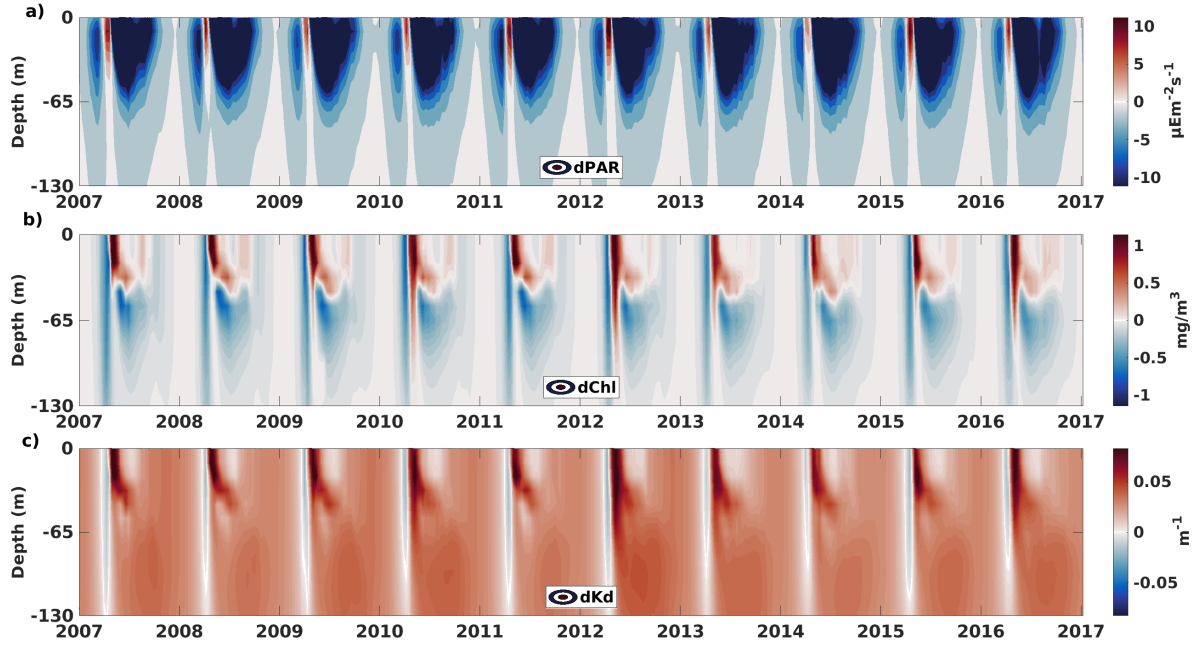


FIGURE 5.6: Mean differences in the Norwegian Sea (highlighted area of Figure 4.9) between YELLOW and GREEN for the upper 130 meters, in: a) photosynthetically available radiation (dPAR), b) total chlorophyll-a concentration (dChl), c) light attenuation coefficient (dKd, Eq. 1.11).

the photosynthetically available radiation (PAR) most of the year (Fig. 5.6a), meaning, it reduces the amount of light available for photosynthesis. The decreased light availability in early spring causes a reduction of total chlorophyll-a in the upper ocean (Fig. 5.6b). At the same time, the well-mixed ocean does not allow the phytoplankton to remain close to the surface, and subsequently to the euphotic zone. Directly after, increased PAR (Fig. 5.6a) owing to reduced chlorophyll-a absorption, as well as increased nutrient availability, trigger an increase of phytoplankton (Fig. 5.6b). Light attenuation rapidly increases again (Fig. 5.6c) due to the self-shading effect of phytoplankton, limiting the available radiation (Fig. 5.6a). However, during summer, there is ample solar radiation, and hence, only nutrients limit phytoplankton growth close to the surface. On the contrary, light is the limiting factor at the sub-surface. The (co-)limitation of light and nutrients confines phytoplankton growth in the upper 40 m, with a maximum increase between 25 and 40 m. This results in a decrease of total chlorophyll-a below 40 m in summer and autumn (Fig. 5.6b). Although there

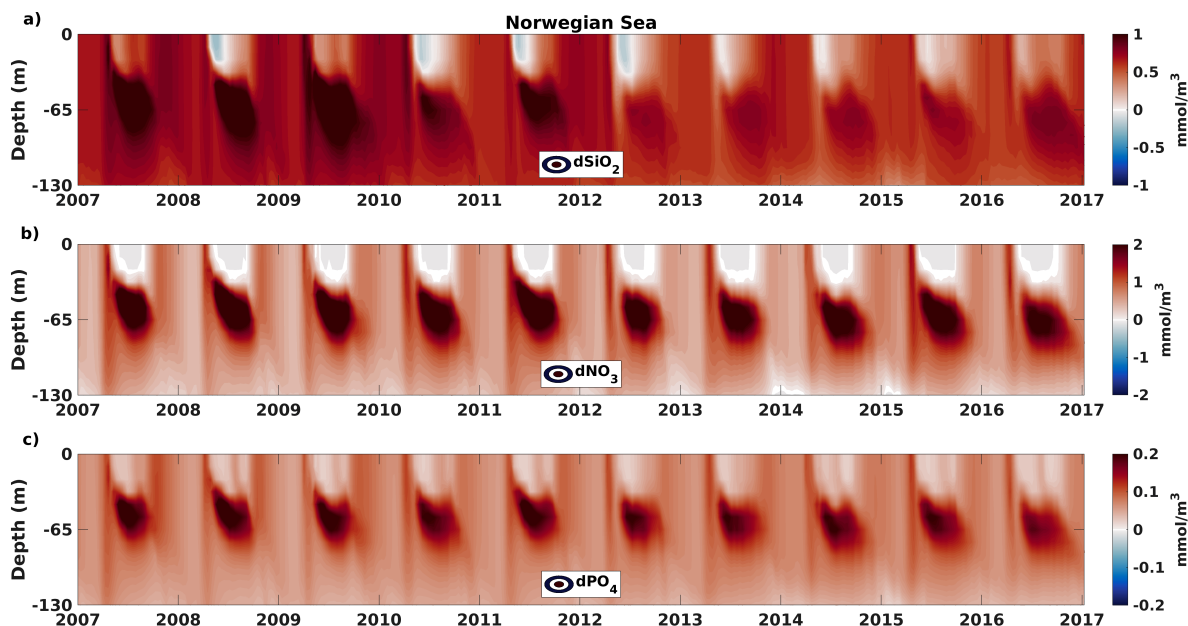


FIGURE 5.7: Mean differences in the Norwegian Sea between YELLOW and GREEN for the upper 130 meters, in: a) silicate ( $\text{dSiO}_2$ ), b) nitrate ( $\text{dNO}_3$ ), and c) phosphate ( $\text{dPO}_4$ ). Nitrate accounts for a large part of DIN.

is increased nutrient availability in this season (Fig. 5.7), the effectiveness of phytoplankton in utilising them is reduced.

Figure 5.7 shows the differences in the three major nutrients over the Norwegian Sea. The reduction of phytoplankton below 40 m leads to a higher concentration of DIN, silicate and phosphate at the sub-surface (Fig. 5.7a, b, c). In some years, silicate is slightly reduced at the surface during the spring bloom (Fig. 5.7a), indicating an increase in diatoms. On the other hand, DIN surface concentrations remain almost constant in summer (Fig. 5.7b). As will be discussed in the next section, this region is mostly Nitrogen-limiting during the sun-lit season. Consequently, DIN is the first nutrient to be depleted in both scenarios (GREEN and YELLOW). Furthermore, the increased vertical stratification inhibits nutrient replenishment within the mixed layer, driving the accumulation of them at the sub-surface (Fig. 5.7).

### 5.3.2 Phytoplankton growth limiting factors

Depending on the region and the time of the year, phytoplankton productivity can be limited by different factors. The Arctic Ocean is known to be mainly Nitrogen limiting during the summer months (Tremblay et al., 2015). On the other hand, photosynthesis is mainly restricted by light the rest of the year, due to very low solar elevations and the presence of sea ice. Phosphorus limitation is also likely in shelf waters affected by Arctic rivers, since they are rich in nitrate and silicate but relatively poor in phosphate (Sakshaug, 2004).

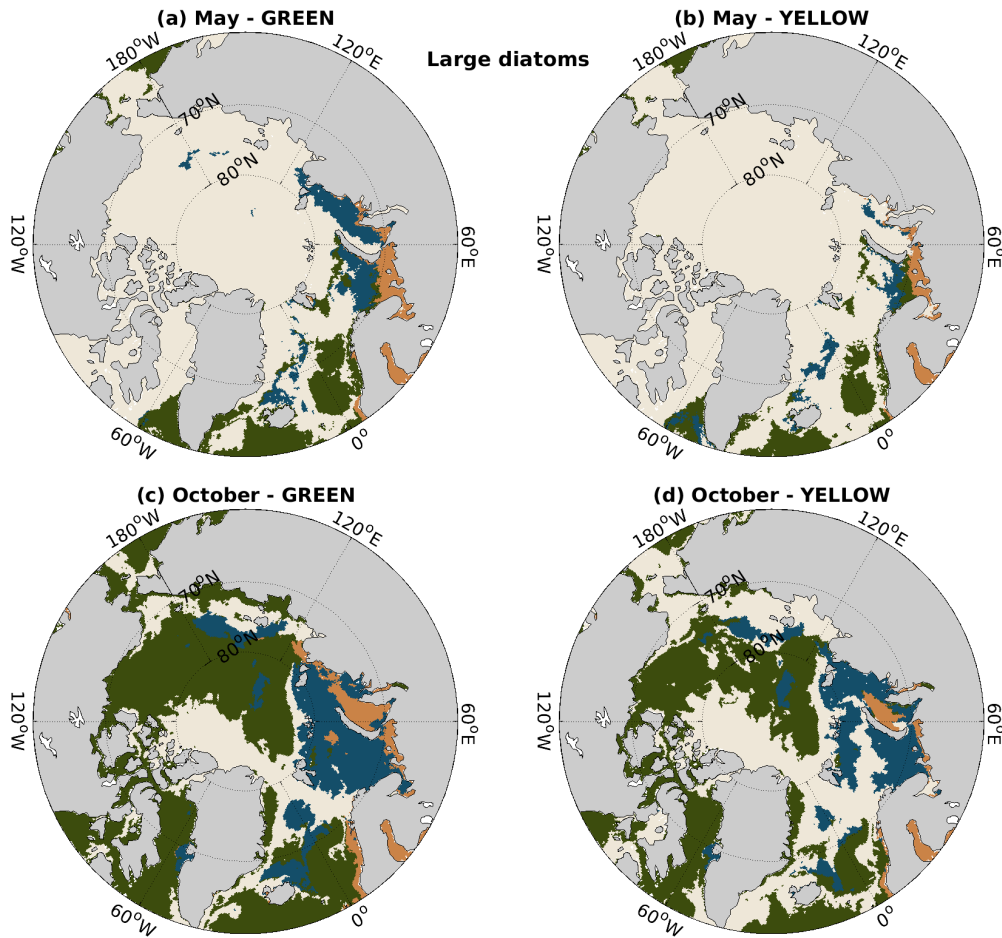


FIGURE 5.8: Spatial distribution of large diatoms growth limiting factors in the upper 20 m, for: a) May in the GREEN simulation, b) May in the YELLOW simulation, c) October in the GREEN simulation, and d) October in the YELLOW simulation. White colour denotes limitation due to light and temperature, green due to DIN, orange due to phosphate, and blue due to silicate.

As shown in the previous section, the consideration of CDOM in the model's light attenuation scheme, reduces in general the available radiation for photosynthesis and alters the major nutrients concentration. Due to the different affinities of the major phytoplankton functional types (PFTs) for nutrients and light (Table 2.2), their growth limitation is examined individually.

TABLE 5.1: Relative differences (YELLOW-GREEN) in the limiting area of every factor (light and other factors, DIN, PO<sub>4</sub>, SiO<sub>2</sub>) over the Arctic, for large and small diatoms, *Phaeocystis*, and coccolithophores. Values in every case are calculated for a specific month, one representing spring (May) and one accounting for late summer or early fall (September or October).

PFT	Light limitation	DIN limitation	PO <sub>4</sub> limitation	SiO <sub>2</sub> limitation
Large diatoms (May)	7.8%	-3.2%	-1.0%	-3.5%
Large diatoms (Oct)	18.3%	-11.7%	-2.7%	-3.9%
Small diatoms (May)	2.2%	-0.8%	-1%	-0.5%
Small diatoms (Sep)	21.9%	-13.4%	-7.1%	-1.4%
<i>Phaeocystis</i> (May)	4.0%	-3.0%	-1.0%	-
<i>Phaeocystis</i> (Sep)	14.3%	-7.6%	-6.8%	-
Coccolithophores (May)	4.0%	-3.0%	-1.0%	-
Coccolithophores (Sep)	16.4%	-9.8%	-6.6%	-

Fig 5.8 shows the factors limiting the growth of large diatoms during May and October; two months representative of the spring bloom in the Atlantic sector and the fall bloom in the eastern Arctic. In spring, light limits their growth in most of the Arctic and a part of the sub-polar regions (Fig. 5.8a). With the inclusion of CDOM absorption (YELLOW), springtime light limitation expands by 7.8% (Table 5.1), mainly in parts of Barents and Kara Sea, as well as in the Nordic Seas (Fig. 5.8b). As a result, silicate stops being limiting in Kara sea, and DIN in the rest of the regions where changes are observed. In late summer and the beginning of fall, increased light availability linked to the sea ice retreat, leads to expanded limitation primarily by DIN and silicate, and to a lesser extent by phosphate (Fig. 5.8c). However, this is a time of the year that CDOM exhibits very high concentrations (not shown). By accounting for its effect, the highest degree of the light limiting area expansion (18.3%) is observed during this season (Fig. 5.8d, Table 5.1). The most profound changes take place in the Barents Sea (15–55°E sector), where the light limiting area expands by 27%, mainly



in the cost of silicate limitation (-19.4%).

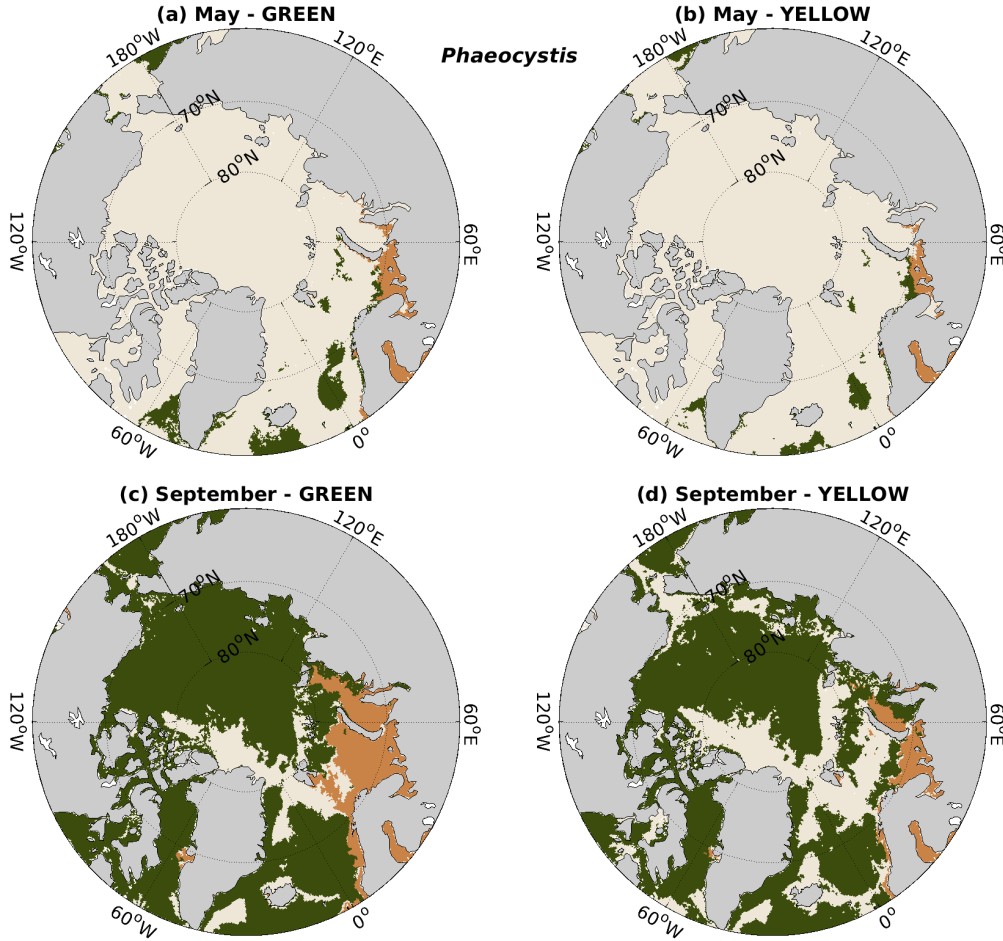


FIGURE 5.9: Same as Fig. 5.8, but for the *Phaeocystis* growth limiting factors (September has been considered for late summer - fall).

Similarly to large diatoms, *Phaeocystis* growth is mostly limited by light in May (Fig. 5.9a). However, as shown in Table 2.3, its growth is not dependent on silicate. Thus, the remaining two (co-)limiting factors are DIN and phosphate. These two nutrients limit *Phaeocystis* growth in a very limited area of sub-polar North Atlantic and in the coastal Barents Sea. Consequently, the CDOM effect in this season is restricted in these regions by slightly expanding the light limitation area (4%) at the expense of nutrients (Fig. 5.9b, Table 5.1). On the contrary, in late summer DIN is the primary limiting factor in the Arctic Ocean. Limitation due to phosphate extends from the Norwegian coast in the North Atlantic to Kara Sea (Fig. 5.9c). In YELLOW, a similar to Fig. 5.8d expansion of the light limiting area is observed (Fig. 5.9d).

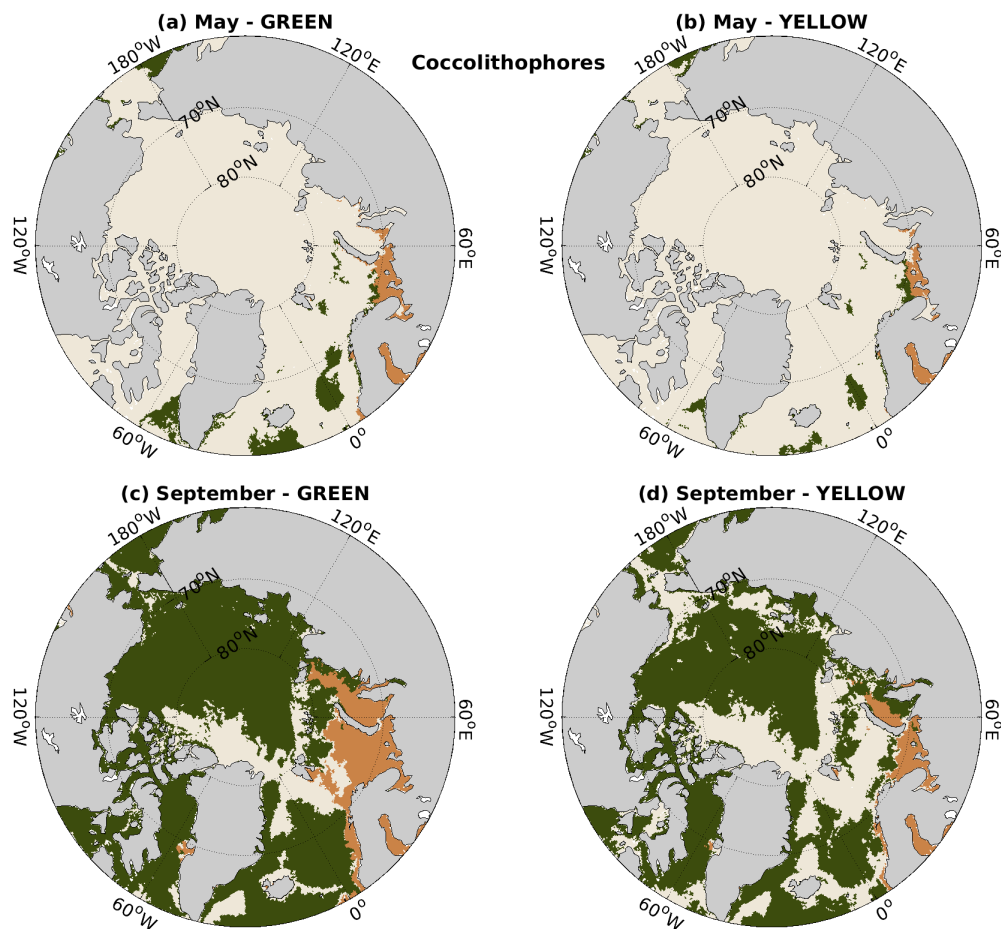


FIGURE 5.10: Same as Fig. 5.8, but for the coccolithophores growth limiting factors (September has been considered for late summer - fall).

As with large diatoms, the largest differences are observed in the Barents Sea, where light limitation expands by 32.2%, while the phosphate limiting area shrinks by 48.6%.

The last major PFT examined here, is coccolithophores (Fig. 5.10), whose growth limitation exhibits very similar behaviour to *Phaeocystis* (Fig. 5.9, Table 5.1). There is barely any difference in May between the simulations GREEN and YELLOW, since light limitation dominates (Fig. 5.10a, b). In late summer, DIN limits the growth of coccolithophores except for the area around the Barents Sea, described in the previous paragraph (Fig. 5.10c). The CDOM effect expands light limitation (16.4%) almost the same way as for *Phaeocystis* (Fig. 5.10d). There are, however, some minor differences indicating that nutrients become less limiting for coccolithophores (Fig. 5.9d, Fig. 5.10d, Table 5.1). In Barents Sea, light limitation expands slightly more (35.2%) compared to *Phaeocystis* (32.2%). It should be also noted that in fall, the light becomes



limiting earlier for *Phaeocystis* and coccolithophores (September), compared to large diatoms (October). This time lag arises from the different sensitivities to light that those PFTs have within the Darwin model.

As a final remark, it should be kept in mind that the near-surface changes observed in the phytoplankton growth limiting factors are the result of two effects: the direct effect of CDOM on reducing light availability (Fig. 5.6a) and the indirect effect on increasing nutrient supply (Fig. 5.7) due to reduced productivity at the sub-surface (Fig. 5.6b).

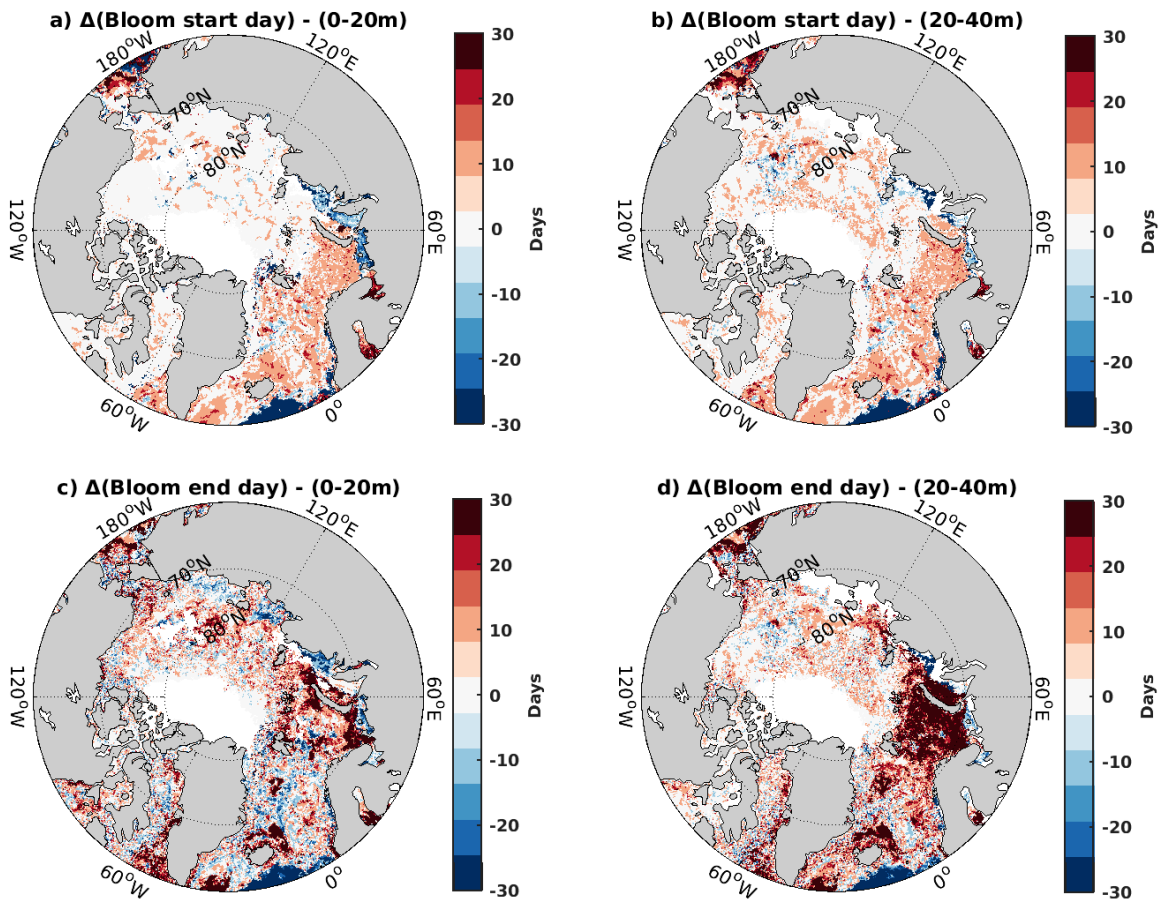


FIGURE 5.11: Spatial distribution of differences (YELLOW-GREEN) in diatoms (large and small) phenology, in 2012: a) bloom start day at the surface (0-20m), b) bloom start day at the sub-surface (20-40m), c) bloom end day at the surface (0-20m), d) bloom end day at the sub-surface (20-40m).

### 5.3.3 Phytoplankton phenology

The term phenology refers to the timing of events during the seasonal cycle; in this case to the onset of the phytoplankton spring bloom and its end in late summer and fall (Fig. A.4, A.5). Figure 5.11 presents the spatial patterns of differences (YELLOW-GREEN) in the diatom (large and small) phenological indices (Section 2.2.7), in 2012. It can be seen that light attenuation due to CDOM leads to a short delay of the onset of the spring bloom (5 days) in the Atlantic sector (Fig. 5.11a, b), both at the surface and at the sub-surface. As discussed in Section 5.3.1, the ocean is well mixed in spring in the sub-polar North Atlantic. As a result, the response of phytoplankton on CDOM effect is almost the same in the entire upper ocean.

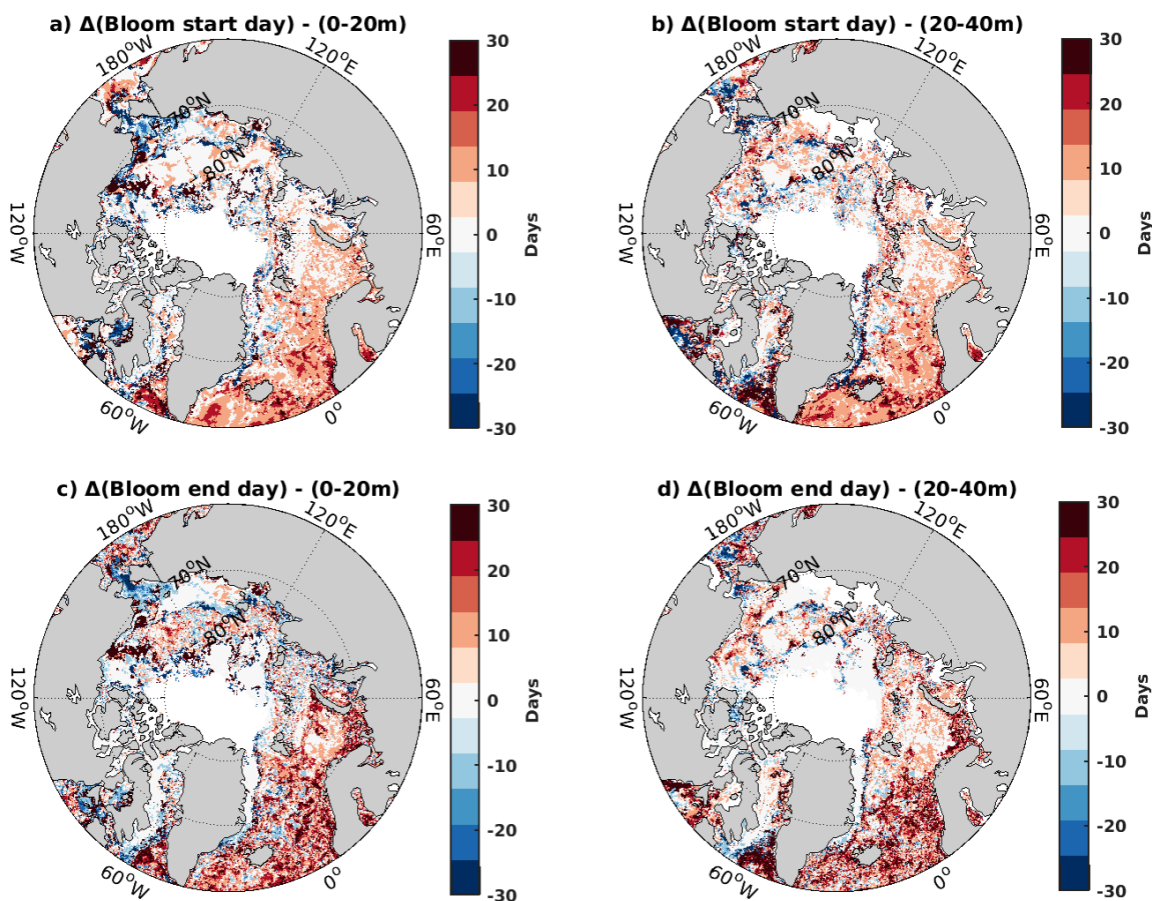


FIGURE 5.12: Same as in Fig. 5.11, but for the haptophytes (coccolithophores and *Phaeocystis*) phenology.

In late summer and early fall, a delay of the end of the diatom bloom (4 days) at the surface is observed in most regions (Fig. 5.11c, d). However, in contrast to

spring, the response of diatoms from 20 to 40 m is stronger (8.6 days), while it may be locally decoupled from their response at the surface (e.g. Greenland Sea). The end of the diatom bloom at the sub-surface is shifted by up to 1 month, especially at the Barents Sea (29 days). Although most of the surface waters of the Barents Sea are characterized by later bloom ending too, the delay in the upper 20 m is shorter (10 days, Fig. 5.11c). Moreover, in some parts of the Greenland Sea and the Siberian coast, the bloom ends earlier at the surface. A possible explanation is that in fall (Fig. A.4c), the Siberian shelf seas are characterized by very high CDOM concentrations, and thus they become much more light limiting than other regions (Fig 5.8c, d). In the Kara Sea, there is also the case that in autumn it becomes more silicate limiting (Fig 5.8c, d) affecting the growth of diatoms. The changes in the timing of the bloom are reflected in its duration. The bloom lasts on average 3 days and 1 week longer at the surface and the sub-surface, respectively. Locally, the changes can be in the order of 24 days (Barents Sea, not shown).

Similarly to diatoms, the bloom of haptophytes (*Phaeocystis* and coccolithophores) at the surface begins on average 2.6 days later, except for the Chukchi Sea (Fig. 5.12a, b). The bloom onset season in the Chukchi Sea (September, Fig. A.5a, b) coincides with the beginning of light limitation due to CDOM absorption (Fig 5.9c, d and 5.10c, d). CDOM appears to affect the bloom ending in a similar way as with diatoms, with a delay of the order of 12 days (Fig 5.12c, d) in the upper 40 meters. One difference, however, is that the decoupling between surface and sub-surface occurs in parts of the eastern Arctic, instead of the Nordic Seas (Fig 5.12c, d). In contrast to diatoms (24 days), the sub-surface bloom duration in most of the Barents Sea barely changes.

## 5.4 Conclusions

This chapter addressed the effect of CDOM light absorption on the Arctic Ocean's and the subarctic seas biogeochemistry. In a step forward, by accounting for CDOM as a prognostic model variable that feeds back to the physics, its potential in altering light availability, nutrient supply, primary production, and CDOM concentration, was examined. It has been shown that the effect of CDOM feeds back to phytoplankton and CDOM itself leading to higher annual mean concentrations of total chlorophyll-a and

CDOM close to the surface, and to lower concentrations at the sub-surface. In spring, reduced light availability causes a phytoplankton bloom delay and, thus, an increase in nutrient concentrations. Subsequently, the excess of nutrients under the late spring well-lit conditions triggers a biomass increase. In late summer, the (co-)limitation of light and nutrients confines phytoplankton growth in a few tens of meters from the ocean surface. A delay of the end of the bloom is observed accordingly, especially at the sub-surface waters of the Barents Sea (29 days for diatoms). These findings indicate that a future increase of CDOM will ignite a secondary positive feedback mechanism on the Arctic climate through increased phytoplankton and CDOM light absorption close to the surface.

Under the effect of CDOM, springtime light limitation for the major phytoplankton groups slightly expands to parts of Barents and Kara Sea, as well as to the Nordic Seas. The most of the light limiting area expansion is observed in the beginning of fall, at the expense of reduced silicate and DIN limitation for diatoms, and at the expense of reduced DIN and phosphate limitation for *Phaeocystis* and coccolithophores. The most profound changes take place in the Barents Sea where light limitation expands by 27%-35.2%, depending on the PFT. Considering the different affinities of the phytoplankton groups on light and nutrients, the changes in the growth limiting factors suggest also a shift in the phytoplankton community structure. The latter would be an interesting topic for future research.

## Chapter 6

# Conclusions and outlook

### 6.1 Main outcomes

The research questions raised in the introduction can now be addressed with the insights from the three previous chapters.

- Q1: What is the role of CDOM and total suspended matter in the radiative heating in the shelf waters of the Laptev Sea?

This research question was addressed in Chapter 3, by means of radiative transfer modelling, satellite remote sensing, and *in situ* observations. The Laptev Sea region is heavily influenced by the Lena River, one of the largest river systems in the Arctic. By using the coupled atmosphere-ocean radiative transfer model SCIATRAN, I simulated locally the radiative effect of CDOM, TSM, and phytoplankton, based on the provided *in situ* data. The results showed that the radiative heating of Laptev Sea surface waters was strongly influenced by the concentration of CDOM and TSM. The presence of these optically active constituents led to enhanced energy absorption in the upper 2 m of the ocean. Likewise, locations with a higher amount of CDOM / TSM exhibited increased sea ice melt rates compared to clearer waters, and larger differences in the ocean-atmosphere heat flux.

As a next step, I provided satellite remote sensing retrievals of CDOM, TSM, chlorophyll-a, and SST as input to the radiative transfer model simulations. Thereby, it was possible for the first time to quantify the spatial distribution of the radiative heating in the Laptev Sea for a typical summer day. The spatial

patterns of absorbed energy and radiative heating closely followed the distribution of the optically active water constituents. The highest energy absorption occurred over river-influenced waters confirming the significant influence of these constituents on the radiative heating of the Laptev Sea surface waters. These findings lend support to the claim that the presence of optically active water constituents in the Arctic can potentially strengthen the effect of Arctic Amplification due to the known positive feedback mechanisms among surface water temperature, sea ice melt, precipitation, and river runoff. Furthermore, they indicated that the lack of *in situ* measurements can be compensated to some extent by satellite retrievals in synergy with radiative transfer modelling. This is particularly valuable for remote and inaccessible Arctic regions. In conclusion, the results indicated that solar radiation absorption by water constituents is an important aspect to be considered in general circulation models as it affects radiative heating, sea ice melting, and heat exchange between the ocean and the atmosphere. A detailed and realistic representation of the optical properties of CDOM and TSM is particularly important to accurately model coastal waters and shelf seas highly influenced by rivers.

- Q2: How does the light attenuation by phytoplankton and CDOM contribute to the radiative heating and sea ice reduction in the Arctic Mediterranean Sea?

In Chapter 4, I upscaled the previous one-dimensional and regional Laptev Sea study utilizing 3D general circulation modelling for the entire Arctic Mediterranean Sea and the subarctic seas. By operating an ocean biogeochemical model coupled to a general circulation model with sea ice (Darwin-MITgcm), the effect of phytoplankton and CDOM was incorporated into the in-water shortwave radiation penetration scheme. This interactive parameterization was used to examine how the light attenuation by phytoplankton and CDOM contributes to surface warming and sea ice loss in the Arctic Ocean and the subarctic seas. When both effects were turned on, the summer surface temperatures were higher, causing more sea ice melting. Over the 2007-2016 period, the mean SST of the warmest climatological month (July) increased by 0.3°C. Consequently, the sea ice season was reduced by up to one month in some parts of the Eastern Arctic.

Increased heat losses to the atmosphere led to lower SSTs in winter, and subsequently, to an amplified seasonal cycle of surface temperature. Nevertheless, it has been discussed that the results obtained, are subject to the assumptions used to parameterize light penetration in the control run. For that, it was shown that the plethora of reference simulations used, makes the comparison between relevant studies difficult.

The examination of the individual effect of CDOM revealed that it drives a significant part of the observed changes. In summer, CDOM amplified the surface warming and sea ice loss induced by phytoplankton and reduced the available heat at depth. From June to September of 2012, 48% of the observed changes in surface temperature over the Arctic were attributed to the effect of CDOM. This warming at the surface was accompanied by increased heat loss, primarily through sensible and latent heat flux. However, two distinct cases were identified. Although the summertime heat loss in the Norwegian Sea was  $2.4 \text{ W/m}^2$ , the reduced sea ice in the Laptev Sea promoted the penetration of shortwave radiation, counterbalancing any temperature-induced losses there. Apart from its direct thermal effect, CDOM induced indirect changes too. Its effect altered the vertical diffusion, advection, and non-local vertical mixing. Different parts of the Arctic Mediterranean Sea, are characterized by different balances. Although differences in shortwave heating and vertical diffusion accounted for a large part of the Arctic-wide changes in the heat budget throughout the year, in the Atlantic sector, differences in the sub-surface heating were largely determined by advective and non-local mixing processes in spring and winter. In the Norwegian Sea, the sub-surface indirect dynamical effect (advection & non-local mixing) in winter was 2.7 times larger than the effect of shortwave heating. Whereas the Arctic shelf seas were mostly affected by shortwave heating and vertical diffusion close to the surface during the sunlit season, and by advection in deeper layers.

The findings of this thesis give support to the claim that a future increase of CDOM, owing to increased permafrost thawing and river runoff, will amplify the observed Arctic surface warming. They also suggest that the radiative effect of phytoplankton and CDOM is a significant source of predictive uncertainty in ocean and climate models. The modelling community has either neglected both



of them, investigated solely the effect of phytoplankton, or considered prescribed values of CDOM absorption. The presented results, underline the need to treat appropriately the variability and the optical properties of phytoplankton and CDOM in future modelling studies, to enhance their plausibility.

- Q3: How do changes in light attenuation due to CDOM affect biogeochemistry and the ecosystem?

The results corresponding to the two previous research questions prompted me to further investigate the CDOM effect on the Arctic Mediterranean Sea's biogeochemistry and ecosystem (Chapter 5). So far, modelling effort in investigating the effect of CDOM on the physics, and subsequently, on the biogeochemistry of the ocean had considered temporally and vertically constant values of its light absorption. Hence, the feedback of modified temperature and ocean circulation on phytoplankton and CDOM concentration was necessarily neglected. This thesis examined the potential of CDOM, as a prognostic model variable, in altering light availability and nutrient supply, and thus primary production and CDOM concentration.

The effect of CDOM feeds back to phytoplankton biomass and the concentration of CDOM itself. Accounting for CDOM light absorption led to higher annual mean concentrations of total chlorophyll-a and CDOM close to the surface of the ocean. Over the Arctic, their near-surface concentrations increased by 6.1% and 3.9% respectively, while in regions like the Laptev Sea the total chlorophyll-a increase was of the order of 13%. On the contrary, reduced concentrations were observed at the sub-surface resulting in a 16.6% overall biomass decrease in the upper ocean (0-100m). CDOM decreased the available radiation for photosynthesis most of the year. In spring, reduced light availability under well-mixed ocean conditions did not allow the phytoplankton to remain in the euphotic zone causing a bloom delay. Shortly after, an excess of nutrients under well-lit conditions triggered a biomass increase. In late summer, the (co-)limitation of light and nutrients confined phytoplankton growth in a few tens of meters from the ocean surface. Correspondingly, a delay of the end of the bloom was observed,



especially at the Barents Sea (29 days for diatoms, 20-40 m). These findings indicate that a future increase of CDOM will ignite a secondary positive feedback mechanism on the Arctic climate, through increased phytoplankton and CDOM light absorption close to the surface.

Under the effect of CDOM, springtime light limitation for the major phytoplankton groups slightly expanded to parts of Barents and Kara Sea, as well as to the Nordic Seas. The highest degree of expansion of the light limiting areas was observed at the beginning of fall. This expansion happened at the cost of silicate and DIN limitation for diatoms, and DIN and phosphate limitation for *Phaeocystis* and coccolithophores. The most profound changes took place in the Barents Sea, where light limitation expanded by 27%-35.2%, depending on the PFT. Considering the different affinities of the phytoplankton groups on light and nutrients, the changes in the growth limiting factors suggest a shift in the phytoplankton community structure. Since this aspect of the CDOM effect is beyond the scope of this thesis, it would be an interesting topic for future research.

## 6.2 Outlook

Based on the results and limitations of this study, several aspects to be considered in future research, are identified.

For an even better representation of optically active constituents in numerical models, the light attenuation coefficients need to be wavelength dependent. Future studies should consider that CDOM absorbs light disproportionately in the ultraviolet and blue bands, while phytoplankton absorption occurs mostly in the 400-500 and 650-700 nm. Phytoplankton absorption is further spectrally varying because of its composition and physiological state. Apart from light absorption, phytoplankton and suspended material also scatter light in a way that differs by wavelength. To rigorously calculate these effects, multispectral parameterization schemes that consider these inherent spectral optical properties correctly, are required. The choice of parameterization and

the inclusion of spectrally-resolved irradiance may significantly affect the ocean biogeochemistry and the phytoplankton community structure (Dutkiewicz et al., 2015; Gregg and Rousseaux, 2016). Besides light partitioning, a scheme like this would also require multispectral data of solar radiation as input.

As a further step to better assess the CDOM effect in the Arctic Ocean, the terrigenous sources of CDOM and suspended material need to be included in future model setups. Depending on the time of the year, the exclusion of terrigenous CDOM in the Arctic shelf seas may lead to an underestimation up to an order of ten times, close to the river deltas. Additionally, the spectral dependency based on the composition of CDOM (e.g. terrestrial versus marine sources) needs to be represented. By accounting for the loading of major Arctic rivers, its effect on the Arctic shelf regions is expected to be larger than shown in this study.

Another aspect to be considered is the horizontal and vertical resolution of the general circulation model. To allow the model to be eddy-resolving, a horizontal resolution of the order of 1 km in the open ocean is required (Wekerle et al., 2017). However, close to the Arctic coasts, a resolution of the order of a few hundred meters would allow to take into account the details of the coastline and the bathymetry (Fofonova et al., 2015). A realistic representation of the radiative effect of the water constituents will also require a vertical resolution of the order of 1m close to the surface of the ocean (Terhaar et al., 2019).

Hopefully, in the future, a model setup that satisfies the aforementioned requirements will allow a more thorough investigation of the effect of phytoplankton and CDOM on the Arctic climate.

# Bibliography

- Ardyna, Mathieu et al. (2014). “Recent Arctic Ocean sea ice loss triggers novel fall phytoplankton blooms”. In: *Geophysical Research Letters* 41.17, pp. 6207–6212. DOI: <https://doi.org/10.1002/2014GL061047>.
- Bailey, Sean W and P Jeremy Werdell (2006). “A multi-sensor approach for the on-orbit validation of ocean color satellite data products”. In: *Remote Sensing of Environment* 102.1, pp. 12–23.
- Bauch, D. and E. Cherniavskaia (2018). “Water Mass Classification on a Highly Variable Arctic Shelf Region: Origin of Laptev Sea Water Masses and Implications for the Nutrient Budget”. In: *Journal of Geophysical Research: Oceans* 123.3, pp. 1896–1906. DOI: <https://doi.org/10.1002/2017JC013524>.
- Bintanja, R. and O. Andry (2017). “Towards a rain-dominated Arctic”. In: *Nature Climate Change* 7, pp. 263–267. DOI: [10.1038/nclimate3240](https://doi.org/10.1038/nclimate3240).
- Bintanja, R and F. M. Selten (2014). “Future increases in Arctic precipitation linked to local evaporation and sea-ice retreat”. In: *Nature* 509.7501, pp. 479–482. DOI: [10.1038/nature13259](https://doi.org/10.1038/nature13259).
- Blum, M et al. (2012). “Coupled ocean-atmosphere radiative transfer model in the framework of software package SCIATRAN: Selected comparisons to model and satellite data”. In: *Advances in Space Research* 49.12, pp. 1728–1742.
- Bricaud, A., A.-L. Bédhomme, and A. Morel (1988). “Optical properties of diverse phytoplanktonic species: experimental results and theoretical interpretation”. In: *Journal of Plankton Research* 10.5, pp. 851–873. DOI: [10.1093/plankt/10.5.851](https://doi.org/10.1093/plankt/10.5.851).
- Bricaud, A. et al. (1995). “Variability in chlorophyll-specific absorption coefficients of natural phytoplankton: Analysis and parameterization”. In: *Journal of Geophysical Research* 100.7, pp. 13321–13332. DOI: <https://doi.org/10.1029/95JC00463>.
- Bricaud, Annick et al. (2004). “Natural variability of phytoplanktonic absorption in oceanic waters: Influence of the size structure of algal populations”. In: *Journal of Geophysical Research: Oceans* 109, p. C11010. DOI: <https://doi.org/10.1029/2004JC002419>.

- Brockmann, Carsten et al. (2016). “Evolution of the C2RCC neural network for Sentinel 2 and 3 for the retrieval of ocean colour products in normal and extreme optically complex waters”. In: *Living Planet Symposium*. Vol. 740, p. 54.
- Buiteveld, H., J.H.M. Hakvoort, and M. Donze (1994). “The optical properties of pure water”. In: *SPIE 2258, Ocean Optics XII*, pp. 174–183. URL: <https://www.spiedigitallibrary.org/conference-proceedings-of-spie/2258/0000/Optical-properties-of-pure-water/10.1117/12.190060.short?SS0=1>.
- Cahill B., Schofield O et al. (2008). “Dynamics of turbid buoyant plumes and the feedbacks on near-shore biogeochemistry and physics”. In: *Geophysical Research Letters* 35, p. L10605. DOI: [10.1029/2008GL033595](https://doi.org/10.1029/2008GL033595).
- Clayton, S. et al. (2017). “Biogeochemical versus ecological consequences of modeled ocean physics”. In: *Biogeosciences* 14.11, pp. 2877–2889.
- Coble, Paula G. (2007). “Marine Optical Biogeochemistry: The Chemistry of Ocean Color”. In: *Chemical Reviews* 107.2, pp. 402–418. DOI: <https://doi.org/10.1021/cr050350+>.
- Daru, V. and C. Tenaud (2004). “High order one-step monotonicity-preserving schemes for unsteady compressible flow calculations”. In: *Journal of Computational Physics* 193.2, pp. 563–594. DOI: <https://doi.org/10.1016/j.jcp.2003.08.023>.
- Dmitrenko, Igor et al. (2005). “Wind-driven summer surface hydrography of the eastern Siberian shelf”. In: *Geophysical Research Letters* 32.14. DOI: <https://doi.org/10.1029/2005GL023022>.
- Dutkiewicz, S. et al. (2015). “Capturing optically important constituents and properties in a marine biogeochemical and ecosystem model”. In: *Biogeosciences* 12, pp. 4447–4481. DOI: [10.5194/bg-12-4447-2015](https://doi.org/10.5194/bg-12-4447-2015).
- Field, Christopher B. et al. (1998). “Primary Production of the Biosphere: Integrating Terrestrial and Oceanic Components”. In: *Science* 281.5374, pp. 237–240. DOI: [10.1126/science.281.5374.237](https://doi.org/10.1126/science.281.5374.237).
- Fofonova, V. et al. (2015). “Impact of wind and tides on the Lena River freshwater plume dynamics in the summer season”. In: *Ocean Dynamics* 65, 951–968. DOI: <https://doi.org/10.1007/s10236-015-0847-5>.
- Frey, Karen E. and Laurence C. Smith (2005). “Amplified carbon release from vast West Siberian peatlands by 2100”. In: *Geophysical Research Letters* 32.9, p. L09401. DOI: <https://doi.org/10.1029/2004GL022025>.

- Garcia, H. E. et al. (2018). “World Ocean Atlas 2018, Volume 4: Dissolved Inorganic Nutrients (phosphate, nitrate and nitrate+nitrite, silicate). A. Mishonov Technical Editor”. In: *NOAA Atlas NESDIS* 84, 35pp.
- Gnanadesikan, Anand, Grace E. Kim, and Marie-Aude Pradal (2019). “Impact of Colored Dissolved Materials on the Annual Cycle of Sea Surface Temperature: Potential Implications for Extreme Ocean Temperatures”. In: *Geophysical Research Letters* 46, pp. 961–869. DOI: <https://doi.org/10.1029/2018GL080695>.
- Gohin, F., J.N. Druon, and L. Lampert (2002). “A five channel chlorophyll concentration algorithm applied to SeaWiFS data processed by SeaDAS in coastal waters”. In: *International Journal of Remote Sensing* 23, pp. 1639–1661. DOI: [10.1080/01431160110071879](https://doi.org/10.1080/01431160110071879).
- Gonçalves-Araujo, Rafael et al. (2018). “High colored dissolved organic matter (CDOM) absorption in surface waters of the central-eastern Arctic Ocean: Implications for biogeochemistry and ocean color algorithms”. In: *PloS one* 13.1, e0190838.
- Granskog, Mats A et al. (2015). “Effect of sea-ice melt on inherent optical properties and vertical distribution of solar radiant heating in Arctic surface waters”. In: *Journal of Geophysical Research: Oceans* 120.10, pp. 7028–7039.
- Gregg, Watson W. and Cécile S. Rousseaux (2016). “Directional and Spectral Irradiance in Ocean Models: Effects on Simulated Global Phytoplankton, Nutrients, and Primary Production”. In: *Frontiers in Marine Science* 3, p. 240. DOI: [10.3389/fmars.2016.00240](https://doi.org/10.3389/fmars.2016.00240).
- Groeskamp, S. and D. Iudicone (2018). “The Effect of Air-Sea Flux Products, Short-wave Radiation Depth Penetration, and Albedo on the Upper Ocean Overturning Circulation”. In: *Geophysical Research Letters* 45, pp. 9087–9097. DOI: [10.1029/2018GL078442](https://doi.org/10.1029/2018GL078442).
- Grosse, G. et al. (2016). “Changing permafrost in a warming world and feedbacks to the Earth system”. In: *Environmental Research Letters* 11.4, p. 040201. DOI: [10.1088/1748-9326/11/4/040201](https://doi.org/10.1088/1748-9326/11/4/040201).
- Haltrin, V. I. (1999). “Small-Parametric Model of the Optical Properties of Seawater”. In: *Applied Optics* 38, pp. 6826–6832. DOI: <https://doi.org/10.1364/AO.38.006826>.
- (2006). “Absorption and scattering of light in natural waters”, in *Light Scattering Reviews*. Springer, Praxis Publishing Ltd. ISBN: 978-3-540-37672-9.
- Heim, Birgit et al. (2014). “Ocean colour remote sensing in the southern Laptev Sea: evaluation and applications”. In: *Biogeosciences (BG)* 11.15, pp. 4191–4210.

- Held, I. M. and B. J. Soden (2006). “Robust Responses of the Hydrological Cycle to Global Warming”. In: *Journal of Climate* 19.21, pp. 5686–5699. DOI: <https://doi.org/10.1175/JCLI3990.1>.
- Hill, Victoria J. (2008). “Impacts of chromophoric dissolved organic material on surface ocean heating in the Chukchi Sea”. In: *Journal of Geophysical Research* 113.C07024, pp. 1–10. DOI: [doi:10.1029/2007JC004119](https://doi.org/10.1029/2007JC004119).
- Holloway, G. et al. (2007). “Water properties and circulation in Arctic Ocean models”. In: *Journal of Geophysical Research: Oceans* 112, C04S03. DOI: [10.1029/2018JC014303](https://doi.org/10.1029/2018JC014303).
- Holmes, Robert Max et al. (2012). “Seasonal and annual fluxes of nutrients and organic matter from large rivers to the Arctic Ocean and surrounding seas”. In: *Estuaries and Coasts* 35.2, pp. 369–382.
- IPCC (2013). *Climate Change 2013: The Physical Science Basis. Contribution of Working Group I to the Fifth Assessment Report of the Intergovernmental Panel on Climate Change*. Cambridge, United Kingdom and New York, NY, USA: Cambridge University Press, p. 1535. ISBN: ISBN 978-1-107-66182-0. DOI: [10.1017/CB09781107415324](https://doi.org/10.1017/CB09781107415324). URL: [www.climatechange2013.org](http://www.climatechange2013.org).
- Jackett, D. R. and T. J. McDougall (1995). “Minimal Adjustment of Hydrographic Profiles to Achieve Static Stability”. In: *J. Atmos. Oceanic Technol.* 12.2, pp. 381–389. DOI: [https://doi.org/10.1175/1520-0426\(1995\)012<0381:MAOHPT>2.0.CO;2](https://doi.org/10.1175/1520-0426(1995)012<0381:MAOHPT>2.0.CO;2).
- Janout, M. et al. (2016). “Episodic warming of near-bottom waters under the arctic sea ice on the central Laptev Sea shelf”. In: *Geophysical Research Letter* 43, pp. 264–272. DOI: [10.1002/2015GL066565](https://doi.org/10.1002/2015GL066565).
- Janout, Markus A. et al. (2015). “Kara Sea freshwater transport through Vilkitsky Strait: Variability, forcing, and further pathways toward the western Arctic Ocean from a model and observations”. In: *Journal of Geophysical Research: Oceans* 120.7, pp. 4925–4944. DOI: <https://doi.org/10.1002/2014JC010635>.
- Jerlov, N. G. (1976). *Marine Optics*. Elsevier Scientific Publishing Company, Amsterdam. ISBN: 0-444-41490-8.
- Johnson, M. et al. (2007). “A comparison of Arctic Ocean sea ice concentration among the coordinated AOMIP model experiments”. In: *Journal of Geophysical Research* 112, C04S11. DOI: [10.1029/2006JC003690](https://doi.org/10.1029/2006JC003690).
- Jolliff, Jason K. and Travis A. Smith (2014). “Biological modulation of upper ocean physics: Simulating the biothermal feedback effect in Monterey Bay, California”.

- In: *Journal of Geophysical Research: Biogeosciences* 119, pp. 703–721. DOI: [10.1002/2013JG002522](https://doi.org/10.1002/2013JG002522).
- Jolliff, Jason K. et al. (2012). “The impact of coastal phytoplankton blooms on ocean-atmosphere thermal energy exchange: Evidence from a two-way coupled numerical modeling system”. In: *Geophysical Research Letters* 39, p. L24607. DOI: <https://doi.org/10.1029/2012GL053634>.
- Juhls, Bennet et al. (2019). “Dissolved organic matter at the fluvial-marine transition in the Laptev Sea using in situ data and ocean colour remote sensing”. In: *Biogeosciences* 16.13, pp. 2693–2713. DOI: <https://doi.org/10.5194/bg-16-2693-2019>.
- Juhls, Bennet et al. (2020). “Identifying Drivers of Seasonality in Lena River Biogeochemistry and Dissolved Organic Matter Fluxes”. In: *Frontiers in Environmental Science* 8, p. 53. DOI: [10.3389/fenvs.2020.00053](https://doi.org/10.3389/fenvs.2020.00053).
- Kim, A.-H. et al. (2018a). “Polar Cooling Effect Due to Increase of Phytoplankton and Dimethyl-Sulfide Emission”. In: *Atmosphere* 9.10, p. 384. DOI: [10.3390/atmos9100384](https://doi.org/10.3390/atmos9100384).
- Kim, Grace E., Anand Gnanadesikan, and Marie-Aude Pradal (2016). “Increased Surface Ocean Heating by Colored Detrital Matter (CDM) Linked to Greater Northern Hemisphere Ice Formation in the GFDL CM2Mc ESM”. In: *Journal of Climate* 29.24, pp. 9063–9076. DOI: [10.1175/JCLI-D-16-0053.1](https://doi.org/10.1175/JCLI-D-16-0053.1).
- Kim, Grace E., Marie-Aude Pradal, and Anand Gnanadesikan (2015). “Quantifying the biological impact of surface ocean light attenuation by colored detrital matter in an ESM using a new optical parameterization”. In: *Biogeosciences* 12, pp. 5119–5132. DOI: <https://doi.org/10.5194/bg-12-5119-2015>.
- Kim, Grace E. et al. (2018b). “Upper Ocean Cooling in a Coupled Climate Model Due to Light Attenuation by Yellowing Materials”. In: *Geophysical Research Letters* 45, pp. 6134–6140. DOI: <https://doi.org/10.1029/2018GL077297>.
- Kirk, John T. O. (2011). *Light and Photosynthesis in Aquatic Ecosystems*. 3rd ed. Cambridge University Press. ISBN: 978-0-521-15175-7.
- Kobayashi, S. et al. (2015). “The JRA-55 Reanalysis: General Specifications and Basic Characteristics”. In: *Journal of the Meteorological Society of Japan. Ser. II* 93.1, pp. 5–48. DOI: [10.2151/jmsj.2015-001](https://doi.org/10.2151/jmsj.2015-001).
- Kopelevich, O. V. (1983). “Small-Parametric Model of the Optical Properties of Seawater”. In: *Ocean Optics* 1, pp. 208–234.



- Large, W. G., J. C. McWilliams, and S. C. Doney (1994). “Oceanic vertical mixing: A review and a model with a nonlocal boundary layer parameterization”. In: *Reviews of Geophysics* 32, pp. 363–403. DOI: <https://doi.org/10.1029/94RG01872>.
- Large, W. G. and S. Yeager (2004). “Diurnal to decadal global forcing for ocean and sea-ice models: The data sets and flux climatologies”. In: *University Corporation for Atmospheric Research NCAR/TN-460+STR*. DOI: [10.5065/D6KK98Q6](https://doi.org/10.5065/D6KK98Q6).
- Large, W.G. and A.J.G. Nurser (2001). “Ocean surface water mass transformation”. In: *Ocean Circulation and Climate: Observing and Modelling the Global Ocean*. Ed. by G. Siedler, J. Church, and J. Gould. 77. Academic Press, pp. 317–336.
- Leith, C.E. (1996). “Stochastic models of chaotic systems”. In: *Physica D: Nonlinear Phenomena* 98.2, pp. 481–491. DOI: [https://doi.org/10.1016/0167-2789\(96\)00107-8](https://doi.org/10.1016/0167-2789(96)00107-8).
- Lengaigne, Matthieu et al. (2009). “Bio-physical feedbacks in the Arctic Ocean using an Earth system model”. In: *Geophysical Research Letters* 36, p. L21602. DOI: <https://doi.org/10.1029/2009GL040145>.
- Lewis, K. M., G. L. van Dijken, and K. R. Arrigo (2020). “Changes in phytoplankton concentration now drive increased Arctic Ocean primary production”. In: *Science* 369.6500, pp. 198–202. DOI: [10.1126/science.aay8380](https://doi.org/10.1126/science.aay8380).
- Lewis, M. R. et al. (1990). “Influence of penetrating solar radiation on the heat budget of the equatorial Pacific Ocean”. In: *Nature* 347, 543–545. DOI: <https://doi.org/10.1038/347543a0>.
- Lim, H., Jong-Seong Kug, and Jong-Yeon Park (2018). “Biogeophysical feedback of phytoplankton on the Arctic climate. Part I: Impact of nonlinear rectification of interactive chlorophyll variability in the present-day climate”. In: *Climate Dynamics* 52.9-10, pp. 5383–5396. DOI: [10.1007/s00382-018-4450-6](https://doi.org/10.1007/s00382-018-4450-6).
- Losa, S. N. et al. (2019). “On modeling the Southern Ocean Phytoplankton Functional Types”. In: *Biogeosciences Discussions* 12, pp. 1–37. DOI: [10.5194/bg-2019-289](https://doi.org/10.5194/bg-2019-289).
- Losa, Svetlana N. et al. (2006). “3D ecosystem modelling in the North Atlantic: Relative impacts of physical and biological parameterizations”. In: *Journal of Marine Systems* 61.3. Workshop on Future Directions in Modelling Physical-Biological Interactions (WKFDPI), pp. 230–245. DOI: <https://doi.org/10.1016/j.jmarsys.2005.09.011>.
- Losch, M et al. (2010). “On the formulation of sea-ice models. Part 1: Effects of different solver implementations and parameterizations”. In: *Ocean Modelling* 33.1-2, pp. 129–144. DOI: [10.1016/j.ocemod.2009.12.008](https://doi.org/10.1016/j.ocemod.2009.12.008).



- Manizza, Manfredi et al. (2005). “Bio-optical feedbacks among phytoplankton, upper ocean physics and sea-ice in a global model”. In: *Geophysical Research Letters* 32, p. L05603. DOI: [doi:10.1029/2004GL020778](https://doi.org/10.1029/2004GL020778).
- Marshall, John et al. (1997). “A finite-volume, incompressible Navier Stokes model for studies of the ocean on parallel computers”. In: *Journal of Geophysical Research: Oceans* 102.C3, pp. 5753–5766. DOI: <https://doi.org/10.1029/96JC02775>.
- Marzeion, B. et al. (2005). “Biophysical Feedbacks in the Tropical Pacific”. In: *Journal of Climate* 18.1, pp. 58–70. DOI: <https://doi.org/10.1175/JCLI3261.1>.
- Matsuoka, A. et al. (2014). “A synthesis of light absorption properties of the Arctic Ocean: application to semianalytical estimates of dissolved organic carbon concentrations from space”. In: *Biogeosciences* 11.12, pp. 3131–3147. DOI: [10.5194/bg-11-3131-2014](https://doi.org/10.5194/bg-11-3131-2014). URL: <https://bg.copernicus.org/articles/11/3131/2014/>.
- Menemenlis, D. et al. (2008). “High resolution global ocean and sea ice data synthesis”. In: *Mercator Ocean Quartely Newsletter* 31, pp. 13–21.
- Mignot, J. et al. (2013). “On the evolution of the oceanic component of the IPSL climate models from CMIP3 to CMIP5: A mean state comparison”. In: *Ocean Modelling* 72, pp. 167–184. DOI: <https://doi.org/10.1016/j.ocemod.2013.09.001>.
- Morison J., Kwok R. Peralta-Ferriz C. et al. (2012). “The Arctic Oscillation, rather than the Beaufort High, is the main factor affecting the freshening of the Arctic Ocean since the 1990s”. In: *Nature* 481.3, pp. 66–70. DOI: <https://doi.org/10.1038/nature10705>.
- Morrison, J. Ruairidh and Norman B. Nelson (2004). “Seasonal cycle of phytoplankton UV absorption at the Bermuda Atlantic Time-series Study (BATS) site”. In: *Limnology and Oceanography* 49.1, pp. 215–224. DOI: <https://doi.org/10.4319/lo.2004.49.1.0215>.
- Naval Oceanographic Office, N. O. O (2018). *GHRSSST Level 4 K10\_SST Global 1 meter Sea Surface Temperature Analysis. Ver. 1.0. PO.DAAC, CA, USA*. <http://dx.doi.org/10.5067/GHK10-41N01>. Accessed: 2018-02-27.
- Onarheim, I. H. et al. (2018). “Seasonal and regional manifestation of Arctic sea ice loss”. In: *Journal of Climate* 31, pp. 4917–4932.
- Örek, H et al. (2013). “Contribution to a bio-optical model for remote sensing of Lena River water”. In: *Biogeosciences* 10.11, p. 7081.

- Oschlies, A. (2004). "Feedbacks of biotically induced radiative heating on upper-ocean heat budget, circulation, and biological production in a coupled ecosystem-circulation model". In: *Journal of Geophysical Research* 109, p. C12031. DOI: [10.1029/2004JC002430](https://doi.org/10.1029/2004JC002430).
- Overeem, Irina and James P. M. Syvitski (2010). "Shifting discharge peaks in Arctic rivers, 1977–2007". In: *Geografiska Annaler: Series A, Physical Geography* 92.2, pp. 285–296. DOI: <https://doi.org/10.1111/j.1468-0459.2010.00395.x>.
- Oziel, L. et al. (2020). "Faster Atlantic currents drive poleward expansion of temperate phytoplankton in the Arctic Ocean". In: *Nature Communications* 11.1705. DOI: <https://doi.org/10.1038/s41467-020-15485-5>.
- Paasche, E. (2001). "A review of the coccolithophorid *Emiliana huxleyi* (Prymnesiophyceae), with particular reference to growth, coccolith formation, and calcification-photosynthesis interactions". In: *Phycologia* 40.6, pp. 503–529. DOI: [10.2216/i0031-8884-40-6-503.1](https://doi.org/10.10031-8884-40-6-503.1).
- Pabi, Sudeshna, Gert L. van Dijken, and Kevin R. Arrigo (2008). "Primary production in the Arctic Ocean, 1998–2006". In: *Journal of Geophysical Research: Oceans* 113.C8. DOI: <https://doi.org/10.1029/2007JC004578>.
- Park, Jong-Yeon et al. (2015). "Amplified Arctic warming by phytoplankton under greenhouse warming". In: *Proceedings of the National Academy of Sciences* 112.19, pp. 5921–5926. DOI: [10.1073/pnas.1416884112](https://doi.org/10.1073/pnas.1416884112).
- Parkinson, C. L. and J. C. Comiso (2013). "On the 2012 record low Arctic sea ice cover: Combined impact of preconditioning and an August storm". In: *Geophysical Research Letters* 40, pp. 1356–1361. DOI: [10.1002/grl.50349](https://doi.org/10.1002/grl.50349).
- Patara, Lavinia et al. (2012). "Global response to solar radiation absorbed by phytoplankton in a coupled climate model". In: *Climate Dynamics* 39, pp. 1951–1968. DOI: [10.1007/s00382-012-1300-9](https://doi.org/10.1007/s00382-012-1300-9).
- Paulson, C. A. and J. J. Simpson (1977). "Irradiance measurements in the upper ocean". In: *Journal of Physical Oceanography* 7.6, pp. 952–956. DOI: [https://doi.org/10.1175/1520-0485\(1977\)007<0952:IMITU0>2.0.CO;2](https://doi.org/10.1175/1520-0485(1977)007<0952:IMITU0>2.0.CO;2).
- Pefanis, Vasileios et al. (2020). "Amplified Arctic Surface Warming and Sea Ice Loss Due to Phytoplankton and Colored Dissolved Material". In: *Geophysical Research Letters* 47.21, e2020GL088795. DOI: <https://doi.org/10.1029/2020GL088795>. URL: <https://agupubs.onlinelibrary.wiley.com/doi/abs/10.1029/2020GL088795>.

- Pegau, W Scott (2002). “Inherent optical properties of the central Arctic surface waters”. In: *Journal of Geophysical Research: Oceans* 107.C10.
- Peng, G. et al. (2013). “A long-term and reproducible passive microwave sea ice concentration data record for climate studies and monitoring”. In: *Earth System Science Data* 5, pp. 311–318. DOI: [10.5194/essd-5-311-2013](https://doi.org/10.5194/essd-5-311-2013).
- Perovich, D. et al. (2019). “Update for 2019”. In: *Arctic report card: sea ice*. URL: <https://arctic.noaa.gov/Report-Card/Report-Card-2019/ArtMID/7916/ArticleID/841/Sea-Ice>.
- Peterson, Bruce J. et al. (2002). “Increasing River Discharge to the Arctic Ocean”. In: *Science* 298.5601, pp. 2171–2173. DOI: [10.1126/science.1077445](https://doi.org/10.1126/science.1077445).
- Petty, A. A. et al. (2018). “The Arctic sea ice cover of 2016: a year of record-low highs and higher-than-expected lows”. In: *The Cryosphere* 12.2, pp. 433–452. DOI: [10.5194/tc-12-433-2018](https://doi.org/10.5194/tc-12-433-2018). URL: <https://tc.copernicus.org/articles/12/433/2018/>.
- Pistone, Kristina, Ian Eisenman, and V. Ramanathan (2014). “Observational determination of albedo decrease caused by vanishing Arctic sea ice”. In: *Proceedings of the National Academy of Sciences* 111.9, pp. 3322–3326. DOI: [10.1073/pnas.1318201111](https://doi.org/10.1073/pnas.1318201111).
- Pithan, F. and T. Mauritsen (2014). “Arctic amplification dominated by temperature feedbacks in contemporary climate models”. In: *Nature Geoscience* 7, pp. 181–184. DOI: <https://doi.org/10.1038/ngeo2071>.
- Pope, R. M. and E. S. Fry (1997). “Absorption spectrum (380–700 nm) of pure water. II. Integrating cavity measurements”. In: *Applied Optics* 36, pp. 8710–8723. DOI: [10.1364/AO.36.008699](https://doi.org/10.1364/AO.36.008699).
- Popova, E. E. et al. (2013). “Role of advection in Arctic Ocean lower trophic dynamics: A modeling perspective”. In: *Journal of Geophysical Research: Oceans* 118.3, pp. 1571–1586. DOI: <https://doi.org/10.1002/jgrc.20126>.
- Prieur, L. and S. Sathyendranath (1981). “An optical classification of coastal and oceanic waters based on the specific spectral absorption curves of phytoplankton pigments, dissolved organic matter, and other particulate materials”. In: *Limnology and Oceanography* 26, pp. 671–689. DOI: <https://doi.org/10.4319/lo.1981.26.4.0671>.
- Quéguiner, Bernard (2013). “Iron fertilization and the structure of planktonic communities in high nutrient regions of the Southern Ocean”. In: *Deep Sea Research Part*

- II: Topical Studies in Oceanography* 90, pp. 43–54. DOI: <https://doi.org/10.1016/j.dsr2.2012.07.024>.
- Raymond, Peter A. et al. (2007). “Flux and age of dissolved organic carbon exported to the Arctic Ocean: A carbon isotopic study of the five largest arctic rivers”. In: *Global Biogeochemical Cycles* 21.4, GB4011.
- Roesler, C. S. and M. J. Perry (1995). “In situ phytoplankton absorption, fluorescence emission, and particulate backscattering spectra determined from reflectance”. In: *Journal of Geophysical Research* 100.C7, pp. 13279–13294. DOI: [10.1029/95JC00455](https://doi.org/10.1029/95JC00455).
- Röttgers, Rüdiger, David McKee, and Christian Utschig (2014). “Temperature and salinity correction coefficients for light absorption by water in the visible to infrared spectral region”. In: *Optics express* 22.21, pp. 25093–25108.
- Rozanov, V. V. et al. (2002). “SCIATRAN - a new radiative transfer model for geophysical applications in the 240–2400 nm spectral region: the pseudo-spherical version”. In: *Adv. Space Res.* 29.11, pp. 1831–1835. ISSN: 0273-1177. DOI: [10.1016/S0273-1177\(02\)00095-9](https://doi.org/10.1016/S0273-1177(02)00095-9). URL: <http://www.sciencedirect.com/science/article/pii/S0273117702000959>.
- Rozanov, V. V. et al. (2014). “Radiative transfer through terrestrial atmosphere and ocean: Software package SCIATRAN”. In: *J. Quant. Spectr. Radiat. Transfer* 133.0, pp. 13–71. DOI: [10.1016/j.jqsrt.2013.07.004](https://doi.org/10.1016/j.jqsrt.2013.07.004).
- Rozanov, V. V. et al. (2017). “Radiative transfer modeling through terrestrial atmosphere and ocean accounting for inelastic processes: Software package SCIATRAN”. In: *Journal of Quantitative Spectroscopy and Radiative Transfer*.
- Sakshaug, E. (2004). “Primary and Secondary Production in the Arctic Seas”. In: *The Organic Carbon Cycle in the Arctic Ocean*. Ed. by Ruediger Stein and Robie W. MacDonald. Berlin, Heidelberg: Springer Berlin Heidelberg, pp. 57–81. DOI: [10.1007/978-3-642-18912-8\\_3](https://doi.org/10.1007/978-3-642-18912-8_3).
- Schneider, B. et al. (2008). “Climate-induced interannual variability of marine primary and export production in three global coupled climate carbon cycle models”. In: *Biogeosciences* 5.2, pp. 597–614. DOI: [10.5194/bg-5-597-2008](https://doi.org/10.5194/bg-5-597-2008).
- Segelstein, D. J. (Sept. 1981). “The Complex Refractive Index of Water”. MA thesis. Kansas City, MO.: University of Missouri.
- Senftleben, D., A. Lauer, and A. Karpechko (2020). “Constraining Uncertainties in CMIP5 Projections of September Arctic Sea Ice Extent with Observations”. In: *Journal of Climate* 33, pp. 1487–1503. DOI: [10.1175/JCLI-D-19-0075.1](https://doi.org/10.1175/JCLI-D-19-0075.1).

- Serreze, M. C. et al. (2009). “The emergence of surface-based Arctic amplification”. In: *The Cryosphere* 3.1, pp. 11–19. DOI: [10.5194/tc-3-11-2009](https://doi.org/10.5194/tc-3-11-2009). URL: <https://tc.copernicus.org/articles/3/11/2009/>.
- Serreze, Mark C and Roger G Barry (2011). “Processes and impacts of Arctic amplification: A research synthesis”. In: *Global and Planetary Change* 77.1, pp. 85–96.
- Siegel, D., S. Doney, and J. Yoder (2002). “The North Atlantic spring phytoplankton bloom and Sverdrup’s critical depth hypothesis”. In: *Science* 296.5568, 730–733. DOI: [10.1126/science.1069174](https://doi.org/10.1126/science.1069174).
- Siegel, David A. et al. (1995). “Solar radiation, phytoplankton pigments and the radiant heating of the equatorial Pacific warm pool”. In: *Journal of Geophysical Research: Oceans* 100.C3, pp. 4885–4891. DOI: <https://doi.org/10.1029/94JC03128>.
- SIMIP Community (2020). “Arctic Sea Ice in CMIP6”. In: *Geophysical Research Letters* 47.10, e2019GL086749. DOI: <https://doi.org/10.1029/2019GL086749>. URL: <https://agupubs.onlinelibrary.wiley.com/doi/abs/10.1029/2019GL086749>.
- Smith, R. C. and K. S. Baker (1981). “Optical properties of the clearest natural waters (200–800 nm)”. In: *Applied Optics* 20, pp. 177–184. DOI: [10.1364/AO.20.000177](https://doi.org/10.1364/AO.20.000177).
- Smith, Walter H. F. and David T. Sandwell (1997). “Global Sea Floor Topography from Satellite Altimetry and Ship Depth Soundings”. In: *Science* 277.5334, pp. 1956–1962. DOI: [10.1126/science.277.5334.1956](https://doi.org/10.1126/science.277.5334.1956).
- Sogandares, F. M. and E. S. Fry (1997). “Absorption spectrum (340–640 nm) of pure water. I. Photothermal measurements”. In: *Applied Optics* 36, pp. 8699–8709. DOI: [10.1364/AO.36.008699](https://doi.org/10.1364/AO.36.008699).
- Sonntag, S. and I. Hense (2011). “Phytoplankton behavior affects ocean mixed layer dynamics through biological–physical feedback mechanisms”. In: *Geophysical Research Letters* 38, p. L15610. DOI: [10.1029/2011GL048205](https://doi.org/10.1029/2011GL048205).
- Soppa, Mariana A., Christoph Völker, and Astrid Bracher (2016). “Diatom Phenology in the Southern Ocean: Mean Patterns, Trends and the Role of Climate Oscillations”. In: *Remote Sensing* 8.5. DOI: [10.3390/rs8050420](https://doi.org/10.3390/rs8050420).
- Soppa, Mariana A. et al. (2019). “Assessing the Influence of Water Constituents on the Radiative Heating of Laptev Sea Shelf Waters”. In: *Frontiers in Marine Science* 6.221, pp. 1–13. DOI: <https://doi.org/10.3389/fmars.2019.00221>.
- Stedmon, C. A. and S. Markager (2001). “The optics of chromophoric dissolved organic matter (CDOM) in the Greenland Sea: An algorithm for differentiation between

- marine and terrestrially derived organic matter”. In: *Limnology and Oceanography* 46.8, pp. 2087–2093. DOI: <https://doi.org/10.4319/lo.2001.46.8.2087>.
- Stedmon, C. A. et al. (2011). “The supply and characteristics of colored dissolved organic matter (CDOM) in the Arctic Ocean: Pan Arctic trends and differences”. In: *Marine Chemistry* 124.1, pp. 108–118. DOI: <https://doi.org/10.1016/j.marchem.2010.12.007>.
- Steele, M., R. Morley, and W. Ermold (2001). “PHC: A Global Ocean Hydrography with a High-Quality Arctic Ocean”. In: *Journal of Climate* 14, pp. 2079–2087. DOI: [https://doi.org/10.1175/1520-0442\(2001\)014<2079:PAGOHW>2.0.CO;2](https://doi.org/10.1175/1520-0442(2001)014<2079:PAGOHW>2.0.CO;2).
- Stroeve, J. C. et al. (2012). “Trends in Arctic sea ice extent from CMIP5, CMIP3 and observations”. In: *Geophysical Research Letters* 39, p. L16502. DOI: [10.1029/2012GL052676](https://doi.org/10.1029/2012GL052676).
- Syed, T. H. et al. (2007). “Contemporary estimates of Pan-Arctic freshwater discharge from GRACE and reanalysis”. In: *Geophysical Research Letters* 34.19. DOI: <https://doi.org/10.1029/2007GL031254>.
- Tarnocai, C. et al. (2009). “Soil organic carbon pools in the northern circumpolar permafrost region”. In: *Global Biogeochemical Cycles* 23.2, GB2023. DOI: <https://doi.org/10.1029/2008GB003327>.
- Terhaar, J. et al. (2019). “Simulated Arctic Ocean Response to Doubling of Riverine Carbon and Nutrient Delivery”. In: *Global Biogeochemical Cycles* 33.8, pp. 1048–1070. DOI: <https://doi.org/10.1029/2019GB006200>.
- Timmermans, M.-L. (2015). “The impact of stored solar heat on Arctic sea ice growth”. In: *Geophysical Research Letters* 42.15, pp. 6399–6406. DOI: <https://doi.org/10.1002/2015GL064541>.
- Tremblay, J-E. et al. (2015). “Global and regional drivers of nutrient supply, primary production and CO<sub>2</sub> drawdown in the changing Arctic Ocean”. In: *Progress in Oceanography* 139, pp. 171–196. DOI: <https://doi.org/10.1016/j.pocean.2015.08.009>.
- Walsh, J.E. (2005). “Cryosphere and hydrology”. In: *Arctic Climate Impact Assessment*. Cambridge: Cambridge University Press. Chap. 6, pp. 183–242.
- Wekerle, Claudia et al. (2017). “Eddy-Resolving Simulation of the Atlantic Water Circulation in the Fram Strait With Focus on the Seasonal Cycle”. In: *Journal of Geophysical Research: Oceans* 122.11, pp. 8385–8405. DOI: <https://doi.org/10.1002/2017JC012974>.

- Wendisch, M. et al. (2017). “Understanding Causes and Effects of Rapid Warming in the Arctic”. In: *Eos* 98. DOI: <https://doi.org/10.1029/2017E0064803>.
- Werdell, P. J. et al. (2013). “Generalized ocean color inversion model for retrieving marine inherent optical properties”. In: *Applied Optics* 52.10, pp. 2019–2037. DOI: [10.1364/AO.52.002019](https://doi.org/10.1364/AO.52.002019). URL: <http://ao.osa.org/abstract.cfm?URI=ao-52-10-2019>.
- Wetzel, P. et al. (2006). “Effects of Ocean Biology on the Penetrative Radiation in a Coupled Climate Model”. In: *Journal of Climate* 19.16, pp. 3973–3987. DOI: <https://doi.org/10.1175/JCLI3828.1>.





# Acknowledgements

First and foremost, I would like to express my deepest gratitude to my PhD supervisor Prof. Torsten Kanzow for providing guidance and valuable advice, and for helping me to move forward with my PhD. I would also like to thank all my coauthors and my PhD committee members and especially Dr. Svetlana Losa for her valuable scientific, technical, but also personal support during the last years. I thank Dr. Martin Losch for providing support on the MITgcm and his insights on my results. Finally, I would like to express my gratitude to Dr. Maren Walter for accepting to review my thesis.

I am also thankful to the community of PhD students at the AWI, and especially for being part of a great Dokteam with: Onur, Bimo, Jenna, JC, Daniel, and Daniela. Thanks to Yangyang, Onur, Joyce, Saeid, Marianne, Sara, Jan, Ilias, Stephan, Janosch, Moritz, Julia and many others, for the nice time in Bremerhaven. Thanks to all my friends, close by or far away, that made life nicer and especially to Christos.

Furthermore, I would also like to thank the PROCEED Office; especially Fenina Buttler for being such a compassionate and empathetic person, as well as for her invaluable help and guidance in overcoming difficulties.

Last but not least, I'd like to thank my parents for their encouragement throughout my whole life and Konstantina for supporting and accompanying me during the last years.

I gratefully acknowledge the funding by the Deutsche Forschungsgemeinschaft (DFG, German Research Foundation) with the corresponding project number 268020496 - TRR 172, within the Transregional Collaborative Research Center ArctiC Amplification: Climate Relevant Atmospheric and SurfaCe Processes, and Feedback Mechanisms (AC)<sup>3</sup>.



## Appendix A

## Appendix A

### A.1 Heat budget analysis

#### A.1.1 Robustness

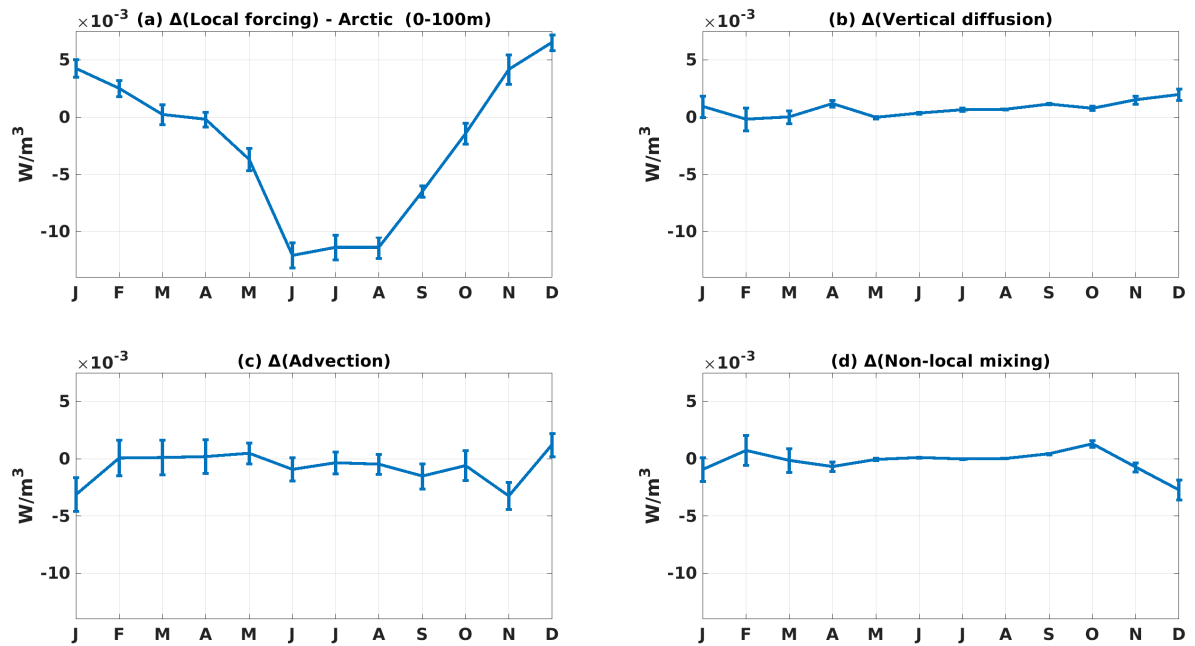


FIGURE A.1: Monthly mean differences between YELLOW and GREEN in the components of the heat budget, averaged over the upper 100 m of the water column: a) in local forcing, b) in vertical diffusion, c) in advection, and d) in non-local mixing. The values are averages over the Arctic ( $>66^\circ N$ ) in  $W/m^3$ . The error bars represent the monthly standard error.

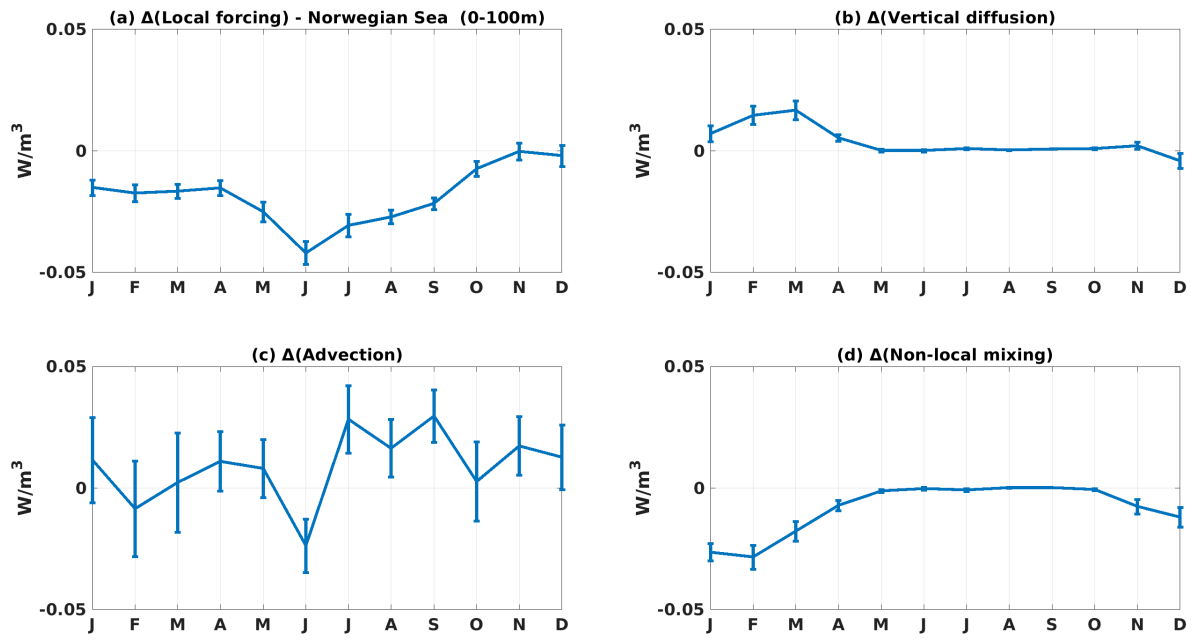


FIGURE A.2: Monthly mean differences between YELLOW and GREEN in the components of the heat budget, averaged over the upper 100 m of the water column: a) in local forcing, b) in vertical diffusion, c) in advection, and d) in non-local mixing. The values are averages over the Norwegian Sea. The error bars represent the monthly standard error.

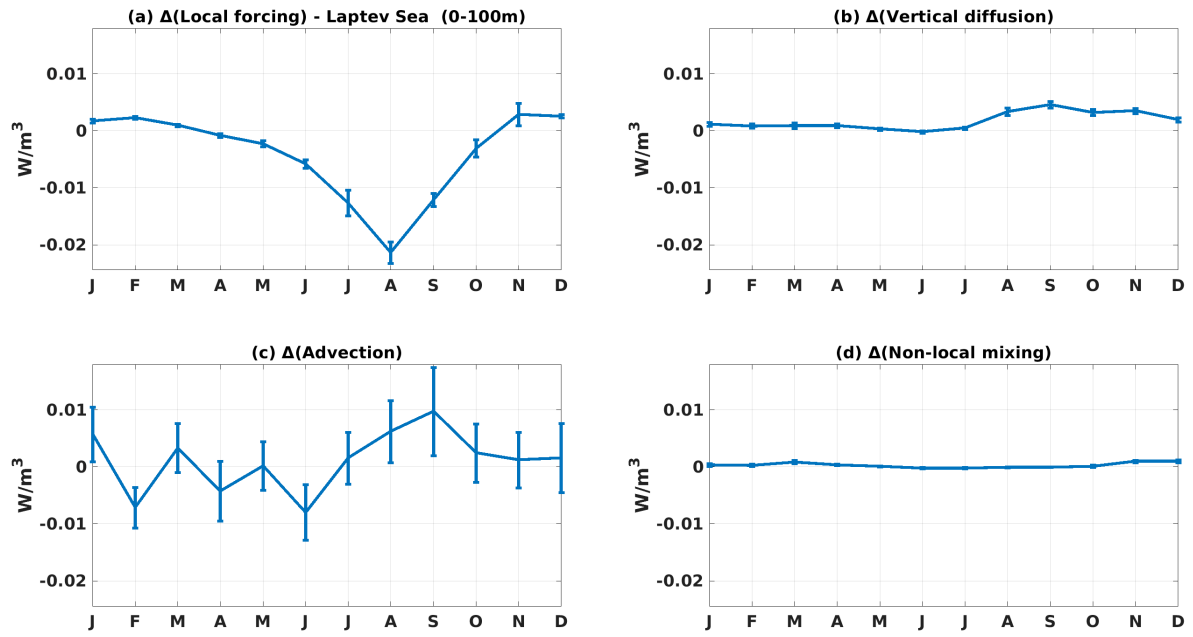


FIGURE A.3: Monthly mean differences between YELLOW and GREEN in the components of the heat budget, averaged over the upper 100 m of the water column: a) in local forcing, b) in vertical diffusion, c) in advection, and d) in non-local mixing. The values are averages over the Laptev Sea ( $105-150^\circ E$ ) in  $W/m^3$ . The error bars represent the monthly standard error.

## A.2 Phytoplankton phenology

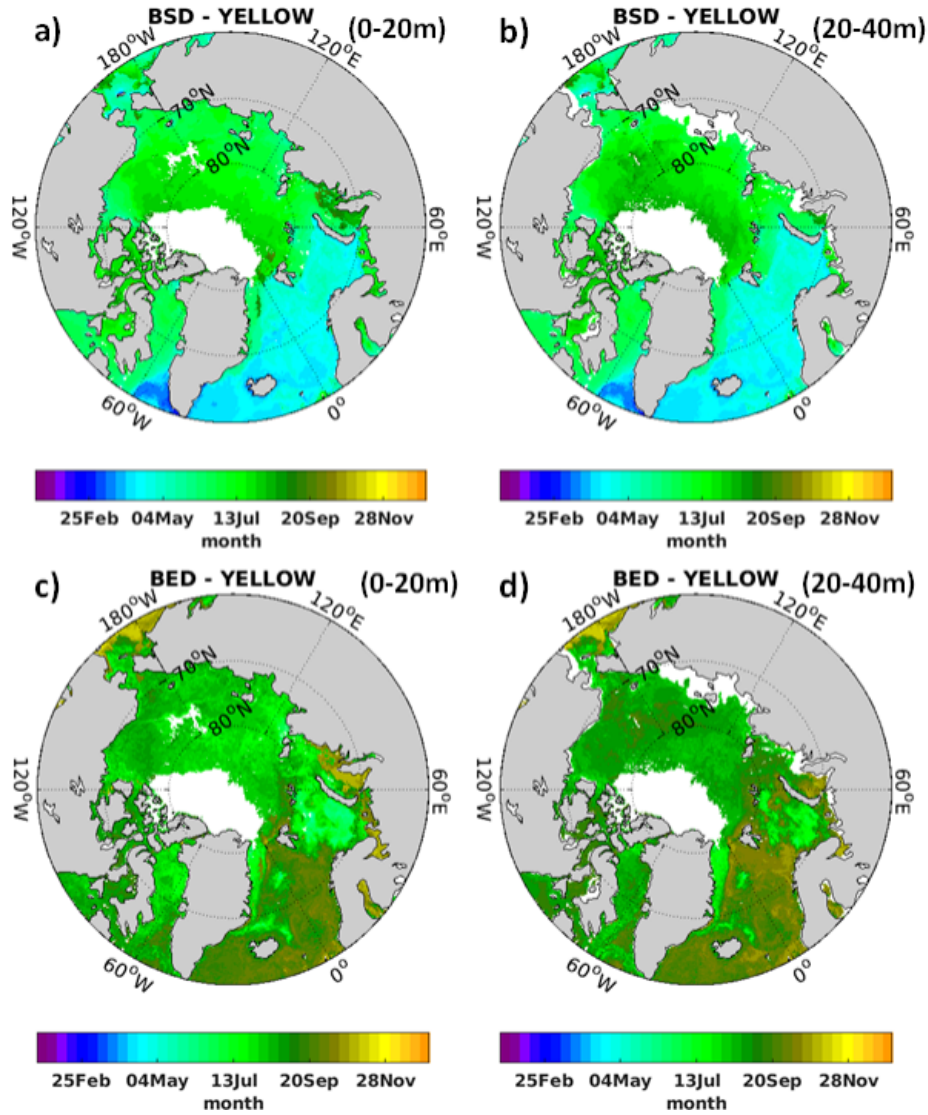


FIGURE A.4: Spatial distribution of diatoms (large and small) phenology in the simulation YELLOW, in 2012: a) bloom start day (BSD) at the surface (0-20m), b) and at the sub-surface (20-40m), c) bloom end day (BED) at the surface (0-20m), d) and at the sub-surface (20-40m).

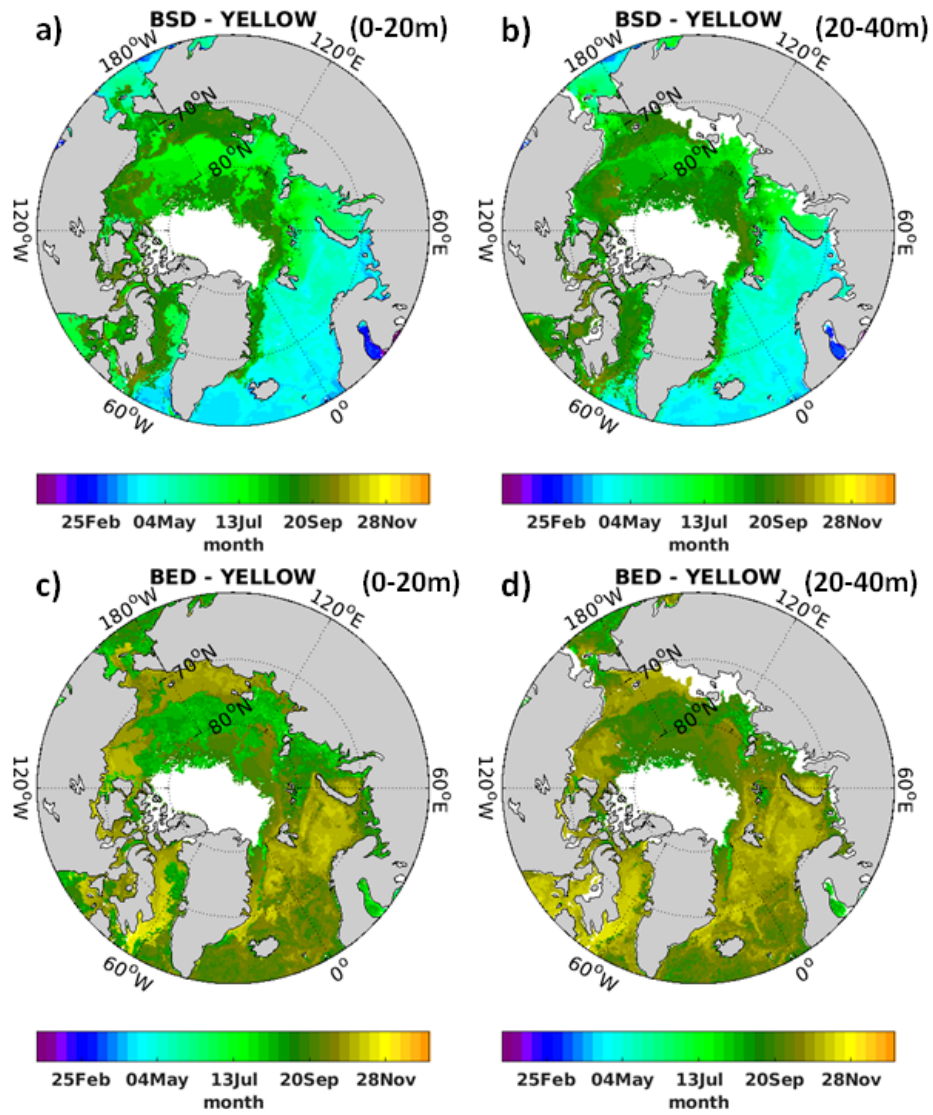


FIGURE A.5: The same as Fig. A.4, but for haptophytes.





# Appendix B

# Appendix B

## B.1 Model output

TABLE B.1: MITgcm diagnostics required for the calculation of the heat budget terms.

Diagnostics			
Term	Name	Field	Unit
Shortwave heating	oceQsw	Net shortwave radiation	W m <sup>-2</sup>
	TFLUX	Total heat flux	W m <sup>-2</sup>
Vertical diffusion	DFrI_TH	Implicit vertical diffusive flux of pot. temp.	°C m <sup>3</sup> s <sup>-1</sup>
Advection	ADVx_TH	Zonal pot. temp. advection	°C m <sup>3</sup> s <sup>-1</sup>
	ADVy_TH	Meridional pot. temp. advection	°C m <sup>3</sup> s <sup>-1</sup>
	ADVr_TH	Vertical pot. temp. advection	°C m <sup>3</sup> s <sup>-1</sup>
Non-local mixing	KPPg_TH	KPP non-local flux of pot. temp	°C m <sup>3</sup> s <sup>-1</sup>

## B.2 Model configuration

TABLE B.2: Model parameters in the MITgcm configuration "data" file.

Parameter choice	Explanation
viscAr= 5.6614e-04	Vertical eddy viscosity
rhonil=1027.5	Reference density
rhoConstFresh=999.8	Reference density for freshwater
eosType='JMD95Z'	Equation of State
hFacMin=0.3	Minimum threshold for hFac
hFacSup=5.	Upper threshold for hFac
select_rStar=2	Choice of rescaled vertical coordinate
nonlinFreeSurf=4	Choice of non-linear free surface
implicitDiffusion=.TRUE.	Implicit vertical diffusion on/off flag
implicitViscosity=.TRUE.	Implicit viscosity on/off flag
viscC4Leith=1.5	Leith biharm viscosity factor
viscA4GridMax=1.	Maximum grid dependent biharmonic viscosity
viscA4GridMin=0.001	Minimum grid dependent biharmonic viscosity
viscA4=1.e9	Lateral biharmonic viscosity
useAreaViscLength=.TRUE.	Use area for visc length instead of geom. mean
sideDragFactor=0.	side-drag scaling factor
highOrderVorticity = .TRUE.	High order interp. of vort. flag
bottomDragQuadratic = 0.0021	Quadratic bottom-drag coefficient
tempAdvScheme=7	Multidimensional temperature advection
saltAdvScheme=7	Multidimensional salt advection
StaggerTimeStep=.TRUE.	Staggered time step
multiDimAdvection=.TRUE.	Enable multidimensional advection
vectorInvariantMomentum=.TRUE.	Enable vector-invariant momentum
implicitFreeSurface=.TRUE.	Implicit free surface
exactConserv=.TRUE.	Exact conservation of global ocean volume
useRealFreshWaterFlux=.TRUE.	Real surface freshwater exchange

# List of Figures

1.1	Time series of annual mean surface air temperature anomalies, zonally averaged, with respect to the 1946–1980 period. Data come from the Land-Ocean-Temperature index (LOTI) and the NOAA/NCEI’s Extended Reconstructed Sea Surface Temperature (ERSST) v5. The unit in the colorbar is °C, while the y axis denotes latitudes. Credit for the data and the figure: NASA Goddard Institute for Space Studies, available at: <a href="https://data.giss.nasa.gov/gistemp/zonal_means/index.html">https://data.giss.nasa.gov/gistemp/zonal_means/index.html</a> . . . . .	2
1.2	A schematic showing the optically active water constituents which absorb or scatter the incoming solar radiation. . . . .	6
1.3	Spectral absorption coefficients ( $\text{m}^{-1}$ ) of water (aw), phytoplankton (aph, for a chlorophyll-a concentration of $30 \text{ mg/m}^3$ ), NAP (aNAP, for a concentration of $25 \text{ g/m}^3$ ), CDOM (aCDOM, for a CDOM absorption of $1.6 \text{ m}^{-1}$ ) at 443 nm, and the sum of them (a). . . . .	7
1.4	Weight-specific absorption spectra of the main phytoplankton pigments, $a_{\text{sol}}^*$ (in $\text{m}^2 \text{ mg}^{-1}$ ). Absorption spectra of photosynthetic and non-photosynthetic carotenoids are shown in red and blue, respectively. Credit: Figure from Bricaud et al. (2004). . . . .	9
1.5	Illustration of a single beam of radiance and the processes affecting it as it propagates a distance $\Delta r$ . Source: <a href="http://www.oceanopticsbook.info">http://www.oceanopticsbook.info</a> . . . . .	13
1.6	Illustration of a beam of radiance in direction $(\theta', \phi')$ generating radiance in the direction of interest $(\theta, \phi)$ by elastic scattering. Source: <a href="http://www.oceanopticsbook.info">http://www.oceanopticsbook.info</a> . . . . .	14

2.1	Study area and location of sampling stations of the TRANSDRIFT-XVII and TRANSDRIFT-XIX expeditions (black). Stations used for the radiative transfer simulations are in red and stations matched with the satellite data are marked as stars. . . . .	20
3.1	Scatter plot of SCIATRAN simulated $L_{\text{TOA}}$ against MERIS $L_{\text{TOA}}$ in the visible and near infrared spectral bands. . . . .	40
3.2	Comparison of SCIATRAN simulated (black) and MERIS-L1b (red) $L_{\text{TOA}}$ at S35. . . . .	41
3.3	Simulated water-leaving radiance ( $L_{\text{W}}$ ) spectra of stations selected for radiative heating simulations. . . . .	41
3.4	A) CDOM absorption spectra ( $a_{\text{CDOM}}$ ) at 5 m depth, B) temperature profiles, and C) salinity profiles of S01 (yellow) and S40 (blue), measured <i>in situ</i> . . . . .	42
3.5	(A) Profiles of daily absorbed energy ( $E_{\text{nabs}}$ , normalized by $dz$ ) including all absorbers. (B) Profiles of daily absorbed energy ( $E_{\text{nabs}}$ , normalized by $dz$ ) at S03 including all absorbers (blue) and without CDOM (red). (C) Profiles of daily absorbed energy ( $E_{\text{nabs}}$ , normalized by $dz$ ) at S16 including all absorbers (blue), without CDOM (red), and without TSM (orange). . . . .	43
3.6	Spatial distribution of the MERIS retrieved surface: a) CDOM absorption at 443 nm, b) TSM concentration, and c) chlorophyll-a concentration in the Laptev Sea, on August 4, 2010. . . . .	46
3.7	Spatial distribution of radiative heating difference (1RH, integrated over one day) of the Laptev Sea surface waters (upper 2 m) for August 4, 2010. . . . .	47
3.8	(A) Scatterplot of $E_{\text{nabs}}$ , $a_{\text{CDOM}}(443)$ as a function of TSM. (B) Scatterplot of $E_{\text{nabs}}$ , $a_{\text{CDOM}}(443)$ as a function of Chla. . . . .	48
4.1	Temporal variation of observed (blue line) and simulated sea ice extent in YELLOW (red line), in the northern hemisphere during the 2007-2019 period. Data comes from the NOAA/NSIDC Climate Data Record of Passive Microwave sea ice Concentration, Version 3 (Peng et al., 2013)	53
4.2	For September 2012: a) simulated SIC in YELLOW, b) observed SIC from the NOAA/NSIDC Climate Data Record of Passive Microwave sea ice Concentration, Version 3 (Peng et al., 2013). . . . .	54

4.3	For September 2012: a) simulated surface chlorophyll concentrations in YELLOW, b) observed surface chlorophyll concentrations (Gohin, Druon, and Lampert, 2002) from the merged GlobColour product ( <a href="ftp://ftp.hermes.acri.fr/GlobColour/">ftp://ftp.hermes.acri.fr/GlobColour/</a> ), c) simulated surface absorption by CDOM in YELLOW, d) observed surface absorption of colored dissolved and detrital matter (CDM) at 443nm (Werdell et al., 2013) from the NASA GSF Center ( <a href="https://oceandata.sci.gsfc.nasa.gov/Aqua/Mapped/Monthly/4km/">https://oceandata.sci.gsfc.nasa.gov/Aqua/Mapped/Monthly/4km/</a> ). Although CDM accounts for the absorption from both detritus and dissolved material, it is the most suitable remote sensing product to compare against simulated CDOM. . . . .	55
4.4	Light attenuation depth differences ( $\Delta Z$ in m) between: a) YELLOW and CTRL, b) YELLOW and GREEN. The light attenuation depth ( $Z$ ) is the reciprocal of the diffuse attenuation coefficient $K_d$ . The values here account for the upper 10 m during the sunlit season, and when they are negative, they indicate a shallower light attenuation depth. The sunlit season is the time period when the mean shortwave downwelling radiation over the Arctic ( $> 66^\circ\text{N}$ ) exceeds 25% of the annual maximum. Depending on the year, it roughly corresponds to the period from April to September. . . . .	56
4.5	Mean differences between YELLOW and CTRL for: a) SST, b) 40-50 m temperature, c) SIC and d) surface heat flux (Eq. 2.15; positive changes indicate heat gain for the ocean), for August 2012. . . . .	57
4.6	Mean differences between YELLOW and CTRL over 2007-2016, for: a) SST in December, b) Sea ice thickness ( $SI_{th}$ ) in February, c) annual range of SST. December and February are the wintertime months with the largest differences observed in SST and $SI_{th}$ , respectively. . . . .	58
4.7	Difference between YELLOW and CTRL in days with more than 15% SIC, for a) 2012, and b) 2016. . . . .	59
4.8	Mean differences between YELLOW and GREEN in the summer of 2016, for: a) SST, b) 40-50 m temperature, c) SIC and d) surface heat flux (Eq. 2.15). The temperature and heat flux differences are calculated for the August, while SIC for the September of 2016. . . . .	61
4.9	Annual mean SST differences (YELLOW-GREEN) for the 2007-2016 time period. The area enclosed by the black line is referred to the text as the Norwegian Sea. . . . .	62

4.10	Mean differences (YELLOW-GREEN) in the Norwegian Sea (Fig. 4.9) in: a) the mixed layer depth (dMLD), b) the upper 200 m temperature profile (dT). The MLD differences for this region are on the order of 5% (winter) to 15% (summer). . . . .	63
4.11	Mean differences between YELLOW and GREEN for: a) shortwave net radiation (SW net), b) latent heat flux, c) sensible heat flux and d) longwave upwelling radiation (LW up), from June to September (2007-2016) (Eq. 2.16 - 2.20). . . . .	64
4.12	Monthly mean differences between YELLOW and GREEN for the components of the surface heat flux (2007-2016). <b>Left panel:</b> Average over the Arctic ( $>66^{\circ}N$ ). <b>Middle panel:</b> Average over the Laptev Sea. <b>Right panel:</b> Average over the Norwegia Sea. Net upward flux is the sum of the latent, sensible and longwave upwelling (LW up) fluxes (negative sign denotes heat loss for the ocean). Following Pabi, Dijken, and Arrigo (2008), as Laptev Sea is considered the region between $105^{\circ}$ and $150^{\circ}E$ . . . . .	65
4.13	Monthly mean differences between YELLOW and GREEN in the components of the heat budget for the upper 100 m of the water column: a) in local forcing, b) in vertical diffusion, c) in advection, and d) in non-local mixing. The values are averages over the Arctic ( $>66^{\circ}N$ ) in $W/m^3$ . . . . .	67
4.14	Same as Fig. 4.13, except for the values are averages over the Norwegian Sea in $W/m^3$ . . . . .	68
4.15	Same as Fig. 4.13, except for the values are averages over the Laptev Sea ( $105-150^{\circ}E$ ) in $W/m^3$ . . . . .	69
5.1	Mean upper 30 m dissolved inorganic nitrogen (DIN) concentration for: a) the World Ocean Atlas (WOA) 2018 (Garcia et al., 2018), b) the simulation YELLOW (2012-2014). Areas where no WOA measurements exist, have been masked (white) in panel (a). . . . .	78
5.2	Same as Fig. 5.1, but for silicate ( $SiO_2$ ) concentration . . . . .	79
5.3	Same as Fig. 5.1, but for phosphate ( $PO_4$ ) concentration. . . . .	80

5.4	Annual mean differences of total chlorophyll-a concentration between YELLOW and GREEN for the upper 100 meters, over the 2007-2016 period for: the Arctic ( <b>left panel</b> ), the Laptev Sea ( <b>middle panel</b> ), and the Norwegian Sea (highlighted area of Figure 4.9) ( <b>right panel</b> ).	81
5.5	Annual mean differences of CDOM concentration between YELLOW and GREEN for the upper 100 meters, over the 2007-2016 period for: the Arctic ( <b>left panel</b> ), the Laptev Sea ( <b>middle panel</b> ), and the Norwegian Sea ( <b>right panel</b> ).	82
5.6	Mean differences in the Norwegian Sea (highlighted area of Figure 4.9) between YELLOW and GREEN for the upper 130 meters, in: a) photosynthetically available radiation (dPAR), b) total chlorophyll-a concentration (dChl), c) light attenuation coefficient (dKd, Eq. 1.11).	83
5.7	Mean differences in the Norwegian Sea between YELLOW and GREEN for the upper 130 meters, in: a) silicate (dSiO <sub>2</sub> ), b) nitrate (dNO <sub>3</sub> ), and c) phosphate (dPO <sub>4</sub> ). Nitrate accounts for a large part of DIN.	84
5.8	Spatial distribution of large diatoms growth limiting factors in the upper 20 m, for: a) May in the GREEN simulation, b) May in the YELLOW simulation, c) October in the GREEN simulation, and d) October in the YELLOW simulation. White colour denotes limitation due to light and temperature, green due to DIN, orange due to phosphate, and blue due to silicate.	85
5.9	Same as Fig. 5.8, but for the <i>Phaeocystis</i> growth limiting factors (September has been considered for late summer - fall).	87
5.10	Same as Fig. 5.8, but for the coccolithophores growth limiting factors (September has been considered for late summer - fall).	88
5.11	Spatial distribution of differences (YELLOW-GREEN) in diatoms (large and small) phenology, in 2012: a) bloom start day at the surface (0-20m), b) bloom start day at the sub-surface (20-40m), c) bloom end day at the surface (0-20m), d) bloom end day at the sub-surface (20-40m).	89
5.12	Same as in Fig. 5.11, but for the haptophytes (coccolithophores and <i>Phaeocystis</i> ) phenology.	90

A.1	Monthly mean differences between YELLOW and GREEN in the components of the heat budget, averaged over the upper 100 m of the water column: a) in local forcing, b) in vertical diffusion, c) in advection, and d) in non-local mixing. The values are averages over the Arctic ( $>66^{\circ}N$ ) in $W/m^3$ . The error bars represent the monthly standard error. . . . .	115
A.2	Monthly mean differences between YELLOW and GREEN in the components of the heat budget, averaged over the upper 100 m of the water column: a) in local forcing, b) in vertical diffusion, c) in advection, and d) in non-local mixing. The values are averages over the Norwegian Sea. The error bars represent the monthly standard error. . . . .	116
A.3	Monthly mean differences between YELLOW and GREEN in the components of the heat budget, averaged over the upper 100 m of the water column: a) in local forcing, b) in vertical diffusion, c) in advection, and d) in non-local mixing. The values are averages over the Laptev Sea ( $105-150^{\circ}E$ ) in $W/m^3$ . The error bars represent the monthly standard error. . . . .	117
A.4	Spatial distribution of diatoms (large and small) phenology in the simulation YELLOW, in 2012: a) bloom start day (BSD) at the surface (0-20m), b) and at the sub-surface (20-40m), c) bloom end day (BED) at the surface (0-20m), d) and at the sub-surface (20-40m). . . . .	118
A.5	The same as Fig. A.4, but for haptophytes. . . . .	119



# List of Tables

2.1	CDOM absorption ( $a_{\text{CDOM}}$ in $\text{m}^{-1}$ ), Chla ( $\text{mg}/\text{m}^3$ ), TSM ( $\text{g}/\text{m}^3$ ) at two meters depth (except for $a_{\text{CDOM}}$ at station 40, S40, sampled at 5 m) and wind speed ( $U$ in $\text{m}/\text{s}$ ). . . . .	24
2.2	Biogeochemical model internal parameters and traits, where <i>Phaeo</i> refers to <i>Phaeocystis</i> , <i>Prochlor</i> to <i>Prochlorococcus</i> , N-fixers to nitrogen fixing phytoplankton and <i>cocco</i> to coccolithophores. (Table adapted from Losa et al., 2019) . . . . .	34
2.3	Biogeochemical model parameters of the nutrient-specific limitation for large and small diatoms, <i>Phaeocystis</i> ( <i>Phaeo</i> ), <i>Prochlorococcus</i> ( <i>Prochlor</i> ), nitrogen fixing phytoplankton (N-fixers), and for coccolithophores ( <i>cocco</i> ). . . . .	36
3.1	Statistical results of the validation of the SCIATRAN simulated $L_{\text{TOA}}$ against the MERIS $L_{\text{TOA}}$ per band. . . . .	39
3.2	Absorbed energy absolute difference ( $\Delta E_{\text{nabs}}$ , $\text{KJ}/\text{m}^2$ ) and relative difference ( $\% \Delta E_{\text{nabs}}$ ), as well as radiative heating ( $\Delta \text{RH}$ , $^{\circ}\text{C}$ ), ice melting rate ( $\Delta(\text{dH}/\text{dt})$ , $\text{mm}/\text{h}$ ), sensible ( $\Delta Q_{\text{sen}}$ , $\text{W}/\text{m}^2$ ), latent ( $\Delta Q_{\text{lat}}$ , $\text{W}/\text{m}^2$ ) heat flux, and net longwave radiation ( $\Delta Q_{\text{lw}}$ , $\text{W}/\text{m}^2$ ) differences for the selected scenarios. . . . .	45
4.1	Differences (YELLOW-GREEN) in the surface heat flux components averaged over the Arctic ( $>66^{\circ}\text{N}$ ), the Laptev Sea, and the Norwegian Sea. Values are calculated for two seasons, the local summer and winter. Notation is the same as in figures 4.11 and 4.12. Please note that I have considered different months for the summer and winter seasons in every region. The unit is $\text{W m}^{-2}$ . . . . .	66

4.2	Differences (YELLOW-GREEN) in the heat budget components averaged over the Arctic, the Laptev Sea, and the Norwegian Sea. Values are calculated for two seasons, the local summer and winter (as defined in Table 4.1). Every component is integrated over the first 10 m and from 10 to 100 m. $F_{\text{local}}$ refers to the local forcing term, and the unit is $\text{W m}^{-2}$ everywhere. . . . .	70
4.3	Parameterizations used in studies examining the bio-optical effect of phytoplankton or CDOM. $Z$ denotes the light attenuation depth ( $Z = 1/K_d$ ), IR the infrared radiation, and VIS the visible radiation. Additionally, R stands for red band, G for green, and B for blue band. . . .	72
5.1	Relative differences (YELLOW-GREEN) in the limiting area of every factor (light and other factors, DIN, $\text{PO}_4$ , $\text{SiO}_2$ ) over the Arctic, for large and small diatoms, <i>Phaeocystis</i> , and coccolithophores. Values in every case are calculated for a specific month, one representing spring (May) and one accounting for late summer or early fall (September or October). . . . .	86
B.1	MITgcm diagnostics required for the calculation of the heat budget terms.	121
B.2	Model parameters in the MITgcm configuration "data" file. . . . .	122

# List of Abbreviations

$a_{\text{CDOM}}(443)$	CDOM absorption at 443 nm
$a_{\text{ph}}(443)$	phytoplankton absorption at 443 nm
Chla	chlorophyll-a
CDOM	Coloured Dissolved Organic Matter
DOM	Dissolved Organic Matter
DIN	Dissolved Inorganic Nitrogen
Kd	light diffuse attenuation coefficient
MLD	Mixed Layer Depth
OCRS	Ocean Colour Remote Sensing
PAR	Photosynthetically Available Radiation
PFT	Phytoplankton Functional Type
RTE	Radiative Transfer Equation
RTM	Radiative Transfer Modelling
SM	Suspended Matter
SST	Sea Surface Temperature
SIC	Sea Ice Concentration
$SI_{\text{ext}}$	Sea Ice extent
$SI_{\text{th}}$	Sea Ice thickness
TSM	Total Suspended Matter



# Declaration of Authorship

I, Vasileios PEFANIS, declare that this thesis titled, “Loading of coloured dissolved organic matter in the Arctic Mediterranean Sea and its effects on the ocean heat budget” and the work presented in it are my own. I confirm that:

- This work was done wholly or mainly while in candidature for a research degree at this University.
- Where any part of this thesis has previously been submitted for a degree or any other qualification at this University or any other institution, this has been clearly stated.
- Where I have consulted the published work of others, this is always clearly attributed.
- Where I have quoted from the work of others, the source is always given. With the exception of such quotations, this thesis is entirely my own work.
- I have acknowledged all main sources of help.
- Where the thesis is based on work done by myself jointly with others, I have made clear exactly what was done by others and what I have contributed myself.

Signed: *Vasileios Pefanis*

---

Date: *08.03.2021*

---